4-1.1. Pyrolysis of *Mesua ferrea* and *Pongamia glabra* seed covers

India is mainly an agricultural based economy where modern agriculture system is heavily mechanized and therefore, dependent upon internal combustion engines for running farm machinery, irrigation pump sets, and other equipments. These IC engines are mostly fueled by diesel and therefore, exploration of renewable fuels must be necessary to curb the problems of fuel scarcity coupled with its increasing price and local air pollution. The fuels from bio-origin can provide a feasible solution to these problems. In this regard, bioethanol and biodiesel becomes the prominent biofuels from Indian perspective. Biodiesel is a renewable and environmental friendly alternative for diesel fuel which can be produced from a variety of vegetable oils extracted from both edible and non-edible oilseeds [1]. In recent years, biodiesel has received a considerable attention due to its biodegradability, renewability, non-toxicity and less emission of gaseous and particulate pollutants. In order to avoid the conflict of using crop for food vs. fuel choice, Government of India (GOI) regulation emphasizes on using only non-edible oilseed crops for biodiesel. In this regard, attempt has been made to experimentally evaluate the possibilities of using biodiesel from a number of non-edible oil seeds such as *Pongamia glabra* [2], *Hevea brasiliensis* [3], *Mesua ferrea* [4], *Madhuca indica* [5], *Terminalia belerica* [6], *Sapindus mukorossi* [7] etc. Among these non-edible oil bearing seeds, *P. glabra and M. ferrea* are considered as the exclusive resources that can meet the growing demand of biodiesel in India due to their high productivity and less maturity cycle. These species are abundantly available in North-Eastern region of India [4]. Moreover, *P. glabra and M. ferrea* seeds contain 30–40 wt.% and 58–75 wt.% of oil content respectively [8]. These trees are naturally distributed along the natural forests riverbanks, roadsides, canal banks and open farm lands. They are also preferable for controlling soil erosion [9]. During the production of bio-diesel, a huge amount of bio-waste like de-oiled cake, seed covers etc., are generated as a by-product which are often discarded. Utilization of these by-products is crucially important for improving the overall economy of biodiesel production and waste utilization [10]. Thus, it will be of national interest to screen the by-products for their feasibility in terms of sustainable energy production. In the current investigation,

M. ferrea seed cover (MFSC) and *P. glabra* seed cover (PGSC) were being studied as a suitable feedstock for potential utilization through thermo-chemical conversion. The effect of pyrolysis temperature and heating rate on product yield was also studied. Maximum yield of liquid product was further fractionated by using liquid column chromatography technique in order to obtain different chemical class compounds. The liquid products were analyzed for different physical and chemical properties by using different chromatographic and spectroscopic technique such as FT-IR, ^{1}H NMR and GC/MS. The co-product of pyrolysis i.e. biochar obtained at different temperatures were also analyzed for different physical and chemical properties.

4-1.2. Physico-chemical characterization of MFSC and PGSC

Physico-chemical characterization of biomass is an imperious property which determines the chemical composition and properties of biomass that affects the conversion process in a variety of ways. These inherent properties of biomass are used to assemble the information regarding any difficulties that may arise during subsequent processing. The knowledge of biomass composition will be helpful to determine the thermal behavior during conversion processes, and also yield can be predicted, mathematical models can be created to make the biomass conversion more efficient and effective [10, 11]. Table 4.1 shows the physicochemical properties of both MFSC and PGSC biomass.

Table 4.1: Physicochemical properties of MFSC and PGSC biomass

Properties		MFSC	PGSC
Proximate analysis (dry basis, wt. %)	Moisture	3.80	3.50
	Volatile Matter	76.83	74.58
	Ash	1.17	2.72
	Fixed carbon	18.20	19.20
Ultimate analysis (dry basis, wt. %)	Carbon	47.5	44.0
	Hydrogen	5.43	5.46
	Nitrogen	1.15	1.61
	Oxygen	45.9	48.8
	H/C	1.37	1.49
	O/C	0.72	0.83
	Calorific value (MJ/kg)	18.34	16.32
Compositional analysis (dry basis, wt. %)	Lignin	27.8	34.4
	Holocellulose (Cellulose + Hemicellulose)	72.2	65.6
	Extractives	15.8	14.7

It can be observed from the Table 4.1 that moisture content of the MFSC sample was 3.80 wt.% which was slightly higher than the moisture content of PGSC sample (3.50 wt.%). It has been reported that biomass sample which contains dry moisture content below 10 wt.% indicates the suitability of feedstock for energy production by thermochemical conversion [5]. Moisture content of the feedstock has a significant effect on the conversion efficiency of the pyrolysis process, its energy content and the product distribution. High moisture content reduces the heating rate resulting in more time to reach the pyrolysis temperature [7]. Both the MFSC and PGSC biomass has high volatile matter and lower ash content. As reported in the literature, biomass fuels having high volatile matter and low ash content are considered to be an ideal for conversion of biomass into its suitable products through pyrolysis process. These two properties strongly influence the combustion behavior and thermal decomposition of a particular biomass [8].

Ultimate analysis of both MFSC and PGSC biomass are shown in Table 4.1. Ultimate analysis showed that both the feedstocks contain higher amounts of carbon and oxygen percentage compared to the hydrogen percentage. The lower amount of nitrogen percentage implies the lower emission of NO_x to the atmosphere creating a minimum environmental impact. Higher proportion of oxygen percentage reduces the

energy value of biomass as compared with fossil fuels since lower energy is contained in carbon–oxygen and carbon–hydrogen bonds than that of carbon–carbon bonds [9]. PGSC biomass has lower calorific value than MFSC biomass which could be attributed to the higher O/C ratio of PGSC than that of MFSC. Further, the compositional analysis of biomass is essential since it helps to determine feedstock compositions as well as product yields from conversion processes. The basic structure of lignocellulosic biomass consists of cellulose, hemicelluloses and lignin. After delignification the residue consisting of cellulose and hemicellulose together, is called holocellulose. MFSC had higher contents of holocellulose (72.2 wt.%) than PGSC (65.6 wt.%). The lignin contents were also found to be 34.4 wt.% and 27.8 wt.% respectively for both PGSC and MFSC biomass (shown in Table 4.1). Lignin present in lignocellulosic biomass holds a great potential in different industries as a source for chemicals, fuels and other bio-products. Besides its contribution to energy production, lignin is biodegradable, antimicrobial, an antioxidant, and CO_2 neutral. Such diverse properties of lignin have emphasized the need to convert and use lignin as liquid fuel additives and commercially important chemicals [12].

4-1.3. Thermal degradation behavior of PGSC biomass

Thermogravimetric analysis (TGA) is the most common technique used for better understanding of pyrolysis of biomass into energy and products. It is a rapid and precise technique to determine the mass loss of a sample over time and evaluate the thermal decomposition of solids and its kinetics [10]. During pyrolysis, the larger molecules of biomass are broken down to low molecular weight gases, liquids and solid char. The combustible gases are transformed into liquid products which can be used as a fuel due to their high calorific value [11]. The chemical transformation of solid raw materials to various products is highly dependent on the kinetic rates of the pyrolysis reactions. Therefore, it is obvious that accurate kinetic models are required in order to achieve a responsive design for the pyrolysis process. Mathematical methods fall into two categories are viz. model-fitting and model-free (isoconversional) methods. Application of model-fitting methods has recently declined in favor of isoconversional methods [13]. The advantage of the model-free analysis is founded on its simplicity and on the avoidance of errors connected with the

choice of a kinetic model. Isoconversional methods enable determination of kinetic parameters without knowledge of reaction mechanism [13–14]. In present study, attempt has been made to investigate the isothermal and non-isothermal data and to establish the minimum number of independent experiments required for determining the kinetic model of the reaction.

4-1.3.1. Thermogravimetric analysis

Figs. 4.1 and 4.2 shows the TG and DTG curves obtained during pyrolysis of PGSC under an inert atmosphere at three different heating rates of 10, 20, and 30 ºC/min. The thermal degradation curve can be divided into three stages: moisture drying (S_I), main devolatilization (active pyrolysis zone) (S_{II}) and continuous slight volatilization (passive pyrolysis zone) (S_{III}). Initial weight loss of the PGSC sample was caused by a loss of moisture content starting at about 50 ºC and continuing up to 130 ºC. The sample started to decompose and release volatiles at about 180 ºC. The step is specified as a small peak on the left most side of the DTG curve. The thermogravimetric (TG) curves of the sample clearly showed changes in slope of the curves which might be due to the presence of three main components (hemicelluloses, cellulose and lignin) of the lignocellulosic material [15].

After the loss of water and light volatiles compounds, the main devolatilization step occurred with a sharp drop in the TG curve which began at around 200 ºC and finished at 360 ºC. This region was referred to as active pyrolysis zone due to the occurrence of high mass loss rate [16]. DTG curve showed two distinct peaks in active pyrolysis region which was in agreement with previous findings [17]. The first peak was attributed to the decomposition of hemicellulose and second to that of cellulose. The hemicellulose decomposition generally appears as a less pronounced “shoulder” whereas the decomposition of cellulose occurs as a well-defined peak [17–18]. At the end of this stage, a slower decrease of mass loss rate was observed. This loss corresponds to the slower degradation of lignin in both regions of active and passive pyrolysis without any characteristic peak [13].

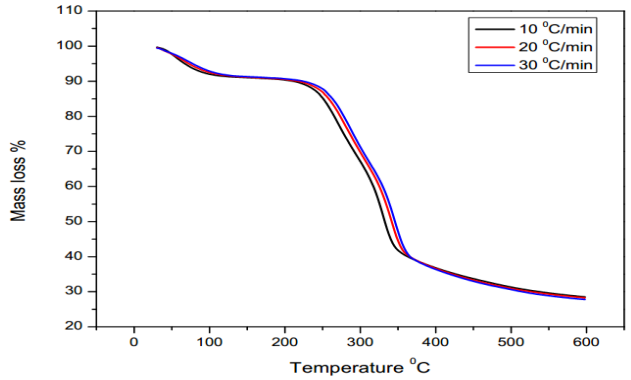

Fig. 4.1: TG curves of PGSC recorded at three different heating rates

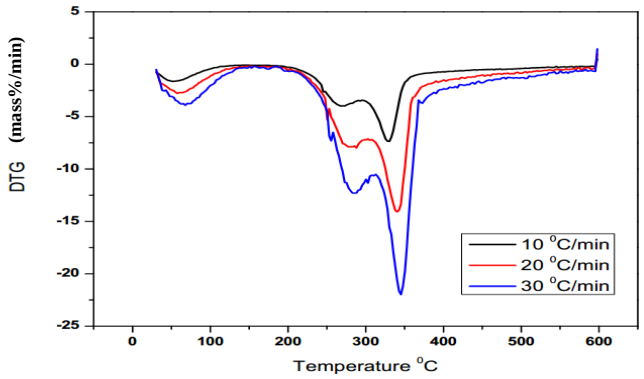

Fig. 4.2: DTG curves of PGSC recorded at three different heating rates

The characteristic temperatures of the active pyrolysis zone for PGSC sample namely starting temperature (T_{onset}), ending temperature (T_{offset}) and the temperature of maximum mass loss rate (T_{max}) that occurred during thermal analysis at three different heating rates are given in Table 4.2 below.

Table 4.2: Characteristic temperatures for PGSC in active pyrolysis zone (S_{II})

Heating rate (°C/min)	**S_{II}**		
	T_{onset}	**T_{max}**	**T_{offset}**
10	183	329	363
20	193	340	379
30	207	345	385

It can be observed from the Table 4.2 that, there is an occurrence of shift in the TG and DTG curves to higher temperatures with increasing heating rates. An increase in the heating rate tends to delay the thermal degradation process towards higher temperatures, most probably due to the presence of increased thermal lag [16]. Thermal lag is the time required to add or remove heat from the biomass before it reaches the desired temperature. At a given temperature, a higher heating rate implies that the material reaches that temperature in a shorter time. It can be clearly observed in Fig. 4.2 that maximum mass loss rates are also shifted to higher temperatures as the heating rate is increased. This can be explained by the effect of inertia of devolatilization process, with the decrease in characteristic time of the process [19].

The results obtained from thermogravimetric analysis were elaborated according to model-free methods to calculate the kinetic parameters. The activation energy (E_a) and frequency factors were calculated by using Friedman (isothermal), KAS and FWO (non-isothermal) methods.

4-1.3.2. Friedman method

Friedman is a differential iso-conversional method described by using the eq. (3.7) in chapter 3. This method is based on selected conversion values (α) from 0.1 to 0.9 irrespective of heating rates. The Friedman plot of $\ln(d\alpha/dt)$ vs. $1/T$ for different values of conversion are shown in Fig. 4.3. A set of straight lines were obtained at different conversions, with the slope of each line being equal to $(-E_a/R)$. From the slope, activation energies at varying degree of conversion were calculated and are reported in Table 4.3.

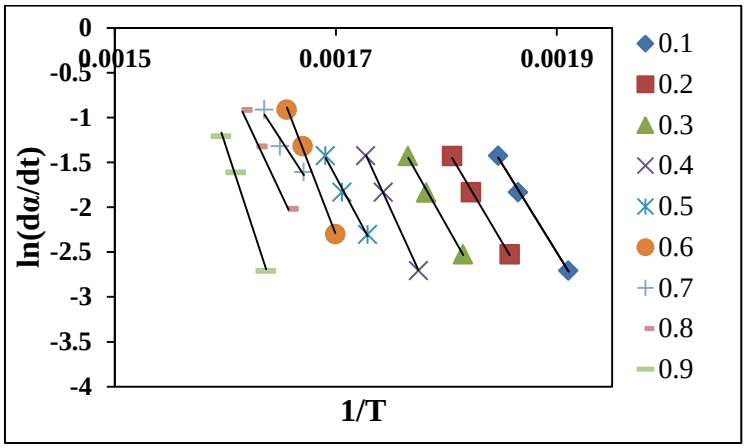

Fig. 4.3: Plots obtained by Friedman method for determination of activation energy of PGSC at S_{II}

Table 4.3: Kinetic parameters obtained from Friedman plot for PGSC

Conversion, α	Activation energy, E_a (kJ/mol)	Intercepts	Frequency factor	R^2
0.1	165.68	35.35	2.25E+15	0.9985
0.2	173.71	36.20	5.26E+15	0.9979
0.3	181.76	37.01	1.18E+16	0.9980
0.4	224.09	45.07	3.74E+19	0.9997
0.5	189.06	37.09	1.28E+16	0.9940
0.6	265.62	52.03	3.94E+22	0.9983
0.7	157.38	30.03	1.10E+13	0.9527
0.8	217.56	41.44	9.93E+17	0.9980
0.9	311.90	58.60	2.81E+25	0.9956

It can be observed from the Table 4.3 that E_a varied from 165 to 311 kJ/mol when α ranges from 0.1 to 0.9. The variation of E_a with α may be attributed to the combination effect of thermal decomposition of biopolymer components (cellulose, hemicellulose and lignin) contained in PGSC sample. Thermal decomposition of each of the components corresponds to a distribution of activation energies depending upon the size and structure of biopolymers [20]. The decomposition of weaker bonds occurs at relatively lower temperature while the crack of stronger bonds needs more energy at higher temperature [21]. Similar results were reported for pyrolysis of eucalyptus wood [22] and sweet sorghum bagasse [23]. Likewise, Wu et al. [24] reported the pyrolysis of eight different lignocellulosic biomass samples viz. corn

stover, cotton stalk, palm oil husk, pine wood, red oak, sugar cane bagasse, switch grass and wheat straw [24].

4-1.3.3. Flynn-Wall-Ozawa (FWO) method

The FWO is an integral iso-conversional method expressed by using the eq. (3.8) in chapter 3. Kinetic parameters were calculated from the FWO plots of ln(β) vs. 1/T for different values of conversion as shown in Fig. 4.4. A set of straight lines were obtained at different degree of conversions with the slope of each line being equal to ($-0.4567E_a/R$), from where energies of activation, E_a, were calculated. Values of the activation energies and the corresponding frequency factors obtained from the FWO method are given in Table 4.4.

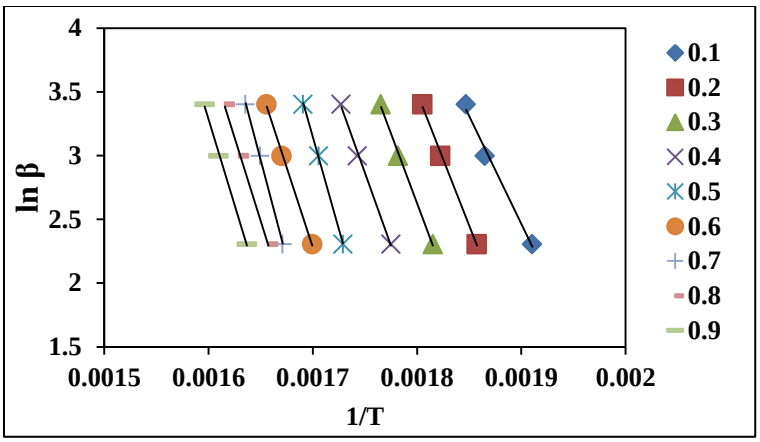

Fig. 4.4: Plots obtained by FWO method for determination of activation energy of PGSC at S_{II}

Table 4.4: Kinetic parameters obtained from FWO plot for PGSC

Conversion, α	Activation energy, E_a (kJ/mol)	Intercepts	Frequency factor	R^2
0.1	147.32	34.46	9.24E+14	0.9907
0.2	182.74	41.10	7.07E+17	0.9980
0.3	191.21	41.97	1.68E+18	0.9980
0.4	199.87	42.85	4.06E+18	0.9980
0.5	252.86	52.29	5.11E+22	0.9991
0.6	217.77	44.61	2.36E+19	0.9980
0.7	270.46	53.98	2.77E+23	0.9991
0.8	228.88	45.66	6.75E+19	0.9980
0.9	234.53	46.18	1.13E+20	0.9980

Table 4.4 shows that activation energy, E_a varied from 147 to 234 kJ/mol when α ranges from 0.1 to 0.9. A change in E_a with an increase in the conversion degree is indicative of a complex reaction mechanism. The activation energy calculated according to the FWO method is called the apparent activation energy, because it is the sum of the activation energies of the chemical reactions and physical processes (like melting, vaporization and sublimation) that occur simultaneously during thermal degradation. It could also be observed that the correlation coefficients (R^2) were between 0.9907 and 0.9991, and that the lines were positioned close and parallel to each other, indicating small variations in the activation energy according to the conversion [25].

4-1.3.4. Kissinger-Akahira-Sunose (KAS) method

The KAS is an integral model-free method, defined by the eq. (3.11) in chapter 3 and showed the dependency of frequency factor and activation energy on the degree of conversion, α. By plotting the ln (β/T^2) vs. 1/T for different values of conversion gives the KAS plot depicted in Fig. 4.5. The apparent activation energies and frequency factor were obtained from the slope and intercept of regression lines respectively and the corresponding values are given in Table 4.5. Correlation coefficients (R^2) values are also listed in Table 4.5.

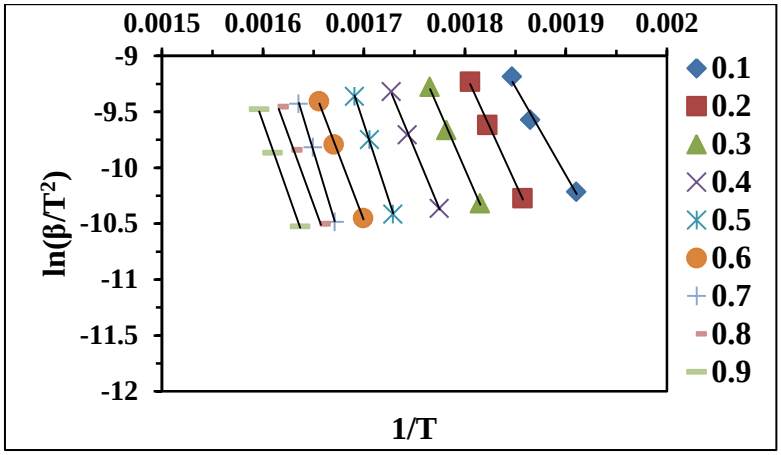

Fig. 4.5: Plots obtained by KAS method for determination of activation energy of PGSC at S_{II}

Table 4.5: Kinetic parameters obtained from KAS plot for PGSC

Conversion, α	Activation energy, E_a (kJ/mol)	Intercepts	Frequency factor	R^2
0.1	131.19	19.91	4.4E+8	0.9895
0.2	164.63	26.49	3.1E+11	0.9978
0.3	172.48	27.32	7.3E+11	0.9978
0.4	180.50	28.16	1.69E+12	0.9978
0.5	230.64	37.55	2.03E+16	0.9990
0.6	197.10	29.83	9.01E+12	0.9978
0.7	247.04	39.17	1.02E+17	0.9990
0.8	207.41	30.83	2.45E+13	0.9979
0.9	212.66	31.33	4.04E+13	0.9979

It can be observed from Table 4.5, apparent activation energies calculated by using KAS method was not similar for all degree of conversion which indicated the existence of a complex multi-step mechanism that occurred in the solid state. The apparent value of activation energy was about 131–212 kJ/mol as α value increased from 0.1 to 0.9. It can be seen from the Table 4.5 that values of activation energies are independent of α values.

The mean activation energies calculated from Friedman, FWO and KAS methods were found to be 209.60, 213.96 and 193.73 kJ/mol correspondingly. Also, excellent linear correlation coefficients were obtained with a R^2 value close to unity for Friedman, FWO and KAS methods respectively.

4-1.4. Thermal degradation behavior of MFSC biomass

The TG and DTG curves for heating rates of 10, 20 and 30 ºC/min for MFSC biomass are shown in Figs. 4.6 and 4.7. As discussed in the previous section the entire pyrolysis process is divided into three zones corresponding to moisture evaporation, main devolatilization (S_{II}) and continuous slight devolatilization (S_{III}). The second region corresponds to active pyrolysis zone where peaks of cellulose and hemicelluloses are merged to give a broader peak. The third region is known as passive pyrolysis zone where lignin decomposition is prominent. Detailed studies using TG-DTG curves have been carried out to estimate the kinetic parameters and are presented in the succeeding sections.

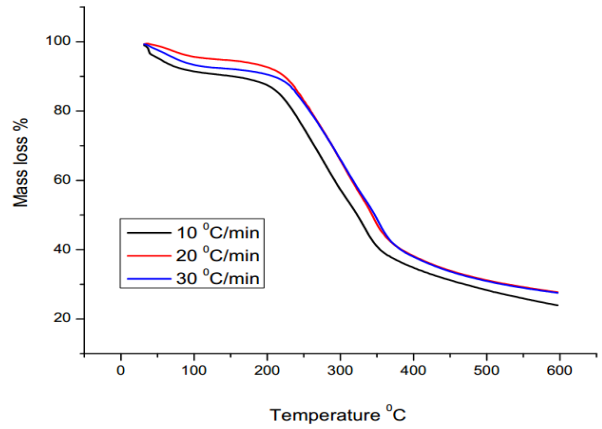

Fig. 4.6: TG curves of MFSC biomass recorded at three different heating rates.

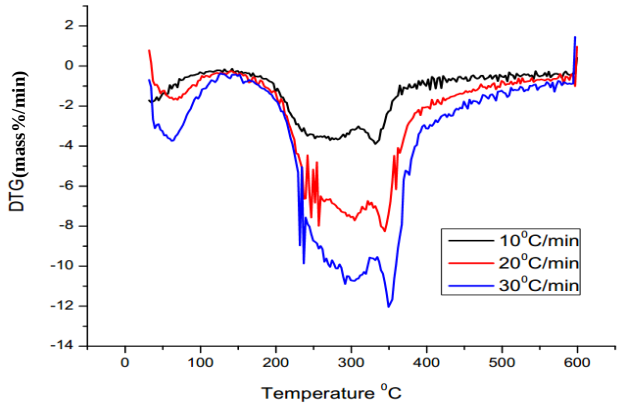

Fig. 4.7: DTG curves of MFSC biomass recorded at three different heating rates

The TG curves of MFSC obtained at different heating rates show a different char yield. This might be due to the heterogeneities of the material tested. The strong effect of the heating rate on the formation of char from biomass may be attributed to the high cellulose content of the biomass. It is known that heating rate has a significant effect on the pyrolysis of cellulose. The dehydration of cellulose to the more stable anhydrocellulose, which gives higher char yield, is the dominant reaction at low temperatures with a low heating rate. As a result, less water remains for the gasification/reforming reaction when it reaches higher temperatures (at high temperatures, the gasification/reforming reaction may occur if there is some water or oxygen-containing species existing on the surface). Thus, more carbon atoms are left for char formation. During the high heating rate pyrolysis process, more energy is

provided to the biomass, and more organic compounds are active and volatilized. If the heating rate is high, the residence time of the biomass at low temperatures is short. Therefore, higher heating rate provides a shorter time for the dehydration reactions. Thus, more water may be left in the biomass, leading to the gasification reaction, so the char yield becomes lower at high heating rates [26].

The values of characteristic temperatures for all the heating rates related to active pyrolysis zone (S_{II}) are given in Table 4.6. It can be observed from the Table 4.6 that all characteristic temperatures were laterally shifted to higher temperature with increasing heating rate similar to the thermal degradation of PGSC biomass described in the previous section (Section 4.3). The maximum mass loss rates were also shifted to higher temperatures with increasing heating rate. The lateral shift is also illustrated in Fig. 4.7. The lateral shift has been reported for different types of biomass and has been assigned as being due to the combined effects of the heat transfer at different heating rates and the kinetics of the decomposition resulting in delayed decomposition [19].

Table 4.6: Characteristic temperatures for MFSC biomass in active pyrolysis zone (S_{II})

Heating rate (°C/min)	**S_{II}**		
	T_{onset}	**T_{max}**	**T_{offset}**
10	150	331	365
20	168	344	396
30	171	350	406

The results obtained from thermogravimetric analysis were elaborated according to model-free methods to calculate the kinetic parameters. The activation energies (E_a) and frequency factors were obtained by using Friedman, KAS and FWO methods.

4-1.4.1. Friedman method

The Friedman isoconversional plots obtained from the simultaneous analysis performed by means of Eq. (3.7) from chapter 3 are shown in Fig. 4.8. The activation energies (E_a) calculated from the slope of the plots for different values of conversion

(α) are given in Table 4.7 together with their corresponding correlation coefficients (R^2).

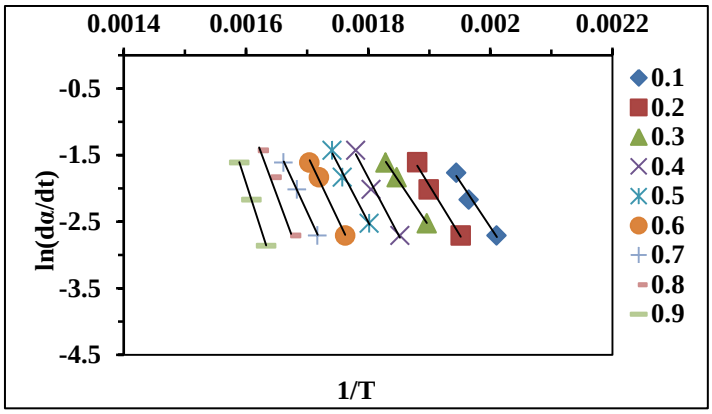

Fig. 4.8: Plots obtained by Friedman method for determination of activation energy of MFSC at S_{II}

Table 4.7: Kinetic parameters obtained from Friedman plot for MFSC

Conversion, α	Activation energy, E_a (kJ/mol)	Intercepts	Frequency factor	R^2
0.1	115.24	25.13	7.80E+10	0.9825
0.2	124.43	26.48	3.16E+11	0.9882
0.3	113.89	23.45	1.48E+10	0.9991
0.4	144.17	29.38	5.46E+12	0.9850
0.5	145.55	29.00	3.93E+12	0.9883
0.6	159.47	31.11	3.17E+13	0.9947
0.7	165.32	31.44	4.37E+13	0.9988
0.8	204.06	38.40	4.84E+16	0.9914
0.9	237.11	43.71	8.87E+18	0.9997

It can be observed from the Table 4.7 that activation energy varied from 115–237 kJ/mol as the conversion increased from 0.1–0.9. These results demonstrate that a constant activation energy E_a= 156.46 kJ/mol could describe the entire process and was independent of α values. Values of correlation coefficients also increased from 0.9825 to 0.9997 with an increase in α values from 0.1–0.9.

4-1.4.2. Flynn-Wall-Ozawa (FWO) method

FWO isoconversional plots obtained from the simultaneous analysis performed by means of Eq. (3.8) from chapter 3 are shown in Fig. 4.9. The activation

energies calculated from the slope of the FWO plots for different values of conversion (α) are shown in Table 4.8 along with their corresponding correlation coefficients, R^2.

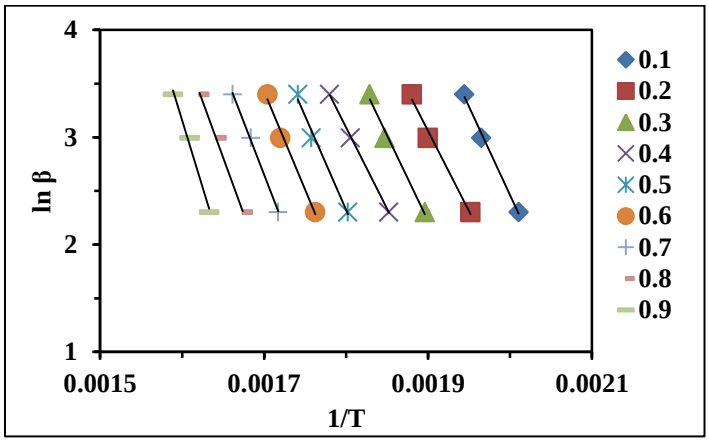

Fig. 4.9: Plots obtained by FWO method for determination of activation energy of MFSC at S_{II}

Table 4.8: Kinetic parameters obtained from FWO plot for MFSC

Conversion, α	Activation energy, E_a (kJ/mol)	Intercepts	Frequency factor	R^2
0.1	143.11	35.18	1.89E+15	0.9959
0.2	130.90	31.49	4.74E+13	0.9882
0.3	138.54	32.32	1.08E+14	0.9882
0.4	132.38	30.33	1.48E+13	0.9995
0.5	153.12	33.83	4.92E+14	0.9883
0.6	159.98	34.52	9.81E+14	0.9883
0.7	173.92	36.45	6.76E+15	0.9988
0.8	182.85	37.30	1.58E+16	0.9988
0.9	219.65	43.34	6.64E+18	0.9892

It can be seen from the Table 4.8 that the activation energy is independent of conversion degree. The data obtained from the FWO plot gives the value of constant activation energy, E_a = 159.38 kJ/mol.

4-1.4.3. Kissinger-Akahira-Sunose (KAS) method

The KAS isoconversional plots obtained from the simultaneous analysis performed by means of Eq. (3.11) described in chapter 3 are shown in Fig. 4.10. The activation energy calculated from the slope of the KAS plots for different value of

conversion (α) is included in Table 4.9 together with their corresponding correlation coefficients.

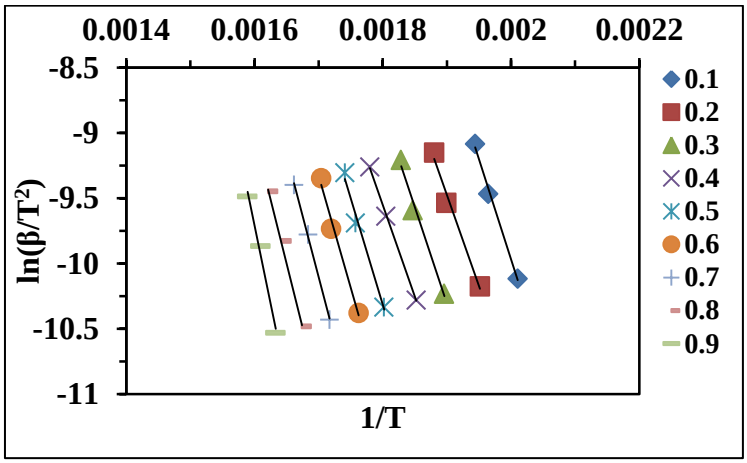

Fig. 4.10: Plots obtained by KAS method for determination of activation energy of MFSC at S_{II}

Table 4.9: Kinetic parameters obtained from KAS plot for MFSC

Conversion, α	Activation energy, E_a (kJ/mol)	Intercepts	Frequency factor	R^2
0.1	127.63	20.73	1.00E+9	0.9954
0.2	115.76	16.98	2.36E+7	0.9864
0.3	122.77	17.75	5.11E+7	0.9865
0.4	116.68	15.71	6.64E+6	0.9995
0.5	136.17	19.16	2.09E+8	0.9867
0.6	142.49	19.81	4.01E+8	0.9868
0.7	155.48	21.69	2.62E+9	0.9986
0.8	163.72	22.49	5.85E+9	0.9986
0.9	198.47	28.48	2.33E+12	0.9880

It can be observed from Table 4.9 that apparent activation energy calculated by KAS method for the pyrolysis of MFSC was not similar for all conversion. That the values of activation energy did not follow any particular trend indicated that activation energy was independent of conversion. A constant value of activation energy for the KAS method is determined as E_a = 142.13 kJ/mol.

4-1.5. Statistical optimization using Response surface model (RSM) for PGSC

For PGSC sample, RSM was performed in order to achieve a realistic model between the investigated factors such as temperature (A) and heating rate (B) with the observed response i.e. the yield of pyrolysis products (biooil, biochar and gas). A second order polynomial equation describes the overall relationship between the two independent variables (shown in chapter 3). A total of 13 experimental runs were performed whose values are given in Table 4.10.

Table 4.10: Design matrix using Central Composite Design and experiment results

		Factor 1	Factor 2	Response 1	Response 2	Response 3
Std	**Run**	**A: Temperature**	**B: Heating rate**	**Biooil**	**Biochar**	**Gas**
7	1	500	3.7868	20.2	35.15	25.4
3	2	350	40	23.2	32.92	23.68
13	3	500	25	26.3	31.3	29.4
2	4	650	10	22.9	32.7	30.8
10	5	500	25	26.3	31.3	29.4
11	6	500	25	26.3	31.3	29.4
9	7	500	25	26.3	31.3	29.4
12	8	500	25	26.3	31.3	29.4
5	9	287.868	25	15.6	40	21.2
6	10	712.132	25	24.4	28.9	33.2
8	11	500	46.2132	27.4	32.68	29.9
1	12	350	10	17.9	40.13	22.3
4	13	650	40	26.9	28.87	31.8

The experimental results obtained for yield (wt.%) of biooil, biochar and gas were fitted to second degree polynomial model, which can be represented by Eqs.1, 2 and 3 respectively in terms of coded factors.

$$\boldsymbol{Biooil} = +26.78 + 2.57 \times A + 2.45 \times B - 0.48 \times AB - 3.25 \times A^2 - 1.23 \times B^2 \quad (1)$$

$$\boldsymbol{Biochar} = +31.30 - 3.40 \times A - 1.82 \times B + 0.84 \times AB + 1.44 \times A^2 + 1.18 \times B^2 \quad (2)$$

$$\boldsymbol{Gas} = +29.40 + 4.20 \times A + 1.09 \times B - 0.095 \times AB - 1.17 \times A^2 - 0.95 \times B^2 \quad (3)$$

The interaction between the independent variables as well as significance of each model term was established by analysis of variance (ANOVA) and the results obtained are presented in Table 4.11.

Table 4.11: Results of ANOVA for PGSC

Products	**Biooil**			**Biochar**			**Gas**		
	Sum of Sqs.	F value	p-value Prob>F	Sum of Sqs.	F value	p-value Prob>F	Sum of Sqs.	F value	p-value Prob>F
Model	179.79	**65.34**	< 0.0001	142.97	**20.22**	0.0005	164.60	**106.88**	< 0.0001
A-Temperature	52.76	95.88	< 0.0001	92.33	65.29	< 0.0001	141.04	457.89	< 0.0001
B-Heating rate	47.97	87.17	< 0.0001	26.40	18.67	0.0035	9.56	31.03	0.0008
AB	0.90	1.64	0.2441	2.86	2.02	0.1983	0.036	0.12	0.7421
A^2	73.59	133.73	< 0.0001	14.49	10.24	0.0151	9.52	30.92	0.0009
B^2	10.48	19.05	0.0010	9.61	6.80	0.0350	6.21	20.17	0.0028
R^2	0.9790			0.9352			0.9871		
Adj-R^2	0.9640			0.8890			0.9778		

The ANOVA analysis showed that most of the variability lie in the observed data could be best explained by a quadratic model. Significance of each term can be determined by using both F-value and Prob > F values. The larger F-value indicates that the term is significant. From Table 4.11, it can be observed that model F-values of 65.34, 20.22 and 106.88 for biooil, biochar and gaseous products respectively implies a significant model. There is only a 0.01 % chance that a Model F-value this large could occur due to noise for both the biooil and gaseous product, and 0.05% chance for biochar. The analysis showed that the p-value (less than 0.05) as a statistic test indicated that the model terms are significant. The "p-value" >0.1 indicate the model terms are not significant and are eliminated in order to achieve an improved surface model (without those terms which are required to support hierarchy). Therefore, reduction of this term (p-value) is an important strategy to get improved fitted surface model. For all the three responses A, B, A^2, B^2 are significant model terms. Both the R^2 and adjusted R^2 values for the model are high enough indicating a close fit of the model to the actual data within the selected operating conditions. Adequate precision (Adeq-Precision) measures the signal to noise ratio and a ratio

more that 4 is desired. In the present study, the value of Adeq-Precision for biooil, biochar and gas are 22.114, 13.115 and 31.498 respectively indicating adequate signal and the model can be used to navigate the design space.

4-1.5.1. Response surface plots for PGSC

The three dimensional surface plots and contour plots of response versus two variables at a time for PGSC sample are shown in Figs. 4.11(a–f). The plots are quite helpful to bring out useful information about the temperature-heating rate-yield correlation within the experimental temperature range of 350–650 ºC and heating rate of 10–40 ºC/min.

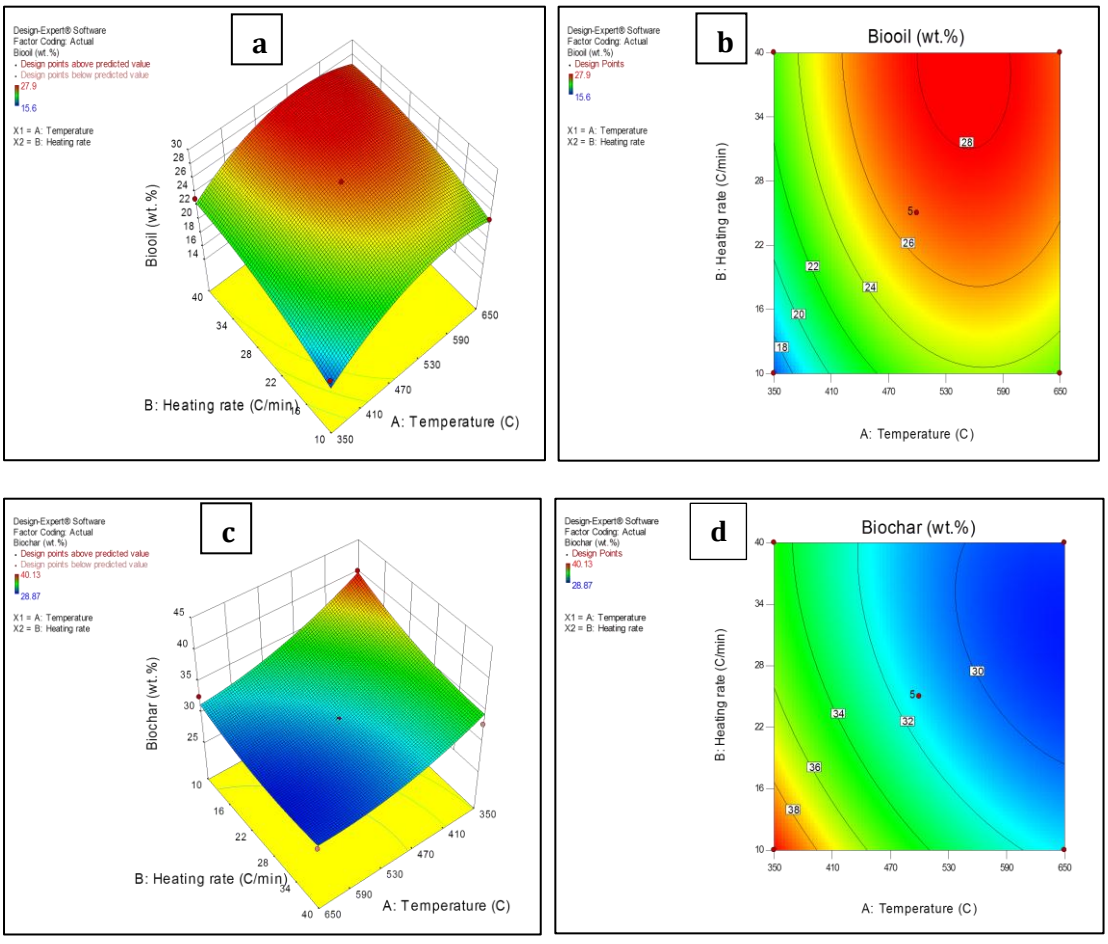

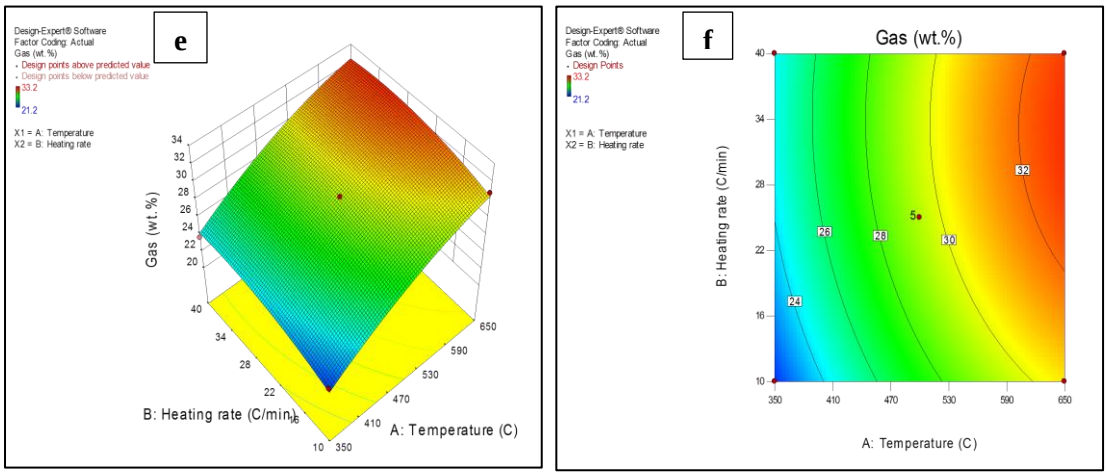

Fig. 4.11: Response surface plots and contour plots of yield percentage of biooil (a, b); biochar (c, d); and gas (e, f) obtained from pyrolysis of PGSC

The three dimensional surface plots and their respective contour plots of response versus two variables at a time are shown in Figs. 4.11(a-f). The plots are quite helpful to bring out useful information about the temperature–heating-rate–yield correlation within the experimental temperature range of 350–650 ºC and heating rate of 10–40 ºC/min. Figs. 4.11(a) and (b) showed the interaction between the temperature (A) and heating rate (B) on the yield percentage of bio-oil. The 3–D plot clearly indicated that increase of temperature from 350–550 ºC increased the yield of bio-oil but, a gradual decline in the response was observed if the temperature further rises to 650 ºC. Contour plot of biooil (Fig. 4.11(b)) indicated that maximum yield of biooil was obtained at higher temperature with higher heating rate. Therefore, it can be observed from the Figs. 4.11(a) and (b) that both temperature and heating rate has significant effect on biooil yield. The red portion on the response surface plot represents the highest yield of biooil. The effect of variables on the response was more distinct at their lower values which were represented by blue and green portions on the plots. On the other hand, the yellow portion represents the response which signifies the variation of temperature and heating rate at an intermediate range. Similarly, an inverse effect of temperature and heating rate on the yield of biochar can be anticipated from the plots shown in Figs. 4.11(c) and (d). Figs 4.11(e) and (f) correspondingly show the surface and contour plot of gaseous product yield which was completely depended on pyrolysis temperature. Heating rate has no major

influences on the gaseous product yield. Furthermore, with the help of such type of response surface plot, one can precisely design product yield model under different values of temperature and heating rate. It is also possible to obtain information over a wide range of experimental conditions by using a small number of experimental runs which is also a time consuming process. Results showed that the generated regression models adequately explained the data variation and significantly represented the actual relationship between the independent variables and the responses.

4-1.5.2. Optimization of PGSC biooil yield

In order to determine the optimum condition of biooil yield RSM simulation was carried out based on the effect of temperature and heating rate. Selected parameters (temperature and heating rate) were being evaluated at four different points. Each point was investigated to select the condition that can produce the largest volume of pyrolytic liquid i.e. biooil and showed the highest value desirability (equal to 1). However, in the present investigation the temperature was set at a target of 550 ºC with maximum value of heating rate (40 ºC/min). A solution with desirability one was given by the statistical software based on the preceding conditions (shown in Fig. 4.12).

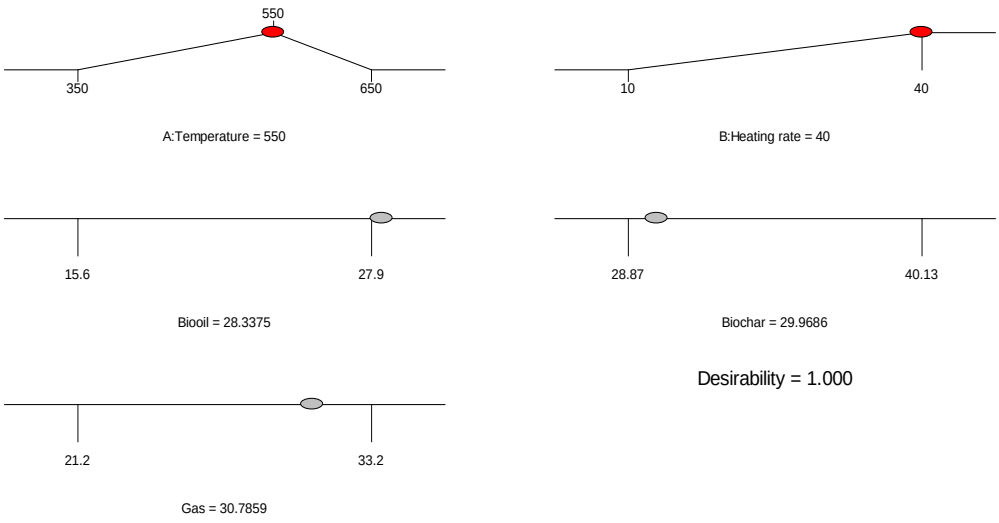

Fig. 4.12: Optimum conditions for highest yield of liquid product from pyrolysis of PGSC

It can be observed from the Fig. 4.12 that, biooil yield of 28.33 wt.% was obtained at the optimum pyrolysis condition of PGSC biomass along with the biochar and gas as co-products with yield percentage of 29.96 wt.% and 30.78 wt.% respectively.

4-1.6. Statistical optimization using Response surface model (RSM) for MFSC

RSM analysis was executed to achieve a realistic model which shows the effect of interaction between temperatures (A) and heating rate (B) on the three responses i.e. yield of biooil, biochar and gas during pyrolysis of MFSC biomass. The complete design matrix and response for yield of pyrolysis products are presented in Table 4.12.

Table 4.12: Design matrix using Central Composite Design and experiment results

		Factor 1	Factor 2	Response 1	Response 2	Response 3
Std	**Run**	**A:Temperature**	**B:Heating rate**	**Biooil**	**Biochar**	**Gas**
		ºC	**ºC/min**	**wt.%**	**wt.%**	**wt.%**
9	1	500	25	27.8	30.2	27.8
5	2	287.868	25	19.2	39.7	18.9
13	3	500	25	27.8	30.2	27.8
3	4	350	40	25.2	30.46	20.5
2	5	650	10	25.4	28.9	23.9
11	6	500	25	27.8	30.2	27.8
6	7	712.132	25	24.7	27.9	26.8
7	8	500	3.7868	23.5	32.2	22.6
10	9	500	25	27.8	30.2	27.8
4	10	650	40	27.8	25.76	24.7
8	11	500	46.2132	28.1	26.8	22.6
1	12	350	10	20.3	37.6	20.2
12	13	500	25	27.4	30.2	27.8

Data were analyzed by using ANOVA, and models were then tested for their significance and suitability. ANOVA analysis showed that experimental data are best fitted into a quadratic equation which establishes its significance. The quadratic models for conversion of all three responses in terms of coded factors are represented by following equations:

$$\boldsymbol{Biooil} = +27.72 + 1.93 \times A + 1.73 \times B - 0.63 \times AB - 2.68 \times A^2 - 0.76 \times B^2 \quad (4)$$

$$\boldsymbol{Biochar} = +30.20 - 3.27 \times A - 2.24 \times B + 1.00 \times AB + 1.03 \times A^2 - 0.42 \times B^2 \quad (5)$$

$$\boldsymbol{Gas} = +27.80 + 2.38 \times A + 0.14 \times B + 0.12 \times AB - 2.57 \times A^2 - 2.70 \times B^2 \quad (6)$$

The statistical models were checked by F-tests for every response and their respective results for ANOVA are summarized in Table 4.13.

Table 4.13: Results of ANOVA for MFSC

Products	**Biooil**			**Biochar**			**Gas**		
	Sum of Sqs.	F value	p-value Prob>F	Sum of Sqs.	F value	p-value Prob>F	Sum of Sqs.	F value	p-value Prob>F
Model	106.67	**100.38**	< 0.0001	139.03	**180.97**	< 0.0001	131.36	**101.62**	< 0.0001
A-Temperature	29.95	140.91	< 0.0001	85.33	555.35	< 0.0001	45.47	175.87	<0.0001
B-Heating rate	23.82	112.10	< 0.0001	40.13	261.14	< 0.0001	0.15	0.59	0.4693
AB	1.56	7.35	0.0301	4.00	26.03	0.0014	0.063	0.24	0.6380
A^2	50.15	235.97	< 0.0001	7.42	48.26	0.0002	46.13	178.41	<0.0001
B^2	4.02	18.91	0.0034	1.21	7.89	0.0262	50.71	196.16	<0.0001
Residuals	1.49	-	-	1.08	-	-	0.26	-	-
Lack of Fit	1.36	**14.16**	0.0135	1.08	-	-	0.60	-	-
Pure error	0.13	-	-	0.000	-	-	0.000	-	-
R-Squared	0.9862			0.9923			0.9864		
Adj R-Squared	0.9764			0.9868			0.9767		
Adeq Precision	28.821			41.767			24.669		

In Table 4.13, the model F-values for biooil, biochar and gaseous products are 100.38, 180.97 and 101.62 respectively which implies the significance of the models. There is only a 0.01 % chance that a Model F-value this large could occur due to noise. The term "p-value" less than 0.05 indicates that model terms are statistically significant whereas greater than 0.1 indicate the non-significance of the model terms. Presence of large number of insignificant model terms may lead to enhancement of the model. In case of biooil, evidence is the lack-of-fit F-value. The lack-of-fit F-value of 14.16 implies that the lack-of-fit is significant relative to the pure error. There is a 1.35% chance that a lack-of-fit F-value this large could occur due to noise. In case of biooil, all the model coefficients, namely A, B, AB, A^2, and B^2 are significant. Similarly, in case of biochar A, B, AB, A^2 and for gaseous product A, A^2,

B^2 are significant model terms. R^2, Adj-R^2 and Adeq Precision values of the suggested model for all three responses are shown in Table 4.13 and their high values support the significance of the models.

4-1.6.1. Response surface plots for MFSC

The three dimensional surface plots and contour plots of response versus two variables for MFSC sample at a time are shown in Figs. 4.13(a–f). The plots depicted the correlation between the temperature-heating rate-yield percentages for an experimental set up with temperature range of 350–650 ºC and heating rate of 10–40 ºC/min.

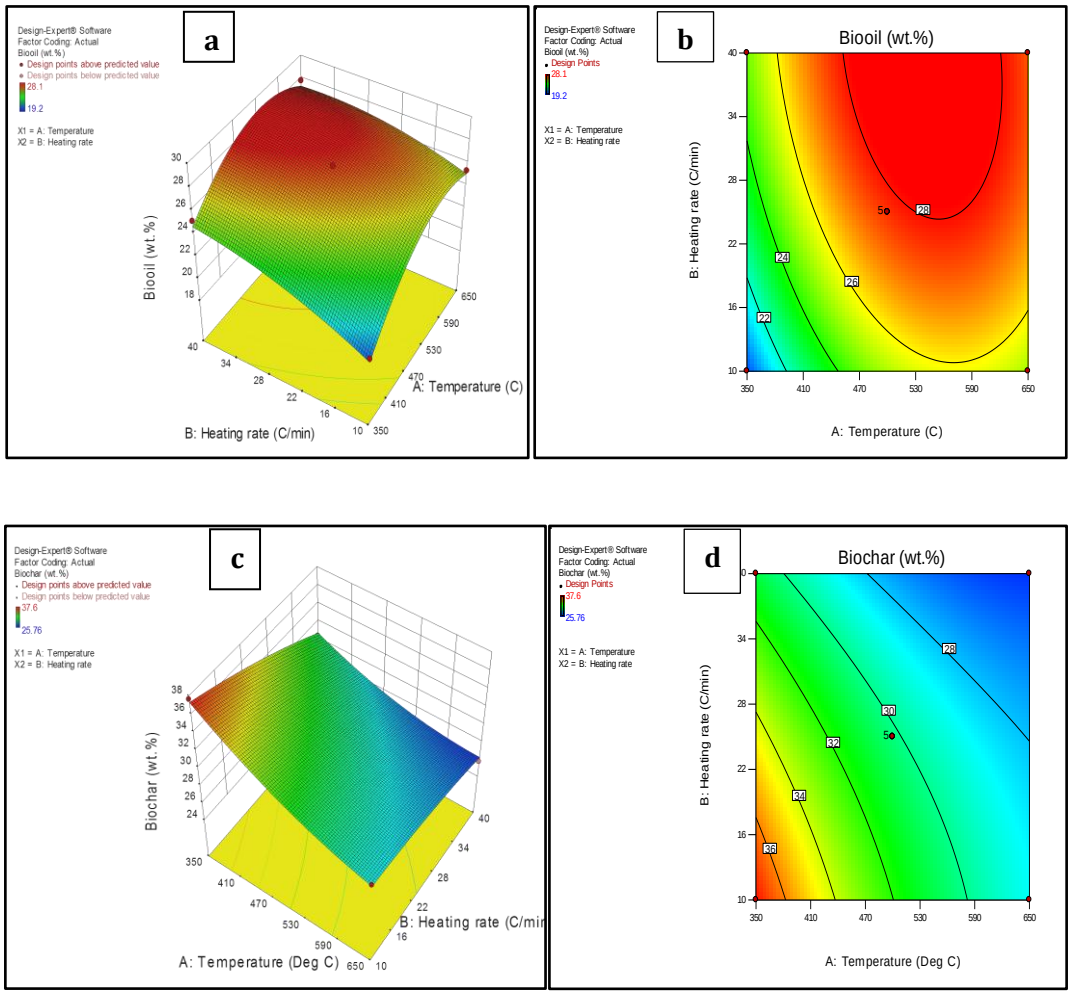

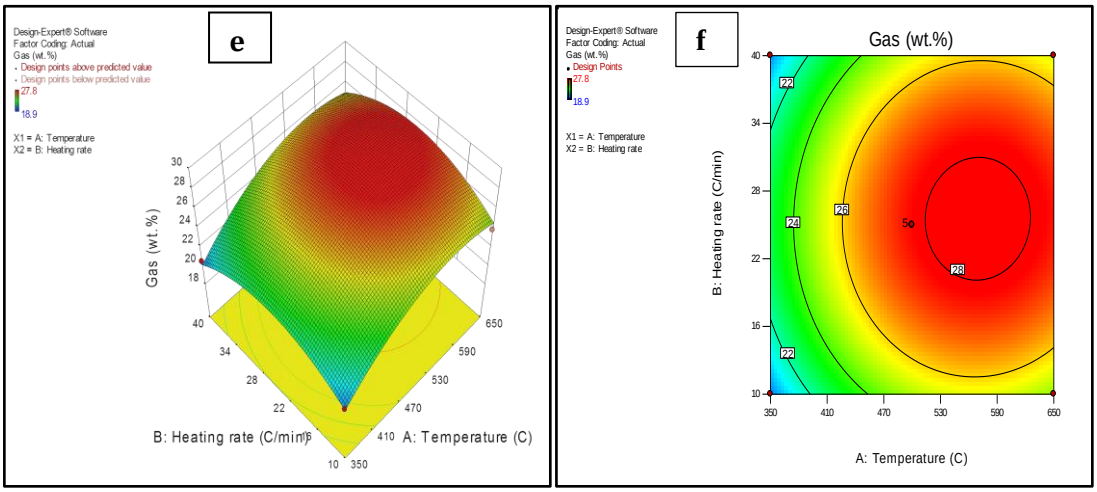

Fig. 4.13: Response surface plots and contour plots of yield percentage of biooil (a, b); biochar (c, d); and gas (e, f) obtained from pyrolysis of MFSC

The Figs. 4.13 (a) and (b) represent the 3–D response surface plot and contour plot of interaction between the temperature (A) and heating rate (B) on the yield percentage of biooil. The 3–D plot clearly indicates that increase of temperature from 350–550 ºC increases the yield of biooil and sudden decline in the response was observed as the temperature further rises to 650 ºC. It can be observed from the Figs. 4.13(a) and (b) that heating rate was a major influential factor that affects oil yield. The red portion on the response surface plots represents the highest yield of biooil whereas the blue and green portions represent the lower yield of biooil. Yellow portion represents effect of temperature and heating rate on the response at an intermediate range. Figs. 4.13(c) and (d) show effect of temperature and heating rate on yield biochar. Lower temperature and heating rate favors the highest yield of biochar which is represented by red portion of the plots. Furthermore, it can be clearly observed from the Figs. 4.13(e) and (f) that yields of gaseous product was completely dependent on pyrolysis temperature whereas heating rate has minor influences.

4-1.6.2. Optimization of MFSC biooil yield

RSM simulation was carried out to find the optimum condition for yield of biooil obtained during pyrolysis of MFSC biomass. For this purpose, temperatures and heating rates were being evaluated and investigated to select the point that can produce the largest volume of pyrolytic liquid. Finally, a solution with highest

desirability (equals to 1) was selected at temperature of 550 ºC and heating rate of 40 ºC/min which was able to provide 28.82 wt.% of biooil yield (shown in Fig. 4.14).

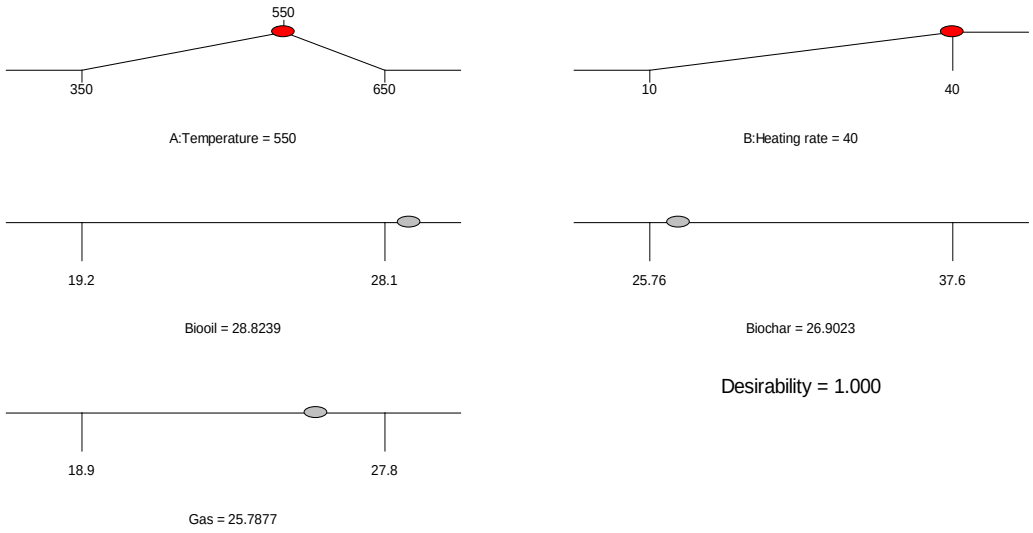

Fig. 4.14: Optimum conditions for highest yield of liquid product from pyrolysis of MFSC

4-1.7. Pyrolysis of PGSC and MFSC biomass

4-1.7.1. Product yield from PGSC and MFSC

RSM analysis suggests that for both PGSC and MFSC biomass the maximum yield of biooil can be obtained at temperature 550 ºC with heating rate of 40 ºC/min. Therefore, in order to obtain the highest yield of biooil, the pyrolysis experiments for both PGSC and MFSC samples were carried out with a temperature increment of 40 ºC/min to the final temperature of 350, 450, 550 and 650 ºC in a fixed bed tubular reactor. The experiments were performed under a constant flow of nitrogen at 100 ml/min with a particle size of 0.2 mm. Figs. 4.15 (a) and (b) show the product yields from the pyrolysis of PGSC and MFSC respectively, whereas Table 4.14 provided corresponding product distributions.

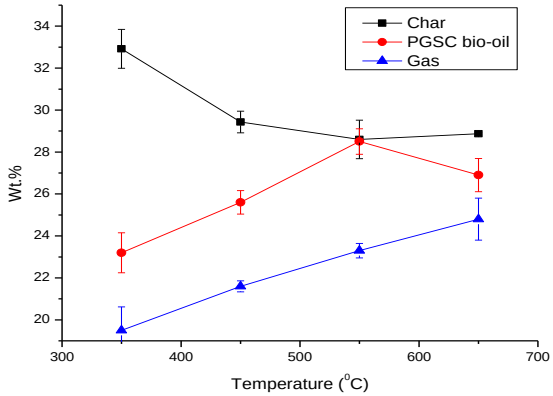

Fig. 4.15: (a) Effect of temperature on solid, liquid and gaseous products of PGSC biomass

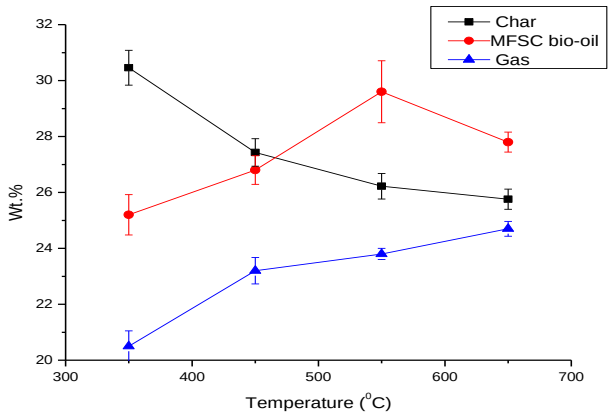

Fig. 4.15: (b) Effect of temperature on solid, liquid and gaseous products of MFSC biomass

Table 4.14: Product distribution of both PGSC and MFSC biomass

PGSC				MFSC		
Temperature (°C)	**Char (wt.%)**	**Biooil (wt.%)**	**Gas (wt.%)**	**Char (wt.%)**	**Biooil (wt.%)**	**Gas (wt.%)**
350	32.92±0.04	23.2±0.11	19.5±0.02	30.46±0.05	25.2±0.09	20.5±0.09
450	29.43±0.05	25.6±0.04	21.6±0.05	27.43±0.04	26.8±0.03	23.2±0.10
550	28.6±0.02	28.5±0.08	23.3±0.03	26.22±0.02	29.6±0.09	23.8±0.02
650	28.87±0.03	26.9±0.05	24.8±0.04	25.76±0.03	27.8±0.02	24.7±0.04

It can be observed from the Table 4.14, that biochar yield decreases from 32.9 wt.% to 28.8 wt.% for PGSC and from 30.4 wt.% to 25.7 wt.% for MFSC biomass with increase in pyrolysis temperature from 350 to 650 ºC. The decrease in biochar yield with increasing temperature could be attributed either due to greater decomposition of organic material at higher temperatures promoting the release of volatile material or due to secondary decomposition of the char residues [27]. Moreover, the rapid heating also leads to a fast deploymerization of solid material to primary volatiles [28].

For MFSC biomass the yield of biooil was found to increase from 25.2 wt.% to 29.6 wt.% corresponding to a rise in temperature from 350 to 550 ºC while a sudden drop in oil yield (27.8 wt.%) was observed at final pyrolysis temperature of 650 ºC. Similarly, for PGSC the maximum oil yield of 28.5 wt.% was obtained at a temperature of 550 ºC, however, the oil yield decreased to 26.9 wt.% at a temperature of 650 ºC. The reason behind the lower yield of biooil at a temperature below 400 ºC may be due to the fact that the temperature rise was not enough for complete pyrolysis to take place, thus yielding less amount of liquid product [27]. Moreover, the decrease of oil yields beyond 550 ºC can be attributed to the fact that higher treatment temperature might lead to more biooil cracking reactions resulting in higher gas yield and subsequently lower oil yield [29-30].

As shown in Figs. 4.15(a) and (b), the gas product yield increased with increase in pyrolysis temperatures. The gas yield increased from 19.5 wt.% to 24.8 wt.% and from 20.5 wt.% to 24.7 wt.% with increase in pyrolysis temperature from 350–650 ºC for PGSC and MFSC biomass respectively. The increase in the gas products is seemed to be predominant due to secondary cracking of the pyrolysis vapors at higher temperatures and heating rates. It was found that the secondary decomposition of char at higher temperatures and heating rates may also produce some non-condensable gaseous products, which also contributes to the increase of the gas yield [30]. Similar interpretation made by other workers has also been observed [27, 31-32]. From the above discussion, the maximum yield of biooil for both PGSC and MFSC samples was obtained at 550 ºC with an increment of temperature 40

ºC/min. Therefore, the biooils obtained at this temperature was subjected for further analysis.

4-1.7.2. Yields of column chromatographic fractions of biooils

The biooil obtained at maximum yield during pyrolysis was further separated by using liquid column chromatography for both PGSC and MFSC samples. Various solvents were used to eluate the compounds dissolved in biooil on the basis of their polarity. First of all the compounds were eluated using non polar solvent, n-hexane which is further followed by toluene, ethyl-acetate and methanol. Weight percentage of various sub-fractions obtained from both PGSC and MFSC biooils were found to be equivalent in amount. Yield of sub-fractions in wt.% basis for both the biooils are shown in Fig. 4.16. The n-hexane fractions of both PGSC and MFSC biooils contained 9 wt.% and 11 wt.% respectively. Yield of toluene and ethyl acetate fractions in both the biooils was found to be relatively more than that of the other two fractions. Finally, methanol was used as solvent for extraction of residual polar compounds present in the biooils (23 wt.% for PGSC and 22 wt.% for MFSC).

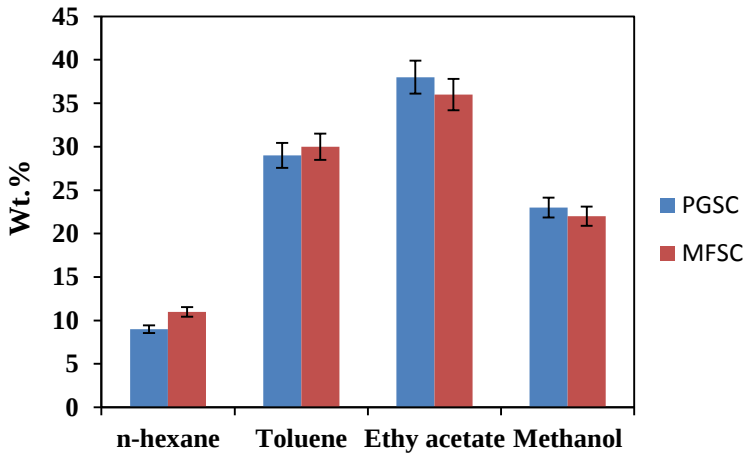

Fig. 4.16: Yields of column chromatographic sub-fractions obtained from PGSC & MFSC biooils

4-1.8. Characterization of biooil

4-1.8.1. Physical characterization of biooil

Table 4.15 shows the elemental composition, calorific value and other physical properties of the liquid product such as density, specific gravity, cloud point, pour point and pH which helps in assessing and determining feasibility of both MFSC and PGSC biooils as liquid fuels. Comparison of physical properties of the biooils with transportation fuels (Table 4.15) reveals that both the biooils have higher density as compared to transportation fuels. High density may adversely affect the pumping and injection quality of the biooils in an engine at lower temperatures and therefore, prospect of blending with commercial transportation fuels needs to be explored. The flash point of the liquid products is in a comparable range with conventional transport fuels which will ensure the safe storage. Pour points of both the biooils are acceptable for most of the climatic conditions. Calorific values of PGSC and MFSC biooils were about 70% and 75% of that of the gasoline and diesel respectively. Calorific values of aliphatic sub-fractions were found to be 34.90 MJ/kg for PGSC and 37.23 MJ/kg for MFSC biooil which were higher than their respective raw biooils. This could be attributed to the exclusion of oxygenated compounds from the biooil during n-hexane separation by using liquid column chromatography. Elemental analysis of biooils obtained from both the feedstock showed that the oxygen contents in the biooils were lower than that of the original feedstock. The decrease in the oxygen contents in the biooils is favorable since high oxygen content results in low energy density (heating value) of biooil as compared to transportation fuel. From the elemental analyses, both PGSC and MFSC biooils were found to have higher values of carbon, hydrogen and nitrogen contents as compared to the original feedstocks, which typically results in higher energy density of biooils. The higher calorific value along with higher values of carbon and hydrogen with low oxygen levels in MFSC biooil corroborates their better fuel properties than PGSC biooil.

Table 4.15: Physico-chemical properties of biooil and its comparison with petro-fuels

Properties	Methods	PGSC biooil	MFSC biooil	Gasoline	Diesel
Appearance		Dark brownish oil	Dark brownish oil	_	_
Density, 15 ºC (kg/m^3)	ASTM D1298-99	0.9580	0.9720	_	_
Specific gravity at 15°C/15 ºC	ASTM D1298-99	0.9583	0.9725	0.72-0.78	0.82-0.85
pH		3.9	3.7	_	_
Pour point (ºC)	ASTM D5853-09	Plus 4	Plus 7	-40	- 40 to -1
Cloud point (ºC)	ASTM D1310-01(2007)	15	25	_	_
Flash point (ºC)	ASTM D6450-05(2010)	42	50	-43	53-80
Fire point (ºC)	ASTM D1310-01(2007)	58	62	_	_
C	_	56.12	60.05	_	_
H	_	6.97	7.11	_	_
N	_	1.83	1.45	_	_
O	_	31.87	29.08	_	_
H/C	_	1.49	1.42	_	_
O/C	_	0.43	0.36	_	_
Empirical formula	_	$C_{35.7}H_{53.3}NO_{15.2}$	$C_{48.3}H_{68.6}NO_{17.5}$	_	_
Calorific value (MJ/kg)	_	29.45	32.63	42–46	42–45

4-1.8.2. FTIR analysis of biooil

FTIR spectra of biooil obtained from pyrolysis of MFSC and PGSC at 550 ºC with heating rate of 40 ºC/min are shown in Figs. 4.17 (a) and (b).

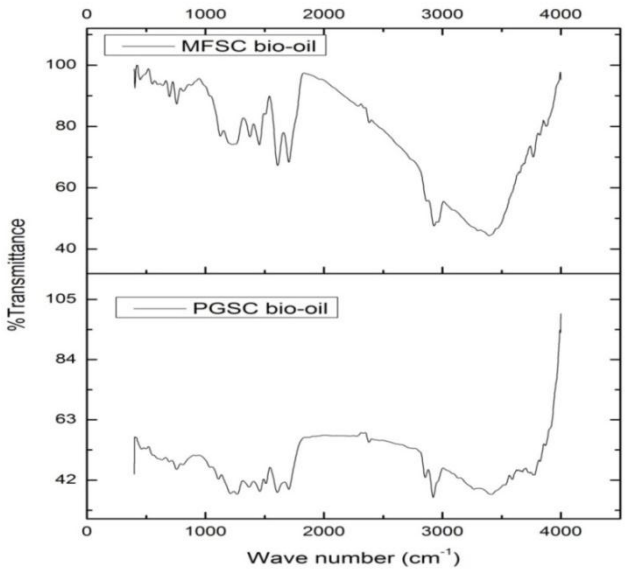

Fig: 4.17. FTIR spectra of (a) MFSC and (b) PGSC biooil

The biooils obtained from pyrolysis of PGSC and MFSC biomasses were further fractionated using liquid column chromatography into four different fractions (n-hexane, toluene, ethyl-acetate and methanol). FTIR spectra for all the sub-fractions obtained from both PGSC and MFSC biooils are shown in Figs. 4.18 and 4.19.

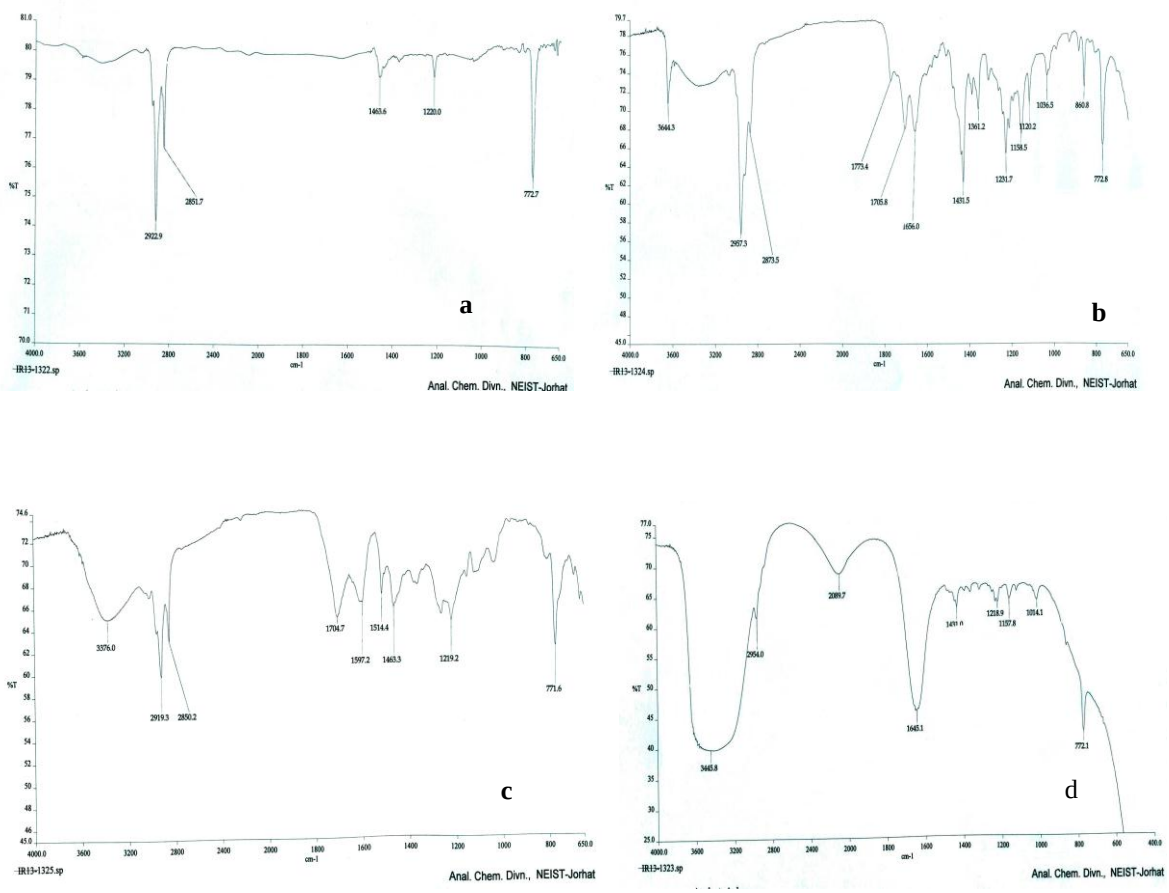

Fig. 4.18: FTIR images of sub-fractions obtained from PGSC biooil after elution of using solvents (a) n-hexane, (b) toluene, (c) ethyl-acetate, and (d) methanol

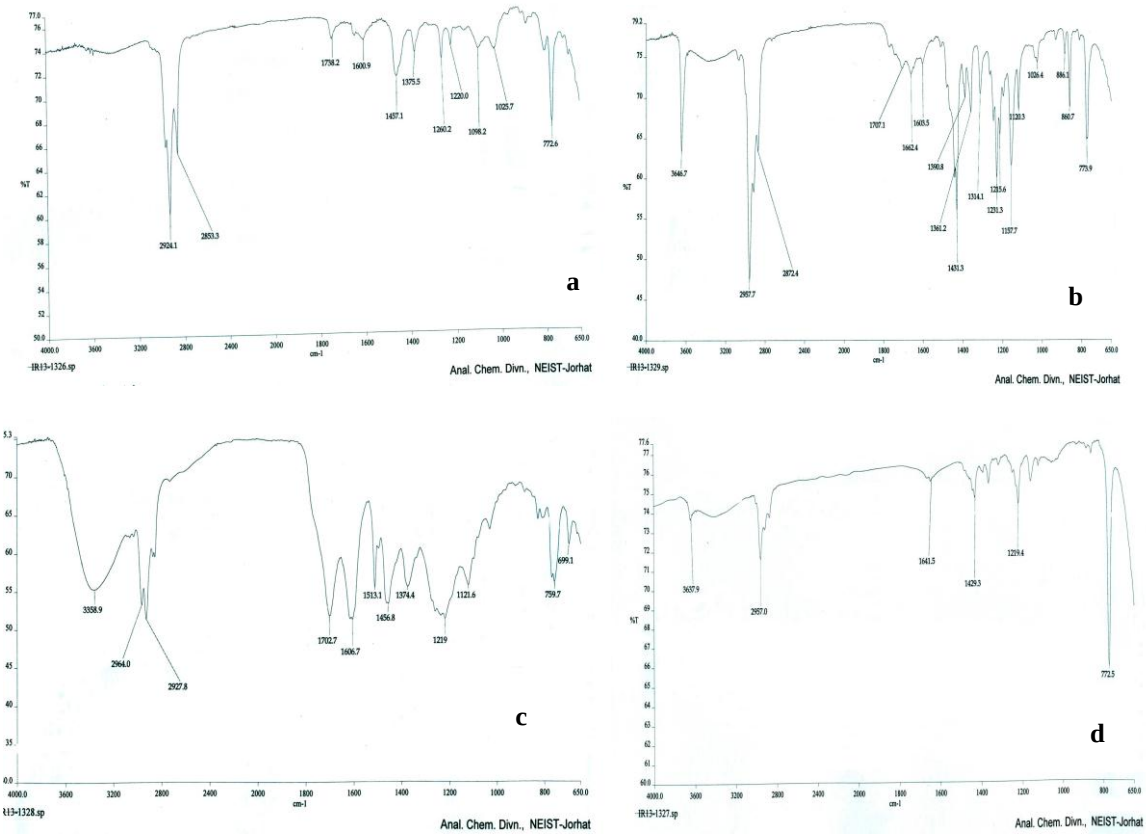

Fig. 4.19: FTIR images of sub-fractions obtained from MFSC biooil after elution of using solvents (a) n-hexane, (b) toluene, (c) ethyl-acetate, and (d) methanol

The absorption peak at 3200–3550 cm^{-1} indicated the presence of oxygenated compounds along with moisture [33]. This band was observed in the toluene and methanol fractions of PGSC and in toluene fractions of MFSC biooil. A sharp peak at 3580–3650 cm^{-1} indicated the presence of free O–H group and this was observed in the ethyl acetate fractions of both the biooils and methanol fractions of MFSC biooil. This band, however, was not observed in the hexane fractions of both the biooils indicating the absence of O–H group in the hexane fractions. This indicated that the fractionation separated the oxygenated compounds from biooils and thereby increased their aliphatic nature. The C–H stretching vibrations between 2850 and 2925 cm^{-1} and C–H deformation vibrations between 1410 and 1515 cm^{-1} indicated the presence of alkanes. Moreover, the location of bending vibration of C–H groups at 1378 cm^{-1} provided another evidence of the fact that this band was very important for the

detection of methyl groups in a given compound [34]. The presence of amines was detected by C–N stretching vibrations between 1080 and 1335 cm^{-1}. The C=O stretching vibrations between 1650 and 1750 cm^{-1} was compatible with the presence of ketone, quinine and aldehyde groups etc. The absorbance of peaks between 1575 and 1675 cm^{-1} representing C=C stretching vibrations was an indicative of alkenes and aromatics [35]. The region between 1210 and 1320 cm^{-1} in methanol sub-fractions of both PGSC and MFSC biooils showed medium C–O stretching vibrations for carboxylic acids and their derivatives. The region between 700 and 900 cm^{-1} contained various bands related to the aromatic, out of plane C–H bending vibrations. The high intensity of the above mentioned bands indicates that the aromatic hydrogen is located in aromatic rings with high degree of substitution [36].

4-1.8.3. ^{1}H NMR analysis of biooil and its sub-fractions

The integral values of selected regions of the 1H NMR spectra for both PGSC and MFSC biooils and their sub-fractions are presented in Table 4.16 on the basis of hydrogen percentage. The corresponding spectra for each sub-fraction are provided in appendix section.

Table 4.16: Percentage of hydrogen based on ^{1}H NMR analysis of PGSC and MFSC biooil sub-fractions

Proton assignment	Chemical Shift (ppm)	PGSC biooil	Hexane	Toluene	EA	MeOH	MFSC biooil	Hexane	Toluene	EA	MeOH
Aromatics	6.5–9.0	22.20	5.70	21.44	19.01	9.98	19.99	12.40	20.09	20.45	14.52
Phenolic OH or olefinic proton	5.0–6.5	7.11	2.22	6.19	17.73	5.10	10.27	2.52	4.35	12.35	5.77
Ring-join methylene (Ar–CH_2–Ar)	3.3–4.5	9.42	1.34	6.60	7.86	12.23	4.49	0.97	3.61	3.80	8.13
CH_3, CH_2, CH α to an aromatic ring	2.0–3.3	24.37	5.31	19.00	25.83	22.51	21.83	12.19	15.45	14.99	29.66
CH_2, CH_β to an aromatic ring (napthenic)	1.6–2.0	4.68	3.55	5.43	7.73	8.84	9.20	9.93	9.16	6.33	4.98
β-CH_3,CH_2, and CHγ or further from an aromatic ring	1.0–1.6	22.99	58.74	31.30	30.48	20.65	18.93	45.90	20.58	15.07	9.33
CH_3γ or further from an aromatic ring	0.5–1.0	4.68	14.65	5.96	5.65	3.62	8.78	15.61	10.94	7.54	4.04

From the Table 4.16, it is evident that there are major differences in the overall chemical composition of the biooils as indicated by different portions of the spectra. The most up field region of the spectra, i.e. from 0.5 to 1.6 ppm, representing aliphatic protons that are attached to carbon atoms, at least two bonds, removed from a C=C double bond or heteroatom (O or N), was more populated for the n-hexane fractions of both PGSC and MFSC biooils (73% for PGSC and 61% for MFSC of all protons) than other biooil fractions and unfractionated biooil, indicating higher aliphatic content in n-hexane fractions of both the biooils. The n-hexane fractions of both the biooils had a higher aliphatic content (shown in Table 4.16.) which accounts for their superior energy content when compared to unfractionated biooils. The aliphatic proton percentages in other fractions (toluene, ethyl acetate and methanol) are lower than hexane fractions.

The next integrated region from 1.6 to 3.3 ppm represents the protons on aliphatic carbon atoms that may be bonded to a C=C double bond (aromatic or olefinic) or are two bonds away from a heteroatom. Lower amount of proton percentage were observed in this region for hexane fractions of PGSC and MFSC biooils than other sub-fractions.

The 3.3–4.5 ppm region of the ^{1}H NMR spectrum could represent protons on carbon atoms next to an aliphatic alcohol or ether, or a methylene group that joins two aromatic rings. The region between 5.0 and 6.5 ppm represents the presence of phenolic OH or olefinic protons. The proton percentage in this region for aliphatic fractions (2.2% for PGSC and 2.5% for MFSC hexane fractions) was quite lower than the other fractions of the biooils and unfractionated biooil. This could be attributed to the fact that fractionation with non-polar solvent separates the oxygenated compounds from the biooils.

The resonances between 6.5 and 9.0 ppm were assigned to aromatic structures. This represents not only those hydrogen atoms in benzenoids, but also those in hetero-aromatics containing O and N. The proton percentages in this region for hexane fractions were quite lower than other fractions (5.7% for PGSC and 12.3% for MFSC). This result showed that hexane fraction consisted mostly hydrocarbon

compounds along with small quantities of other compounds. This result was also consistent with the FTIR result of the hexane fractions. The toluene and ethyl-acetate fractions illustrated almost equivalent amounts of proton percentage in the respective region for both the biooils, as they eluate mostly aromatic compounds including monocyclic and polycyclic aromatic hydrocarbons, phenolic and neutral oxygenated compounds respectively. This interpretation of ^{1}H NMR indicated the presence of phenolic compounds in toluene, and ethyl-acetate fractions of both the biooils. These phenolic derivatives have a high value, as they are used as flavorings in the food industry. Syringol and guaiacol may also be present in biooils in significant concentrations which are useful in the production of biodegradable polyesters and polyethers.

Finally, methanol extracts the polar molecules from the biooil. This methanol extracts showed characteristic peaks in the range of 7.0–8.0 ppm for the amide molecules. Amines, esters, aldehyde, cyanide and nitro group substituted molecules were observed in the region of 0.5–4.5 ppm. It was evident from ^{1}H NMR spectra that aliphatic compounds in the n-hexane fractions of biooils were relatively higher than other fractions. The absence of oxygen content in these fractions was also observed in FTIR spectra. This was also supported by their higher calorific values (34.90 MJ/kg for PGSC and 37.23 MJ/kg for MFSC biooil). Thus, fractionation reduced the disadvantages associated with the highly oxygenated pyrolytic oils.

4-1.8.4. GC-MS analysis of biooil and their sub-fractions

GC–MS analysis was applied to identify the organic compounds present in the both PGSC and MFSC raw biooils and their n-hexane fractions. The compounds present in the biooils were recognized by comparing the chromatograms of PGSC and MFSC biooils and their corresponding n-hexane fractions with standard chromatographic data available from NIST 98 spectrum library. The results showed the complex composition of both the biooils. A complete separation of all the peaks was not possible due to the complicated composition of the biooil. The Total ion chromatograms (TIC) of both PGSC and MFSC raw biooils and their respective n-

hexane fractions are shown in Figs. 4.20, 4.21, 4.22 and 4.23 respectively. TIC of other fractions for both biooils are provided in appendix section.

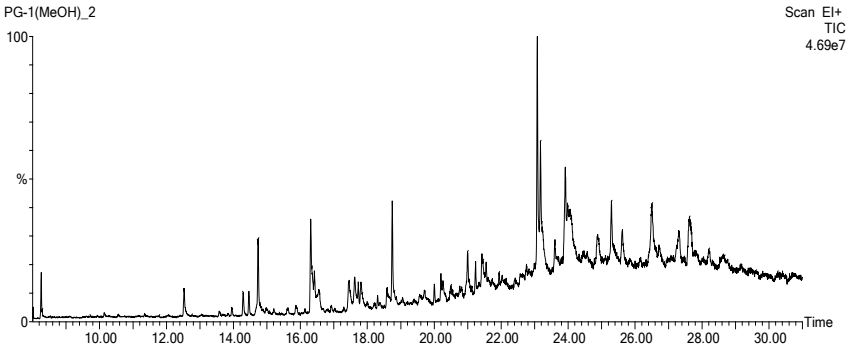

Fig. 4.20: TIC of PGSC biooil

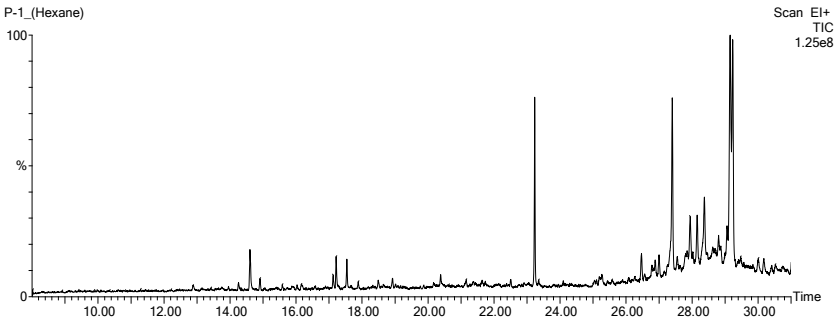

Fig. 4.21: TIC of n-hexane fraction of PGSC biooil

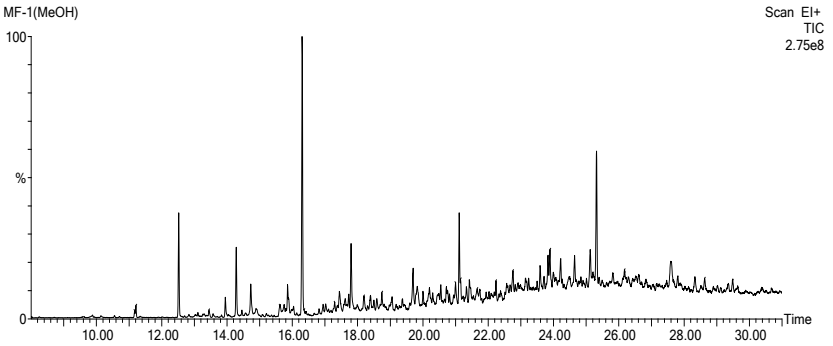

Fig. 4.22: TIC of MFSC biooil

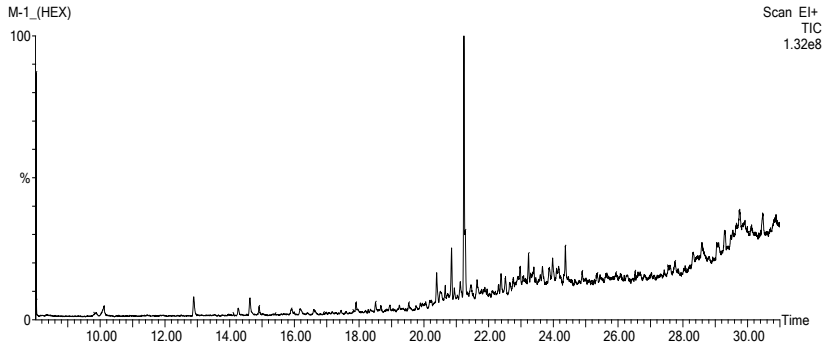

Fig. 4.23: TIC of n-hexane fraction of MFSC biooil

The identified components along with the retention time, compound names and area percentage are shown in Table 4.17. Most of the compounds present in PGSC and MFSC biooils were found to be aromatic and phenolic in nature. Presence of phenols was also evident from FTIR results mentioned in the earlier section. Substituted phenols were present in the biooils as monomeric units and oligomers derived from coniferyl and syringyl building blocks of lignin. Some acid and oxygenated compounds were also found to be present in the raw biooils which were responsible for acidic nature of the biooil. However, the presence of acids in biooil is undesirable due to its corrosive nature. Presence of carbonyl groups (which are oxygenated compounds) can also affect the stability and heating value of biooil. Therefore, these compounds must be detached from biooil structure through efficient separation techniques so as to utilize the biooil effectively. Fractionation of raw biooils using n-hexane as eluent was able to separate mainly aliphatic compounds of biooils. Mostly, three types of compounds were identified in n-hexane fractions: n-alkanes, alkenes and branched hydrocarbons (isoprenoids). The majority of straight-chain alkanes were distributed in the range from C_9–C_{22}; however, some part of the light hydrocarbons may have escaped through evaporation along with the solvent after fractionation. Though alkenes are present in n-hexane fractions, but n-alkanes are dominant. This was probably due to the cracking of branched hydrocarbons to straight chain low molecular hydrocarbons when high heating rate is applied [37].

Table 4.17: Chemical compounds in PGSC and MFSC biooils and their corresponding n-hexane fractions (GCMS)

RT(min)	Compound Name	Area% in			
		MFSC biooil	MFSC n-hexane fraction	PGSC biooil	PGSC n-hexane fraction
8.26	Pyridine	-	-	0.8	0.6
10.12	Styrene		0.9	-	-
12.52	1,3-cyclopentadiene	2.7	-	1.0	-
12.89	Cyclopropane, ethynyl-		1.0		0.4
14.28	furan, 2-(2-propenyl)-	1.9	-	-	-
14.29	Phenol, 2-methyl	-	-	0.6	-
14.46	Acetophenone	-	-	0.5	-
14.60	Pentadecane	-	-	-	1.5
14.63	1-Undecene	-	0.9	-	-
14.73	5-ethyl-2-furaldehyde	1.3	-	-	-
14.74	Phenol, 2-methoxy-	-	-	2.0	-
14.90	1,11- Dodecadine	-	-	-	0.4
15.85	Phenol, 3,5-dimethyl-	1.1	-	0.4	-
16.31	Resorcinol	8.2	-	3.1	-
16.42	2,3-dimethylhydroquinone	-	-	1.3	-
16.54	Phenol, 4-Ethyl-2-Methoxy	-	-	1.5	-
17.13	Docosane	-	-	-	0.4
17.21	Undecane	-	-	-	1.0
17.46	1,2-benzenediol	0.9	-	1.1	-
17.54	Tridecane	-	-	-	1.0
17.62	4-octyne	-	-	0.7	-
17.81	Benzaldehyde, oxime	2.1	-	0.8	-
17.91	1-Tetradecene	-	0.7	-	-
18.50	n-nonadecane	-	-	-	0.3
18.74	Phenol ,2,6-Dimethoxy	0.7	-	2.5	-
18.92	6,9-heptadecadiene	-	-	-	0.4
19.70	Acrylic acid	1.3	-	0.9	-
20.00	2,5-dimethoxybenzyl alcohol	1.0	-	0.6	-
20.20	Eugenol	-	-	0.9	-
20.38	1-pentadecene	-	-	-	0.6
20.39	n-nonylcyclohexane	-	1.2	0.3	-
20.55	Naphthalene	0.8	0.7	-	-
20.85	Hexadecane	-	1.7	-	-
20.99	5-tert-butylpyrogallol	-	0.8	1.8	-
21.00	Toluene	2.9	-	-	-
21.23	Tetradecane	-	9.1	0.5	0.3
21.42	Furan, 2-(1-pentenyl)-	1.0	-	1.3	-
21.64	Dodecane	-	1.1	-	-
22.38	Heneicosane	-	-	-	0.3
23.23	6,8-tetradecadiene	-	-	-	4.6
23.83	3-chloropropionic acid	-	-	-	0.4
24.88	Hydroquinone	0.9	-	-	-
25.29	Caffeine	-	-	-	0.6
26.47	Heptadecane	-	-	-	0.3

Further, the presence of an important compound, “Resorcinol” was observed with high area percentage both in PGSC (3.1) and MFSC (8.2) biooil. The compound has wide application both in medicinal and chemical industries. It can be used as an antiseptic and disinfectant as well as chemical intermediate for the synthesis of

pharmaceuticals and other organic compounds. It is also used in the production of diazo dyes, plasticizers and as a UV absorber in resins.

4-1.9. Characterization of biochar

4-1.9.1. Physico-chemical characterization of biochar

The proximate and elemental compositions of the biochars obtained from the pyrolysis of both PGSC and MFSC biomass at different temperatures with a heating rate of 40 ºC/min are shown in Table 4.18.

Table 4.18: Various properties of biochar co-produced from pyrolysis of PGSC and MFSC samples

Biomass	**PGSC**				**MFSC**			
Properties	**350 ºC**	**450 ºC**	**550 ºC**	**650 ºC**	**350 ºC**	**450 ºC**	**550 ºC**	**650 ºC**
pH	9.25	9.58	9.75	10.61	7.17	7.25	8.97	9.70
EC (mʊ)	0.973	1.206	1.639	1.967	0.202	0.280	0.898	1.176
Moisture content (wt.%)	2.60	2.00	1.20	0.80	2.90	2.10	1.60	1.10
Ash content (wt.%)	10.09	11.86	12.08	12.39	8.20	9.10	10.80	11.5
Volatile content (wt.%)	19.03	14.09	13.21	10.25	21.85	18.30	15.60	12.22
Fixed Carbon (wt.%)	68.28	72.05	73.51	76.56	67.05	70.50	72.00	75.18
C (wt.%)	61.90	67.4	73.7	78.21	63.5	69.28	74.2	79.1
H (wt.%)	3.62	2.73	1.89	1.63	4.29	3.6	2.11	1.83
N (wt.%)	2.1	1.53	1.82	1.33	0.62	0.92	1.19	0.48
O (wt.%)	31.6	28.1	21.6	18.6	31.2	25.06	22.16	17.8
H/C Molar ratio	0.70	0.49	0.31	0.25	0.81	0.62	0.34	0.28
O/C Molar ratio	0.38	0.31	0.22	0.18	0.37	0.27	0.22	0.17
Calorific Value(MJ/ kg)	22.83	25.39	28.09	28.95	26.89	29.11	29.31	30.37

Proximate analysis was performed to measure the moisture content, volatile matter, fixed carbon and ash content present within the produced biochars. The moisture contents of the biochars were found to decrease with increasing pyrolysis severity from 350–650 ºC. It can be observed from the Table 4.18 that biochar produced at low pyrolysis temperature has enriched volatile matter composition than biochar produced at higher temperature. Volatile matter content decreased from 19.03 to 10.25 wt.% and 21.85 to 12.22 wt.% for PGSC biochar and MFSC biochar respectively as the pyrolysis temperature increased from 350–650 ºC. The high volatile matter content of biochars at relatively low temperature is due to the presence of lignin in the biomass, which can partially resist pyrolytic decomposition at 350 ºC,

but not at higher temperatures [38]. Ash content of both PGSC and MFSC biochars were found to increase with increasing temperature from 350–650 ºC. This increase in ash content was the consequence of enhanced concentration of minerals and destructive volatilization of lignocellulosic matters with increase of temperature [39]. The minerals present in biomass are left as ash after pyrolysis. This is likely to be related to the increase in relative concentrations of Ca, Mg, K, P, S and Zn in ash content as the temperature increased [40]. The values of fixed carbon (FC) content of the biochar were found to increase with the severity in terminal temperatures (Table 4.18.) and corresponding decrease in char yield for all the experiments (Fig. 4.15(a) and (b) for PGSC and MFSC respectively). FC content of biochars significantly increased from 68.28–76.56 wt.% for PGSC and 67.05–75.18 wt.% for MFSC as the temperature rose from 350–650 ºC. It is well known that fixed carbon is the solid combustible residue that remains after a particle sample is carbonized and volatile matter is expelled. Thus, it is used to estimate the number of carbonaceous substances that will be yielded from a solid sample [41]. The C, H, N and O contents of biochar from MFSC and PGSC biomass at different temperatures are shown in Table 4.18. From the table, it is evident that an increase in the temperature resulted in a larger loss of H and O compared to that of C. The H/C and O/C atomic ratios decreased with an increase in terminal temperatures, which might be due to increase in proportion of aryl C [42] and carbonization of biochars [43].

A Van-Kravelen diagram was plotted by using H/C and O/C ratios of biochars obtained at different temperatures for both PGSC and MFSC samples and are shown in Figs. 4.24(a) and (b) respectively. Specifically, H/C and O/C ratios are used to measure the degree of aromaticity and carbonization. It was observed that atomic H/C and O/C ratios of biochars decreased with an increase in pyrolysis temperature from 350 to 650 ºC for both samples. This decrease may be due to dehydration, decarboxylation and decarbonylation. The oxygen containing functionalities are decomposed by decarbonylation and decarboxylation followed by transformation to the alkyl aryl C–C bonds as a cross linking between small aromatic rings [44]. It was observed that biochars obtained at higher temperatures are situated in the region of anthracite coal, the lower H/C ratio of biochars indicates the higher aromaticity.

Aromatized biochar is resistant to decomposition and becomes recalcitrant, meaning it could persist in soil for many years and a strong tool for C-sequestration [45]. These changes also influence the change occurred in calorific value of biochar.

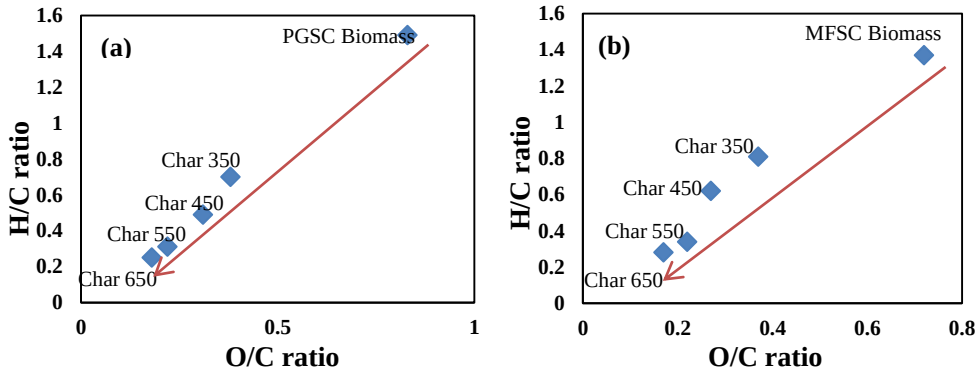

Fig 4.24: Van-Krevelen diagram of (a) PGSC and (b) MFSC biochars obtained at different temperatures.

As shown in Table 4.18, the pH value of biochars increased with temperature, probably as a consequence of the relative concentration of non-pyrolyzed inorganic elements which are present in the original feedstocks [38]. Biochars produced at higher temperature becomes more alkaline in nature probably due to the concomitant decrease in acidic functional groups (due to influence of pyrolysis temperature). The basicity of biochar arises from the presence of salts such as carbonates and chlorides of K and Ca, in addition to oxygen free functional groups. Increase in biochar's pH with temperature is also associated with the increase in the ash content. Biochar with high pH may correct the soil acidity problem and therefore, may be used as a liming agent. Amplifying the soil pH results in increased base saturation (Ca and Mg concentrations) and increased soil microbial activity [45].

The values of electrical conductivity (EC) of biochars obtained from PGSC and MFSC were found to increase with increase in pyrolysis temperature. The EC has been used to give an indication for the salinity of the biochar. Incorporation of biochar into acidic soil caused an increase in EC due to release of weakly bound nutrients of biochars into the soil solution, which are available for plant uptake [46]. But biochar with higher EC when applied to soil, it may increase soil salinity and subsequently

provide undesirable impacts on the plant growth by reducing water uptake and cause nutrient imbalance due to increased salinity [47]. Therefore, EC of biochar is an important parameter which must be taken into consideration prior to biochar application as a soil amendment. Though biochar with high pH may be desirable for reclamation of highly acidic soils, but, may also harm the soil due to its high EC. Terminal temperature used in biochar preparation is therefore crucial for its applicability as soil amendment.

4-1.9.2. Carbon sequestration potential of biochar

Carbon sequestration potential (CSP) is one of the most important characteristics of biochar, particularly regarding its long-term stability in soil. Higher CSP means higher resistance ability of biochar against both biotic and abiotic degradation. A new recalcitrance index, the R_{50}, for assessing biochar quality for carbon sequestration is proposed. The R_{50} is based on the relative thermal stability of a given biochar to that of graphite. Table 4.19 shows the R_{50} index and CSP of the biochars obtained at different temperatures for both PGSC and MFSC samples and a comparison with R_{50} index of other biochars.

Table 4.19: R_{50} index and CSP values of biochars obtained at different temperatures for both PGSC and MFSC samples and a comparison with R_{50} index of other biochars

Biomass	**Temperature (ºC)**	**R_{50}**	**CSP%**	**Biomass**	**R_{50}**
PGSC	350	0.47	38.1	**Rape straw [47]**	
	450	0.53	34.2	450	0.45
	550	0.58	36.8	550	0.46
	650	0.64	39.0	650	0.48
MFSC	350	0.55	41.5	**Vine shoot [47]**	
	450	0.61	35.8	-	-
	550	0.72	37.9	550	0.44
	650	0.78	40.9	650	0.46

The recalcitrance increased from 0.47 to 0.64 and 0.55 to 0.78 for PGSC biochar and MFSC biochar respectively with an increase in pyrolysis temperature from 350–650 ºC. This increase might be attributed to increase in aromatic C in biochar with temperature [49]. Aromatized biochar is resistant to decomposition and becomes recalcitrant, meaning it could persist in soil for many years and a strong tool

for C-sequestration [44]. Thus, biochar produced at lower temperature had lower recalcitrance which indicated that it can be easily mineralized by microorganism compared to biochar produced at higher temperature.

4-1.9.3. SEM analysis of Biochar

The surface morphology of the biochar was studied by Scanning Electron Microscopy (SEM). It is used for high magnification imaging. SEM images taken at 2000× magnification for both PGSC and MFSC biochars produced at 350º, 450º and 550 ºC with a heating rate of 40 ºC/min are shown in Fig. 4.25 and Fig. 4.26 respectively. The SEM images revealed that with increase in temperature, decomposition of feedstock increased and the underlying layers became more exposed resulting in improved porosity of the biochar. The presence of pores in the biochar indicated that volatile components were formed and released during thermal decomposition [23]. The SEM images confirmed the heterogeneous structure of the biochars obtained from both the samples. The MFSC biochar showed some rough texture with some erratic hollow structure whereas PGSC biochar showed heterogeneous distribution of some undeveloped pores in rolling surface. Further processing of these biochars might be helpful to use as activated carbon or as a support material for solid catalysts.

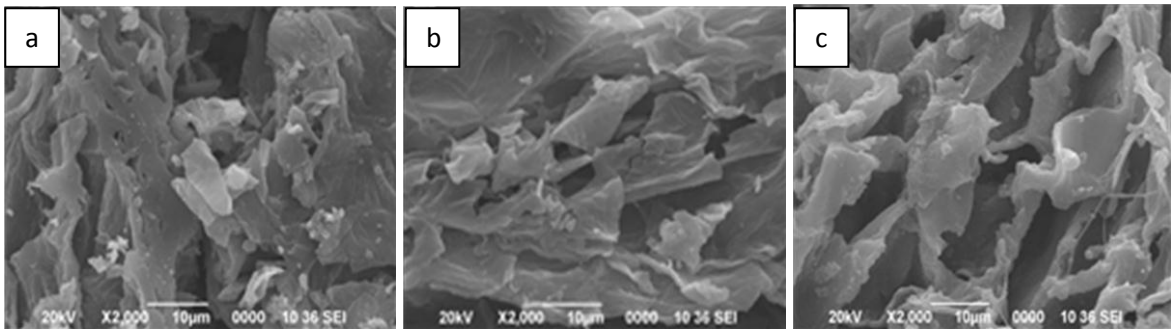

Fig. 4.25: SEM images of MFSC biochars obtained at (a) 350 ºC (b) 450 ºC and (c) 550 ºC

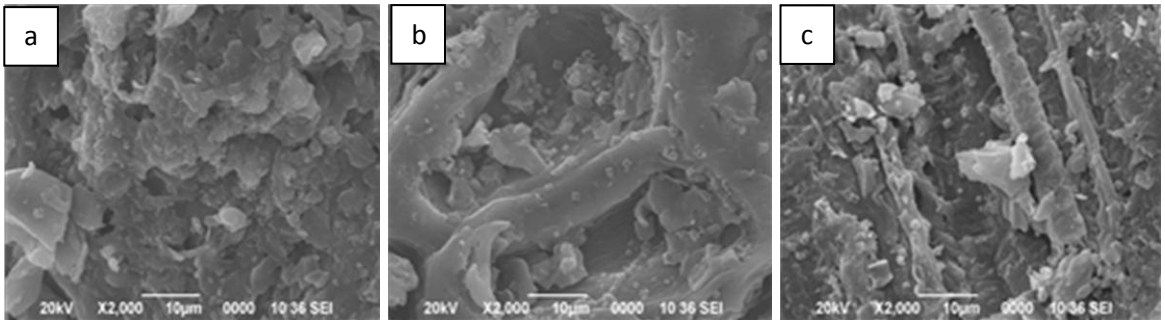

Fig. 4.26: SEM images of PGSC biochars obtained at (a) 350 ºC (b) 450 ºC and (c) 550 ºC

respectively. The EDX spectrum of the MFSC biochar surface (Fig. 4.27) identified the same elements as detected by the elemental analysis of biochar sample (Table 4.20). The EDX analysis indicated that the biochar produced at high temperature consisted of high content of carbon element along with small percentage of oxygen. The hydrogen present in the original biomass was not observed on the biochar surface, which may be released during thermal decomposition of biomass at 550 ºC. Moreover, some other elements such as Mg, Al, K, Ca, Mn and Fe were also found to be present in trace amount on the surface of the biochar.

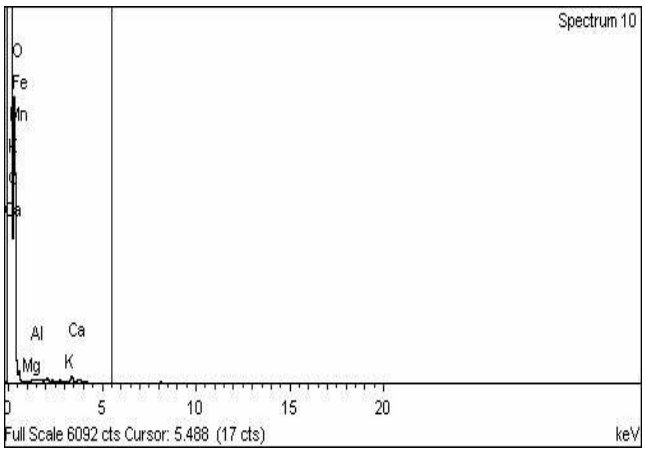

Table 4.20: Elemental composition of MFSC biochar produced at 550 ºC obtained from EDX analysis

Element	Weight %	Atomic %
C	89.51	92.46
O	9.19	7.13
Mg	0.14	0.07
Al	0.03	0.02
K	0.42	0.13
Ca	0.41	0.13
Mn	0.06	0.01
Fe	0.24	0.05
Totals	100.00	

Fig.4.27. EDX spectrum of MFSC biochar produced at 550 ºC

Similarly, EDX spectrum of PGSC biochar and percentage compositions of the elements present on the surface are shown in Fig. 4.28 and Table 4.21 respectively. The EDX spectrum shows the presence of C in the highest amount and O, Mg, Al, K, Ca, Mn and Fe are found to be in trace amount on the surface of the

biochar. Thus, EDX analysis supports the presence of higher amount of aromatic carbon in both the PGSC and MFSC biochars derived at higher temperature.

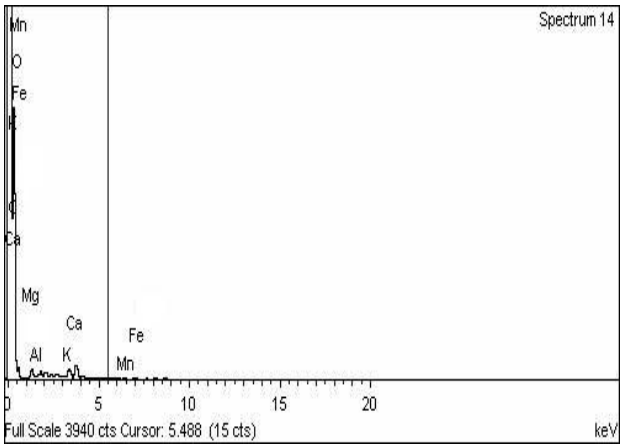

Table 4.21: Elemental composition of PGSC biochar produced at 550 ºC obtained from EDX analysis

Element	Weight %	Atomic %
C	87.46	91.29
O	9.81	7.74
Mg	0.53	0.28
Al	0.04	0.02
K	0.52	0.17
Ca	1.37	0.43
Mn	0.07	0.02
Fe	0.20	0.05
Totals	100.00	

Fig. 4.28: EDX spectrum of PGSC biochar produced at 550 ºC

4-1.9.4. FTIR analysis of biochar

Various functional groups present in the biochars obtained from the pyrolysis of both PGSC and MFSC at different temperatures (350º, 450º, 550º and 650 ºC) were detected by FTIR spectra and are shown in Figs. 4.29(a) and (b) respectively.

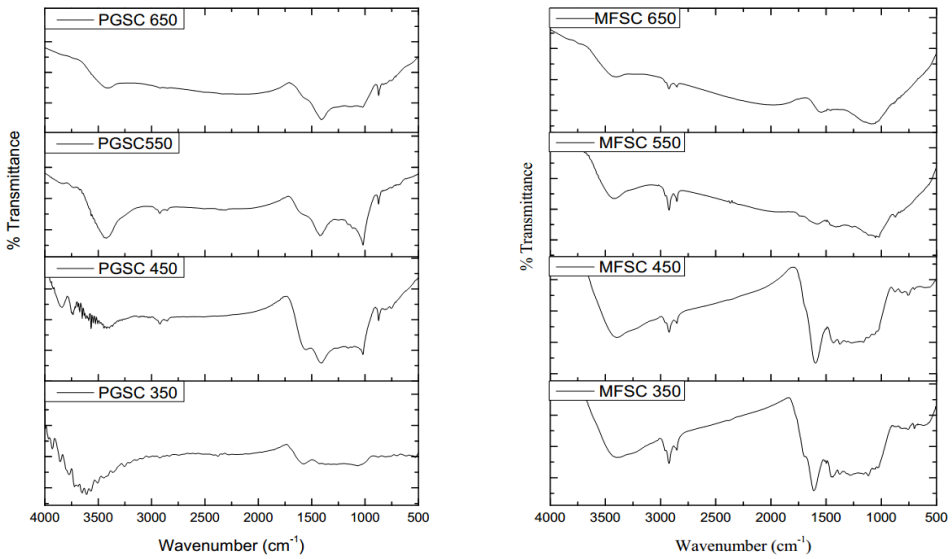

Fig 4.29: FTIR of (a) PGSC and (b) MFSC biochar obtained at different temperatures

The spectra revealed that biochar is a complex arrangement of chemical bonds consisting of mixture of minerals and organic matters. The broad peaks around 3600–

3700 cm^{-1} occurred due to the presence of O–H groups along with moisture content. N–H group present in the organic matter showed the vibration around 3276-3300 cm^{-1}. At 1550–1653 cm^{-1}, the C=O stretching vibrations were identified. It can be observed from the Figs. 4.29(a) and (b), that in both the samples, the intensity of O–H peaks started to decrease with increase in temperature from 350 to 650 ºC suggesting that organic OH and NH groups were very unstable at high temperatures. Further, the decrease in intensity of O–H peaks might be due to the loss of oxygen content occurred during pyrolysis at higher temperature and phenolic-aromatic structures were also cracked to leave behind a carbonaceous solid product. The bands at 2954 cm^{-1} and 2847 cm^{-1} correspond to aliphatic CH_3 asymmetric and CH_2 symmetric stretching vibration respectively, which was further confirmed by the vibration around 1432 cm^{-1}. Aromatic and hetero-aromatic compounds were also confirmed by C–H bending vibrations in the region between 800–600 cm^{-1}. The intensity of these peaks increased with increase in temperature from 350–650 ºC. This indicated stability of the aromatic and hetero-aromatic compounds and possible cyclisation occurred within biochar produced at higher temperature [50].

4-1.9.5. XRD analysis of biochar

The X-ray diffraction (XRD) patterns of the biochars obtained at different temperatures for both PGSC and MFSC biochar samples were investigated and are shown in Figs. 4.30(a) and (b) respectively. XRD is a broadly used technique for analyzing the biomass crystallinity and the biochar structure [51]. The XRD spectra of biochar showed a broad peak of the 2θ values at around 20–30, which were assigned to the crystalline region of cellulose in sample. With increase in temperature from 350–650 ºC, these peaks became broader indicating that some partial crystalline structure of cellulose was lost in the biomass [52]. The appearance of the peaks for biochar, indicated the development of increasingly carbonized material [53] and gives evidence of presence of graphitic structure in the biochar. This peak comes from the formation and successive ordering of aromatic carbon in the biochar [52]. The presence of higher amount of aromatic compound in the biochar as evidenced from FTIR spectra was further supported by the XRD pattern.

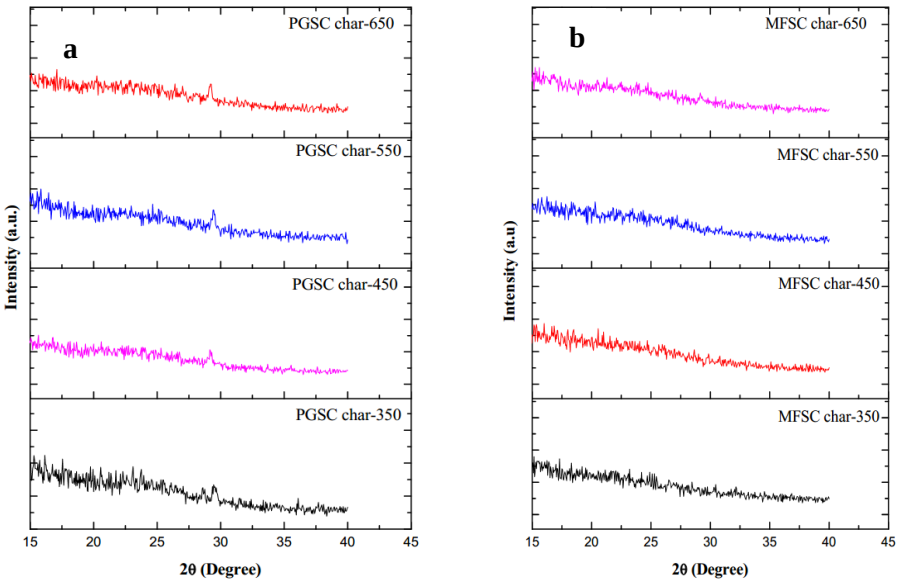

Fig. 4.30: XRD patterns of biochars obtained at different temperatures for (a) PGSC and (b) MFSC biomass

4-1.10. Summary

Present investigation aims to explore the pyrolytic valorization of two selected bio-wastes (MFSC and PGSC) for fuels and chemicals. Physicochemical characterizations and thermal degradation behavior of two samples was carried out by using Thermo-gravimetric analysis (TGA) in order to evaluate the entire degradation process of the two samples during pyrolysis. Activation energy was determined by using three model free methods viz. Friedman, FWO and KAS. It was evident that for both MFSC and PGSC biomass the activation energy values obtained by the Friedman method were little lower than the values of activation energies obtained by the FWO and KAS methods. These differences could be due to the approximation of the temperature integral that was used in the derivations of the relations that ground the FWO and KAS methods and because of this fact the FWO and KAS methods involve a systematic error in E_a which is not the case in the Friedman method. Thus, the activation energies obtained as a function of the conversion from the Friedman method are more reliable than those obtained from the FWO and KAS methods.

Chapter - 4 (a)

The effect of pyrolysis temperature and heating rate on product yield was predicted by a simulation technique named Response surface methodology based on Central composite design matrix which was again verified experimentally. Both MFSC and PGSC samples were subjected to pyrolysis at temperature range of 350-650 ºC with heating rate of 40 ºC /min. Maximum yield of liquid product was obtained 29.6 wt.% for MFSC and 28.5 wt.% for PGSC biomass at temperature 550 ºC with heating rate of 40 ºC/min. With increase in temperature, the liquid product yield increases upto 550 ºC, while a sudden drop in oil yield was observed at final pyrolysis temperature of 650 ºC. Biochar yield found to be decreased with rise in temperature from 350-650 ºC.

Calorific values of both the biooils were found to be higher than original feedstocks. This might be due to the fact that biooils were characterized by lower oxygen content than that of original biomass feedstock. Presence of high oxygen content is not favorable for liquid product in terms of storage and usage. Therefore, biooil obtained at optimum condition for both the samples were further separated by using a liquid column chromatography by using solvents of different polarity (n-hexane, toluene, ethyl-acetate and methanol). Thus, the oxygenated compounds can be separated from the biooil and further the biooil can be categorized into three individual chemical classes viz. aliphatic, aromatic and polar, by using chromatography technique. Moreover, the biooil and their sub-fractions were analyzed for different physical and chemical properties by using different chromatographic and spectroscopic technique such as FT-IR, ^{1}H NMR and GC/MS. The solid co-product of pyrolysis i.e. biochar obtained at different temperatures were also investigated for different physical and chemical properties in order to estimate their suitability for fuel and other applications.

References:

1. Kushwah, Y. S., Mahanta, P. and Mishra, S. C. Some studies on fuel characteristics of *Mesua ferrea*. *Heat Transfer Engineering*, 29(4): 405-409, 2008.
2. Ministry of New and Renewable Energy, Govt. of India, 2009.
3. Dwivedi, G., Jain, S. and Sharma, M. P. Pongamia as a source of biodiesel in India. *Smart Grid and Renewable Energy*, 2(3):184-189, 2011.
4. Sarma, A.K. *Biodiesel Production from Mesua ferrea L (Nahar) and Pongamia glabra Vent (Koroch) Seed Oil*. Ph.D. thesis, Department of Energy, Tezpur University, India, 2006.
5. Choudhury, N.D., Chutia, R.S., Bhaskar, T. and Kataki, R., Pyrolysis of jute dust: effect of reaction parameters and analysis of products. *Journal of Material and Cycles Waste Management*, 16 (3): 449–459, 2014.
6. Demirbas, A. Effects of temperature and particle size on bio-char yield from pyrolysis of agricultural residues. *Journal of Analytical and Applied Pyrolysis*, 72(2): 243-248, 2004.
7. Janse, A. M. C., Westerhout, R. W. J. and Prins, W. Modelling of flash pyrolysis of a single wood particle. *Chemical Engineering and Processing: Process Intensification*, 39(3): 239-252. 2000.
8. Chutia, R.S., Kataki, R. and Bhaskar, T. Thermogravimetric and decomposition kinetic studies of *Mesua ferrea* L. deoiled cake. *Bioresource Technology*, 139: 66–72, 2013.
9. Tripathi, M., Sahu, J. N. and Ganesan, P. Effect of process parameters on production of biochar from biomass waste through pyrolysis: A review. *Renewable and Sustainable Energy Reviews*, 55: 467-481, 2016.
10. Cortés, A. M. and Bridgwater, A. V. Kinetic study of the pyrolysis of miscanthus and its acid hydrolysis residue by thermogravimetric analysis. *Fuel Processing Technology*, 138: 184-193. 2015.
11. Damartzis, T., Vamvuka, D., Sfakiotakis, S. and Zabaniotou, A. Thermal degradation studies and kinetic modeling of cardoon (Cynara cardunculus) pyrolysis using thermogravimetric analysis (TGA). *Bioresource Technology*, 102(10): 6230-6238, 2011.

12. Welker, C. M., Balasubramanian, V. K., Petti, C., Rai, K. M., DeBolt, S. and Mendu, V. Engineering plant biomass lignin content and composition for biofuels and bioproducts. *Energies*, *8*(8): 7654-7676, 2015.
13. Slopiecka, K., Bartocci, P. and Fantozzi, F. Thermogravimetric analysis and kinetic study of poplar wood pyrolysis. *Applied Energy*, 97: 491-497, 2012.
14. Ceylan, S. and Topçu, Y. Pyrolysis kinetics of hazelnut husk using thermogravimetric analysis. *Bioresource Technology*, 156: 182-188, 2014.
15. Manya, J. J., Velo, E. and Puigjaner, L. Kinetics of biomass pyrolysis: a reformulated three-parallel-reactions model. *Industrial and Engineering Chemistry Research*, 42(3): 434-441, 2003.
16. Uzun, B. B. and Yaman, E. Thermogravimetric characteristics and kinetics of scrap tyre and Juglans regia shell co-pyrolysis. *Waste Management and Research*, 32(10): 961-970, 2014.
17. Grønli, M. G., Várhegyi, G. and Di Blasi, C. Thermogravimetric analysis and devolatilization kinetics of wood. *Industrial and Engineering Chemistry Research*, 41(17): 4201-4208, 2002.
18. Crespo, A., Naranjo, A., Burgos, J. C. V., Sanchez, C. G. and Sanchez, E. M. S. Thermogravimetric analysis of thermal and kinetic behavior of acacia mangium wood. *Wood and Fiber Science*, 47(4): 1-9, 2015.
19. Aboulkas, A., El Harfi, K., Nadifiyine, M. and El Bouadili, A. Thermogravimetric characteristics and kinetic of co-pyrolysis of olive residue with high density polyethylene. *Journal of Thermal Analysis and Calorimetry*, 91(3): 737-743, 2008.
20. Cai, J.M., Wu, W.X., Liu, R.H. and Huber, G.W. A distributed activation energy model for the pyrolysis of lignocellulosic biomass. *Green Chemistry* 15(5): 1331-1340, 2013.
21. De Filippis, P., de Caprariis, B., Scarsella, M. and Verdone, N. Double Distribution Activation Energy Model as Suitable Tool in Explaining Biomass and Coal Pyrolysis Behavior. *Energies* 8(3): 1730-1744, 2015.
22. Carrier, M., Auret, L., Bridgwater, A. and Knoetze, J.H. Using apparent activation energy as a reactivity criterion for biomass pyrolysis. *Energy and Fuels* 30: 7834-7841, 2016.

23. Dong, Z. and Cai, J. Isoconversional kinetic analysis of sweet sorghum bagasse pyrolysis by modified logistic mixture model. *Journal of the Energy Institute*, 2017. https://doi.org/10.1016/j.joei.2017.04.006.
24. Wu, W., Mei, Y., Zhang, L., Liu, R. and Cai, J. Effective activation energies of lignocellulosic biomass pyrolysis. *Energy and Fuels* 28(6): 3916-3923, 2014.
25. Poletto, M., Dettenborn, J., Pistor, V., Zeni, M. and Zattera, A. J. Materials produced from plant biomass: Part I: evaluation of thermal stability and pyrolysis of wood. *Materials Research*, 13(3): 375-379, 2010.
26. Yan, Q., Toghiani, H., Yu, F., Cai, Z., and Zhang, J. Effects of pyrolysis conditions on yield of bio-chars from pine chips. *Forest Products Journal*, 61(5): 367-371, 2011.
27. Onay, O. Influence of pyrolysis temperature and heating rate on the production of bio-oil and char from safflower seed by pyrolysis, using a well-swept fixed-bed reactor. *Fuel Processing Technology*, 88(5): 523-531, 2007.
28. Haykiri-Acma, H., Yaman, S. and Kucukbayrak, S. Effect of heating rate on the pyrolysis yields of rapeseed. *Renewable Energy*, 31(6): 803-810, 2006.
29. Pütün, A.E., Uzun, B.B., Apaydin, E. and Pütün, E. Bio-oil from olive oil industry wastes: pyrolysis of olive residue under different conditions. *Fuel Processing Technology*, 87 (1): 25–32, 2005.
30. Şensöz, S., Demiral, İ. and Gerçel, H. F. Olive bagasse (*Olea europea L.)* pyrolysis. *Bioresource Technology*, 97(3): 429-436, 2006.
31. Luo, Z.,Wang, S., Liao, Y., Zhou, J., Gu, Y. and Cen, K. Research on biomass fast pyrolysis for liquid fuel. *Biomass Bioenergy*, 26(5): 455-462, 2004.
32. Horne, P. A. and Williams, P. T. Influence of temperature on the products from the flash pyrolysis of biomass. *Fuel*, 75(9): 1051-1059, 1996.
33. Pütün, A. E., Özcan, A. and Pütün, E. Pyrolysis of hazelnut shells in a fixed-bed tubular reactor: yields and structural analysis of bio-oil. *Journal of Analytical and Applied Pyrolysis*, 52(1): 33-49, 1999.
34. Apaydin-Varol, E., Uzun, B. B., Önal, E. and Pütün, A. E. Synthetic fuel production from cottonseed: Fast pyrolysis and a TGA/FT-IR/MS study. *Journal of Analytical and Applied Pyrolysis*, 105: 83-90, 2014.

35. Gercel, H. F. The production and evaluation of bio-oils from the pyrolysis of sunflower-oil cake. *Biomass and Bioenergy*, 23(4): 307-314, 2002.
36. Ozbay, N., Pütün, A. E. and Pütün, E. Bio- oil production from rapid pyrolysis of cottonseed cake: product yields and compositions. *International Journal of Energy Research*, 30(7): 501-510, 2006.
37. Pütün, E., Uzun, B. B. and Pütün, A. E. Production of bio-fuels from cottonseed cake by catalytic pyrolysis under steam atmosphere. *Biomass and Bioenergy*, 30(6): 592-598, 2006.
38. Jindo, K., Mizumoto, H., Sawada, Y. and Sonoki, T. Physical and chemical characterization of biochars derived from different agricultural residues. *Biogeosciences*, 11(23): 6613-6621, 2014.
39. Joseph, S., Bachmann, R. T., Shang, Z., Long, R. L., Rafiq, M. T. and Rafiq, M. K. Influence of pyrolysis temperature on physico-chemical properties of corn stover (zea mays l.) biochar and feasibility for carbon capture and energy balance. *PLoS One*, 11(6): 1-17, 2016.
40. Melo, L. C., Coscione, A. R., Abreu, C. A., Puga, A. P. and Camargo, O. A. Influence of pyrolysis temperature on cadmium and zinc sorption capacity of sugar cane straw–derived biochar. *BioResources*, 8(4): 4992-5004, 2013.
41. Verma, M., Godbout, S., Brar, S. K., Solomatnikova, O., Lemay, S. P., and Larouche, J. P. Biofuels production from biomass by thermochemical conversion technologies. *International Journal of Chemical Engineering*, 2012.
42. Baldock, J. A. and Smernik, R. J. Chemical composition and bioavailability of thermally altered Pinus resinosa (Red pine) wood. *Organic Geochemistry*, *33*(9):1093-1109, 2002.
43. Fu, P., Yi, W., Bai, X., Li, Z., Hu, S. and Xiang, J. Effect of temperature on gas composition and char structural features of pyrolyzed agricultural residues. *Bioresource Technology*, 102(17): 8211-8219, 2011.
44. Yuan, H., Lu, T., Zhao, D., Huang, H., Noriyuki, K., Chen, Y., 2013. Influence of temperature on product distribution and biochar properties by municipal sludge pyrolysis. *Journal of Material Cycles and Waste Management*, 15(3): 357–361, 2013.

45. Ok, Y. S., Uchimiya, S. M., Chang, S. X., and Bolan, N. (Eds.). *Biochar: Production, Characterization, and Applications*. CRC Press, 2015.
46. Chintala, R., Mollinedo, J., Schumacher, T. E., Malo, D. D. and Julson, J. L. Effect of biochar on chemical properties of acidic soil. *Archives of Agronomy and Soil Science*, 60(3): 393-404, 2014.
47. del Martínez-Ballesta, M. C., Silva, C., López-Berenguer, C., Cabanero, F. J. and Carvajal, M. Plant aquaporins: new perspectives on water and nutrient uptake in saline environment. *Plant Biology*, 8(05): 535-546, 2006.
48. Gómez, N., Rosas, J. G., Singh, S., Ross, A. B., Sánchez, M. E., & Cara, J. (2016). Development of a gained stability index for describing biochar stability: Relation of high recalcitrance index (R50) with accelerated ageing tests. *Journal of Analytical and Applied Pyrolysis*, 120, 37-44.
49. Spokas, K. A., Koskinen, W. C., Baker, J. M. and Reicosky, D. C. Impacts of woodchip biochar additions on greenhouse gas production and sorption/degradation of two herbicides in a Minnesota soil. *Chemosphere*, 77(4): 574-581, 2009.
50. Hossain, M. K., Strezov, V., Chan, K. Y., Ziolkowski, A. and Nelson, P. F. Influence of pyrolysis temperature on production and nutrient properties of wastewater sludge biochar. *Journal of Environmental Management*, 92(1): 223-228, 2011.
51. Ertaş, M. and Alma, M. H. Pyrolysis of laurel (Laurus nobilis L.) extraction residues in a fixed-bed reactor: Characterization of bio-oil and bio-char. *Journal of Analytical and Applied Pyrolysis*, 88(1): 22-29, 2010.
52. Kim, K. H., Kim, J. Y., Cho, T. S. and Choi, J. W. Influence of pyrolysis temperature on physicochemical properties of biochar obtained from the fast pyrolysis of pitch pine (Pinus rigida). *Bioresource Technology*, 118: 158-162, 2012.
53. Keiluweit, M., Nico, P. S., Johnson, M. G. and Kleber, M. Dynamic molecular structure of plant biomass-derived black carbon (biochar). *Environmental Science and Technology*, 44(4): 1247-1253, 2010.

Chapter – 4 (b)

4-2.1. Introduction

In recent years microalgae has received growing interest as a source of renewable fuel because of their high productivity, high oil content and the ability to grow in non-potable water such as waste and sea water, and on non-arable areas [1]. Utilization of microalgae as a renewable source of fuel was an old concept proposed during late fifties particularly for producing biogas only. Later production of liquid fuel has received an increased attention due to the reasons mentioned earlier [2]. However, conversion of microalgae to biofuels is still a challenge as extraction of lipid from microalgae and subsequent trans-esterification is a costly process. The process requires acid catalysts to convert free fatty acids present in microalgae into fatty acids esters [3]. Further, during production of algal biodiesel, only oil fraction can be utilized and the rest is considered as waste in terms of fuel use [4]. Recently, an alternative conversion method, pyrolysis (a thermo-chemical conversion method), has received increasing attention in conversion of whole microalgae biomass into liquid fuel [5]. Along with the liquid product pyrolysis can transform the biomass in the form of solid and gaseous fuel also. Since, microalgae biomass has a very different chemical composition as compared to lignocellulosic feedstock therefore, the biooil produced from pyrolysis of microalgae may contain different types of compounds such as linear hydrocarbons and nitrogenous species resulting from pyrolysis of lipids and proteins, respectively [6]. Several microalgae strains have been reported concerning the pyrolytic characteristics of microalgae but only a few studies have been carried out by using microalgae species *Scenedesmus dimorphus* as the feedstock.

Among the various strains of microalgae, *S. dimorphus* is appeared to be an ideal species due to their high growth ability and tolerance capability at different environmental conditions. *S. dimorphus* has acquired mounting interest as a source of biofuel due to its relatively high lipid content, efficient and economic combination of CO_2 fixation ability, and wastewater treatment potential [7]. In the present investigation, microalgae species, *S. dimorphus* was being studied as a potential feedstock for thermo-chemical conversion. The effect of pyrolysis temperature on product yield was also studied. The liquid products were analyzed for different

physical and chemical properties by using different chromatographic and spectroscopic technique such as FT- IR, ^{1}H NMR and GC/MS. The solid co-product of pyrolysis i.e. biochar obtained at different temperatures were also analyzed for different physical and chemical properties.

4-2.2. Physico-chemical characterization of *S. dimorphus*

The raw *S. dimorphus* microalgae contain almost 76 percent of water. For the present investigation dried *S. dimorphus* sample was collected from Defense Research Laboratory, Tezpur, India. The chemical composition, proximate and ultimate analysis of microalgae species *S. dimorphus* are shown in Table 4.22.

Table 4.22: Physicochemical properties of *S. dimorphus* biomass

Properties	Raw Biomass
Proximate analysis (dry basis)	
Moisture Content (wt.%)	0.083
Ash Content (wt.%)	17.33
Volatile matter (wt.%)	51.45
Fixed C (wt.%)	31.13
Ultimate analysis (dry basis)	
C (wt.%)	52.60
H (wt.%)	6.21
N (wt.%)	8.75
O (wt.%)	31.92
H/C	1.42
O/C	0.46
HHV (MJ/Kg)	19.0
Protein content (wt.%)	53.13
Lipid content (wt.%)	10.23
Carbohydrate content (wt.%)	22.90

It can be observed from the Table 4.22 that *S. dimorphus* has very low amount of dry moisture content (0.08 wt.%) which is necessary to ensure the sustained combustion of the biomass. The *S. dimorphus* has high percentage of ash content (17.33 wt.%) and is consistent with previous observations made by other researchers that high ash content is present in aquatic flora from natural ecosystems, including micro and macro algae [8–9]. This might be due to the presence of the inorganic component in the biomass [10]. The biomass has the volatile matter (VM) of 51.45 wt.% and fixed carbon content (FC) of 31.13 wt.%. VM includes those compounds

which were driven-off as volatiles during heating while FC refers to the remaining constituents after the releases of volatiles. Percentage of FC and VM represent the available chemical energy that biomass is able to release [11]. The carbon, hydrogen and nitrogen contents in the algal biomass were found to be 52.60 wt.%, 6.21 wt.% and 8.75 wt.% respectively obtained on dry basis. Oxygen content was calculated by difference. The H/C and O/C values were calculated from elemental composition as 1.42 and 0.46 respectively. Higher value of H/C indicates the presence of higher amounts of aliphatic hydrocarbon compounds as compared to polar compounds in the biomass. The protein, lipid and carbohydrate are the biochemical components of microalgae, which follows the decomposition order like:

Lipids > proteins > carbohydrates

It was reported that lipids, proteins and carbohydrates has contribution towards the formation of oil yields as 80–55 wt.%, 18–11 wt.% and 15–6 wt.% respectively [12]. Protein and carbohydrate fractions in microalgae biomass are directly associated with the presence of nitrogen and oxygen contents respectively. The nitrogen content of the *S. dimorphus* was significantly higher than that of lignocellulosic biomass which was probably due to the presence of protein content in sample [13]. Similarly, oxygen content can correlate with the presence of carbohydrate fraction in biomass [12].

4-2.3. Thermo-gravimetric analysis

A thermogravimetric analyzer was used to monitor the degradation of the biomass. The TG and DTG curves at three different heating rates 10, 20 and 30 ºC/min for microalgae species *S. dimorphus* are shown in Figs. 4.31 and 4.32. Three main phases were observed during the thermochemical conversion of the aquatic species, and the results concord with recent thermal degradation studies of macro and microalgae [14]. The first phase involved a dehydration process and occurred at temperatures lower than 180 ºC, during this phase slight loss weight was occurred due to elimination of free/bound moisture and light volatile extractives that was loosely bound to the biomass was lost [15]. Second phase started from temperature 180 º to 550 ºC where most of the organic material decomposed. This phase was referred to as

active pyrolysis region which can be further divided into two zones. The first zone with less prominent shoulder denoted the decomposition of proteins and carbohydrates while the second zone with a sharp peak denoted the decomposition of lipids [16]. In the third phase (T>550 ºC), slow decomposition of the solid residue was was indicated by a gradual mass loss in TG curve (shown in Fig. 4.31). In this zone, highly non-volatile carbon compounds were vaporized forming CO and CO_2 due to the high temperatures [17]. The third phase is known as passive pyrolysis zone slow degradation of carbonaceous product resemble to gasification. Detailed kinetic studies have been carried out to estimate the various parameters using TG–DTG curves.

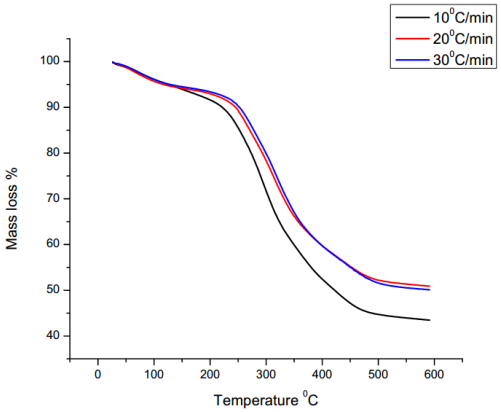

Fig. 4.31: TG of weight loss curves of *S. dimorphus* recorded at three heating rates.

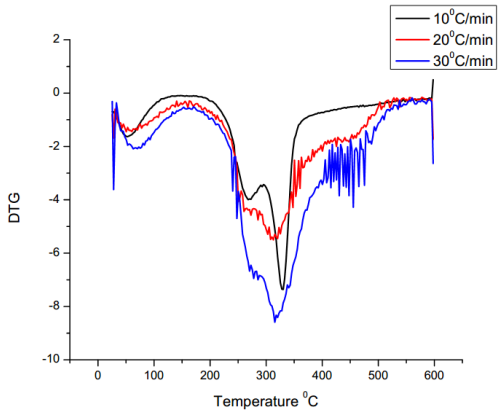

Fig. 4.32: DTG curves of *S. dimorphus* biomass recorded at three different heating rates

The effect of heating rate on certain temperature range of the pyrolysis can be observed from the TG curves (shown in Fig. 4.31). Usually, TG curves are seemed to be shifted towards the right hand side of the plot with increase in heating rate. However, in case of *S. dimorphus*, an overlap was observed in between the TG curves obtained at heating rates of 20 and 30 ºC/min. The values of characteristic temperatures for all the heating rates related to active pyrolysis zone (S_{II}) are given in Table 4.23. It can be observed from the Table 4.23 that onset and offset temperatures (T_{onset} and T_{offset}) were laterally shifted to higher temperature with increasing heating rate. But there was a slight decrease in temperature for maximum mass loss rates (T_{max}) with increasing heating rate. The DTG curve showing the changes that occurred in lateral shift with different heating rate are shown in Fig. 4.32.

Table 4.23: Characteristic temperatures for *S. dimorphus* in active pyrolysis zone (S_{II})

Heating rate (ºC/min)	**S_{II}**		
	T_{onset}	**T_{max}**	**T_{offset}**
10	169	330	525
20	174	322	538
30	178	312	558

The model-free methods, Friedman, FWO and KAS analysis are applied to study the kinetic analysis when experimental data is represented as the set of measurements at three different heating rates. The model-free methods provide information on kinetic parameters, such as the activation energy (E_a) and frequency factor without determining a concrete kinetic model.

4-2.3.1. Friedman method

Friedman is a differential iso-conversional method described by using the eq. (3.7) given in chapter 3. This method was employed at heating rates of 10, 20 and 30 ºC/min, for conversions ranging from 0.1 to 0.9, to determine the changes in activation energy with conversion during the thermal devolatilization process. The mass loss as a function of temperature, conversion, and heating rate using Friedman method was plotted against $\ln(d\alpha/dt)$ vs. $1/T$ is shown in Fig. 4.33. A set of straight lines were obtained at different conversions, with the slope of each line being equal to

($-E_a/R$). Activation energies can be calculated from the slope, frequency factors and correlation coefficients are listed in Table 4.24.

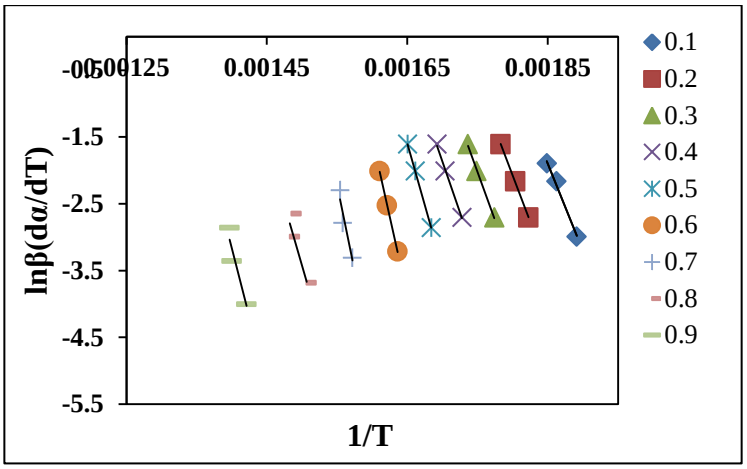

Fig. 4.33: Plots obtained by Friedman method for determination of activation energy of *S. dimorphus* at S_{II}

Table 4.24: Kinetic parameters obtained from the Friedman plot for *S. dimorphus*

Conversion, α	Activation energy, E_a (kJ/mol)	Intercepts	Frequency factor	R^2
0.1	218.12	46.64	1.80E+20	0.9931
0.2	230.62	47.85	6.03E+20	0.9995
0.3	240.94	48.69	1.39E+21	0.9974
0.4	253.80	50.03	5.34E+21	0.9974
0.5	307.61	59.45	6.58E+25	1
0.6	391.70	73.85	1.75E+34	0.9997
0.7	433.60	78.62	1.39E+34	0.9110
0.8	304.91	51.58	2.51E+22	0.8368
0.9	341.67	54.36	4.05E+23	0.8915

It can be observed from the Table 4.24 that correlation coefficients were in the range 0.90 to 1 for all correlated lines and values of activation energy varied from 218 to 433 kJ/ mol. At the initial stage of dehydration the lowest activation energy was observed which was followed by an increase in activation energy. This might be due to the high energy requirement for degradation of hemicellulose and cellulose present in the algal biomass. Increase in activation energy till the initial 0.7 conversion is

because of the requirement of startup energy for degradation of algal biomass constituents [15].

4-2.3.2. Flynn-Wall-Ozawa (FWO) method

FWO is an integral iso-conversional method used for calculating activation energy from (eq. 3.8 in chapter 3) the slope of the straight lines obtained by plotting lnβ vs 1/T shown in Fig. 4.34. Activation energy values, correlation coefficients and frequency factors of the degradation at various conversions α are listed in Table 4.25.

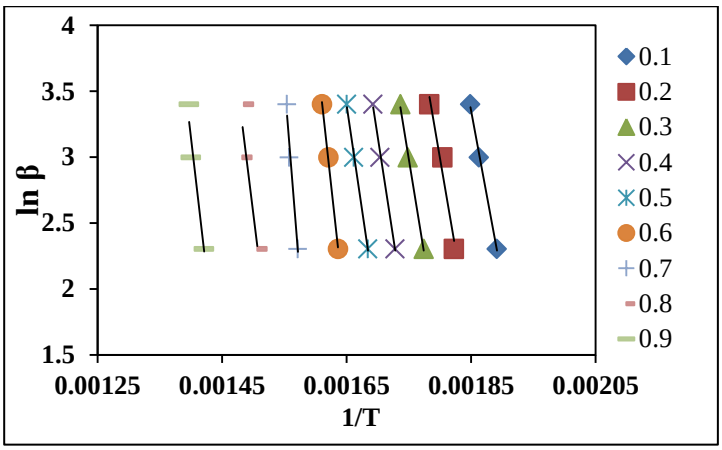

Fig. 4.34: Plots obtained by FWO method for determination of activation energy of *S. dimorphus* at S_{II}

Table 4.25: Kinetic parameters obtained from the FWO plot for *S. dimorphus*

Conversion, α	Activation energy, E_a (kJ/mol)	Intercepts	Frequency factor	R^2
0.1	223.26	50.57	9.16E+21	0.9973
0.2	241.33	52.64	7.26E+22	0.9670
0.3	253.47	53.70	2.09E+23	0.9974
0.4	267.00	55.04	8.00E+23	0.9974
0.5	280.88	56.38	3.05E+24	0.9974
0.6	378.49	73.11	5.63E+31	0.9978
0.7	516.66	95.12	2.04E+41	0.9693
0.8	330.65	59.28	5.55E+25	0.8052
0.9	355.69	60.07	1.22E+26	0.9328

Similar to Friedman method it can be observed from the Table 4.25 that activation energy of *S. dimorphs* increases from 223 to 516 kJ/mol as the degree of

conversion increases from 0.1 to 0.7 and then decrease to 355 kJ/mol with increase in conversion up to 0.9. Correlation coefficients were also varied within the range of 0.8052 to 0.9974.

4-2.3.3. Kissinger-Akira-Sunnose (KAS) method

KAS is another isoconversional method adopted to calculate the activation energy (eq. 3.11 in chapter 3). A series of straight lines were obtained from the plot of $\ln(\beta/T^2)$ vs. 1/T with slope of $-E_a/R$ for different value of conversion (α). The KAS plot is shown in Fig. 4.35 and various kinetic parameters were listed in Table 4.26.

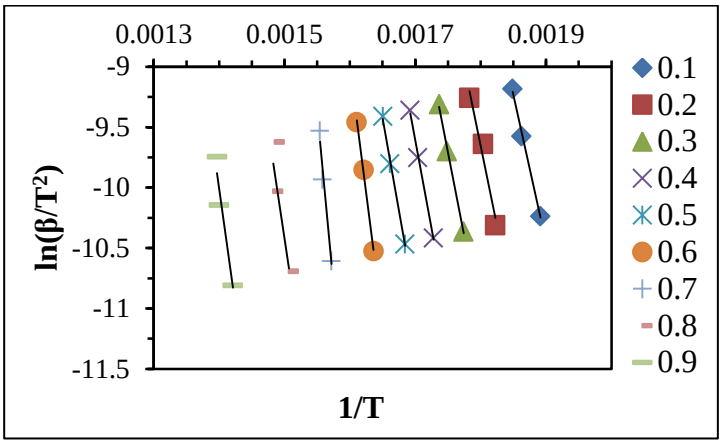

Fig. 4.35: Plots obtained by KAS method for determination of activation energy of *S. dimorphus* at S_{II}

Table 4.26: Kinetic parameters obtained from the KAS plot for *S. dimorphus*

Conversion, α	Activation energy, E_a (kJ/mol)	Intercepts	Frequency factor	R^2
0.1	203.34	36.01	4.35E+15	0.9971
0.2	220.17	38.01	3.21E+16	0.9642
0.3	231.47	39.01	8.74E+16	0.9972
0.4	244.08	40.30	3.17E+17	0.9972
0.5	257.03	41.59	1.15E+18	0.9972
0.6	349.54	58.26	2.00E+25	0.9977
0.7	480.49	80.20	6.76E+34	0.9680
0.8	303.19	44.27	1.68E+19	0.7936
0.9	326.31	44.94	3.28E+19	0.9282

It can be observed from the Table 4.26 that activation energy of *S. dimorphus* estimated by KAS method increased as the conversion degree of the microalgae biomass raise from of 0.1–0.7. But a downward trend was spotted for activation energy for α interval of 0.7–0.9. This illustrates the relationship between the activation energies and the conversion occurred due to continuous change of decomposition mechanisms. With the increase of conversion, the release of volatiles and secondary reaction helped to form gas and porous solid residues. First of all improved diffusion of the gases are responsible for lower activation energy in the conversion interval. But in the later stage, formation of porous solid residues made the diffusion faster and leads to little increase in activation energy or significantly decreases in activation energy in the corresponding conversion interval. All the three isoconversional methods show similar trend of variation regarding the changes occurred in activation energy of biomass. These methods have the advantage that they do not require previous knowledge of the reaction mechanism to determine the activation energy suggests that the model free methods used are reliable in determining the activation energy [18].

4-2.4. Statistical optimization using Response surface model for *S. dimorphus*

RSM was performed for microalgae species *S. dimorphus* in order to establish a model interrelated with two independent variables such as temperature and heating rate by using Central composite design (CCD). Dependent variables such as yield of biooil, biochar and gas are regarded as responses. Second order polynomial equation describes the overall relationship between all the variables. A total of 13 experimental runs were performed to establish a model suggested by CCD matrix and their values are shown in Table 4.27. Based on Sequential Model Sum of Squares' [Type I] highest order polynomial was selected where additional model terms were significant and the model was not distorted. Analysis of variance (ANOVA) was used to test the data obtained from the experiments then establishes a suitable and significant model.

Table 4.27: Design matrix using Central Composite Design and experiment results

		Factor 1	Factor 2	Response 1	Response 2	Response 3
Std	**Run**	**A:Temperature**	**B:Heating rate**	**Biooil**	**Biochar**	**Gas**
7	1	500	3.7868	20.2	35.15	25.4
3	2	350	40	23.2	32.92	23.68
13	3	500	25	26.3	31.3	29.4
2	4	650	10	22.9	32.7	30.8
10	5	500	25	26.3	31.3	29.4
11	6	500	25	26.3	31.3	29.4
9	7	500	25	26.3	31.3	29.4
12	8	500	25	26.3	31.3	29.4
5	9	287.868	25	15.6	40	21.2
6	10	712.132	25	24.4	28.9	33.2
8	11	500	46.2132	27.4	32.68	29.9
1	12	350	10	17.9	40.13	22.3
4	13	650	40	26.9	28.87	31.8

The equations related to the yield percentage of the products during decomposition are shown below in terms of coded factors.

$$\boldsymbol{Biooil} = +26.78 + 2.57 \times A + 2.45 \times B - 0.48 \times AB - 3.25 \times A^2 - 1.23 \times B^2 \quad (1)$$

$$\boldsymbol{Biochar} = +31.30 - 3.40 \times A - 1.82 \times B + 0.84 \times AB + 1.44 \times A^2 + 1.18 \times B^2 \quad (2)$$

$$\boldsymbol{Gas} = +29.40 + 4.20 \times A + 1.09 \times B - 0.095 \times AB - 1.17 \times A^2 - 0.95 \times B^2 \quad (3)$$

The interaction between the independent variables as well as significance of each model term was established by analysis of variance (ANOVA) and the results obtained are presented in Table 4.28.

Table 4.28: Results of ANOVA for *S. dimorphus*

Products	**Biooil**			**Biochar**			**Gas**		
	Sum of Sqs.	F value	p-value Prob>F	Sum of Sqs.	F value	p-value Prob>F	Sum of Sqs.	F value	p-value Prob>F
Model	486.08	**72.20**	< 0.0001	260.55	**68.67**	< 0.0001	122.93	**97.20**	< 0.0001
A-Temperature	198.59	147.48	< 0.0001	163.53	215.48	< 0.0001	121.47	192.09	< 0.0001
B-Heating rate	94.63	70.28	< 0.0001	39.08	51.50	0.0002	1.46	2.31	0.1597
AB	6.00	4.46	0.0726	13.91	18.33	0.0036	-	-	-
A^2	156.96	116.56	< 0.0001	1.06	1.39	0.2762	-	-	-
B^2	49.78	36.97	0.0005	44.00	57.98	0.0001	-	-	-
Residual	9.43	-	-	5.31	-	-	6.32	-	-
Lack of Fit	9.43	-	-	5.31	-	-	6.32	-	-
Pure Error	0.000	-	-	0.000	-	-	0.000	-	-
R^2	0.9810			0.9800			0.9511		
Adj-R^2	0.9674			0.9657			0.9413		

The ANOVA analysis suggests a quadratic model with presence of maximum variability in the observed data. The model F-value indicated a significant quadratic model for the observed data. Addition of supplementary terms to a model always increases model coefficient R^2 value, regardless of the significance of the added terms. Thus, a large R-squared value may not always imply a significant model. It can be observed from the Table 4.28, the model F-values of 72.20, 68.67 and 97.20 implies the models for biooil, biochar and gaseous products respectively are significant. There is only a 0.01 % chance that a model F-value this large could occur due to noise for all three responses. Since the values of "Prob>F'' less than 0.05% indicates the significance of model terms. Further, the "Prob>F" values greater than 0.1 indicate the model terms are not significant. Presence of many non-significant model terms (except the terms required supporting hierarchy) supports the elimination in order to achieve an improved model. In case of biooil, A, B, A^2 and B^2 are significant model terms. Similarly, for biochar the significant model terms are A, B, AB and B^2 and for gaseous product only A is the significant model term. The high values of the determination coefficient (R^2) and the adjusted determination coefficient (adjusted R^2) also showed that the significance of the models. Adequate precision (Adeq-Precision) value measures the signal to noise ratio and ratio more that 4 are

desirable. Adeq-Precision values for *S. dimorphus* derived biooil, biochar and gas are found to be 21.655, 28.920 and 28.851 respectively indicating adequate signal and the model can be used to navigate the design space.

4-2.4.1. Response surface plots for S. dimorphus

The three dimensional surface plots and contour plots for biooil, biochar and gas yield are shown in Figs. 4.36(a), (b) and (c) respectively. The plots demonstrate the effect of interaction between the two variables temperature and heating rate on yield percentage of pyrolytic products at temperature range of 300–600 ºC and heating rate of 10–40 ºC/min.

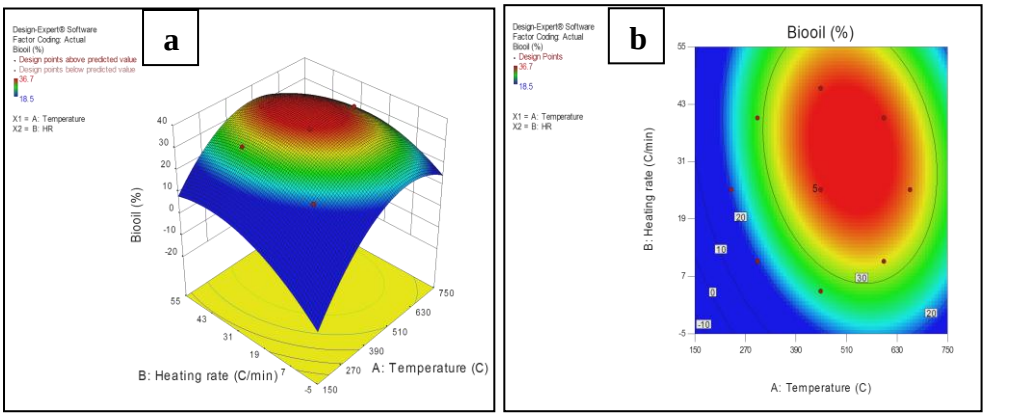

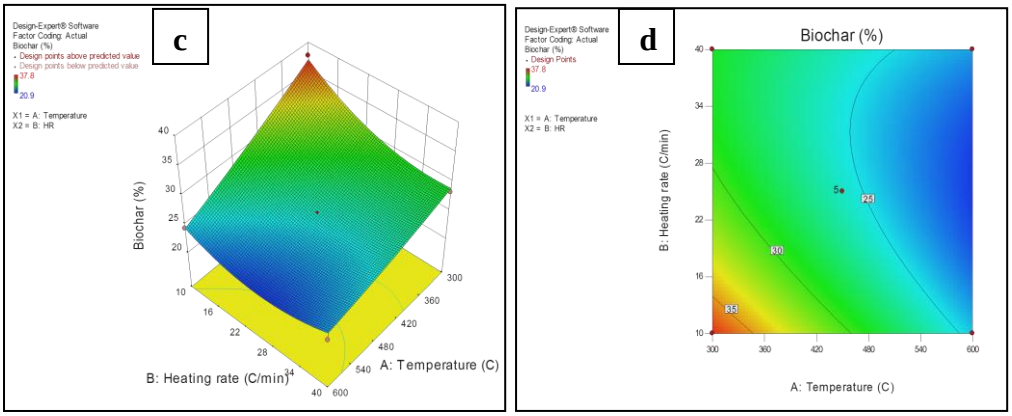

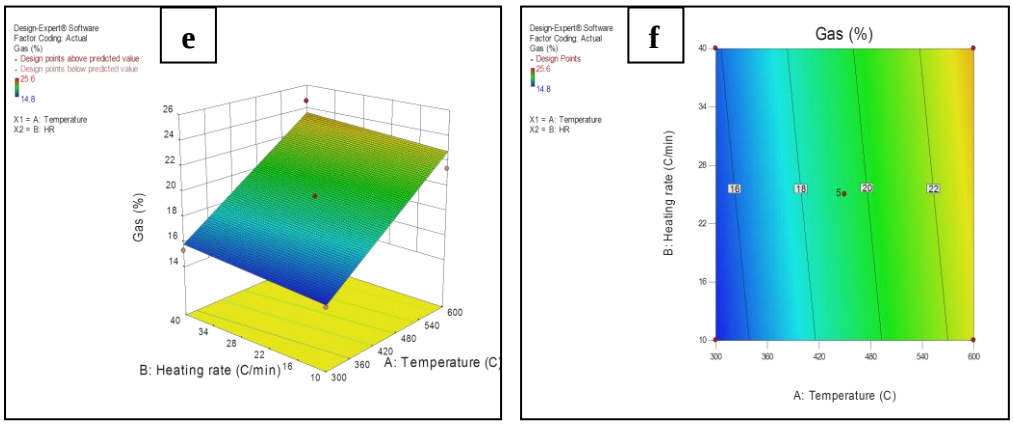

Figs. 4.36: Response surface plots and contour plots of yield percentage of biooil (a, b); biochar (c, d); and gas (e, f) obtained from pyrolysis of *S.dimorphus*

The 3–D surface plots and corresponding contour plot of response vs. two variables at same time are shown in Figs. 4.36(a-f). The Figs. 4.36(a) and (b) revealed the effect of interaction between the temperatures (A) and heating rate (B) on the yield percentage of biooil obtained from the pyrolysis of *S. dimorphus*. These figures indicate that both the temperature and heating rate has marked effect on yield percentage of biooil. Biooil yield found to be increased with increase of temperature from 300 to 500 ºC, however, there was a gradual decline in the response was observed if the temperature further rises to 600 ºC. Moreover, contour plot of biooil (Fig. 4.36(b)) also showed that maximum yield of biooil could be obtained at temperature below 600 ºC with high heating rate. Thus, it can be estimated that both temperature and heating rate has marked effect on biooil yield. The red portion on the response surface plot represents the highest yield of biooil. Blue and green portions of the plots distinctly represent the effect of variables on the response at lower values. On the other hand, the yellow portion corresponds to an intermediate range. Similarly, the effect of temperature and heating rate on yield of biochar can be predicted from the plots shown in Figs. 4.36(c) and (d). Both the surface and contour plots showed that with increase in temperature and heating rate reduces the corresponding yield of biochar. Figs. 4.36(e) and (f) show the surface and contour plot of gaseous product yield which was completely depends on pyrolysis temperature. Heating rate has no major influences on the gaseous product yield. In this way the response surface model

helps to gather information over a wide range of experimental conditions by using a small number of experimental runs.

4-2.4.2. Optimization of S. dimorphus biooil yield

In order to achieve an optimum biooil yield condition RSM simulation was carried out based on the effect of temperature and heating rate. Selected parameters (temperature and heating rate) were being evaluated at four different points. Each point was explored to select the condition that can produce the largest volume biooil with the highest desirability value (equal to 1). Thus, present study aims to investigate the optimum condition by setting the temperature at target of 500 ºC with maximum value of heating rate (40 ºC/min). A solution with desirability one was given by the statistical software based on the preceding conditions (shown in Fig. 4.37). Maximum yield of biooil yield obtained at optimum condition was found to be 38.2 wt.%, whereas biochar 25.2 wt.% and gaseous product of 21 wt.%.

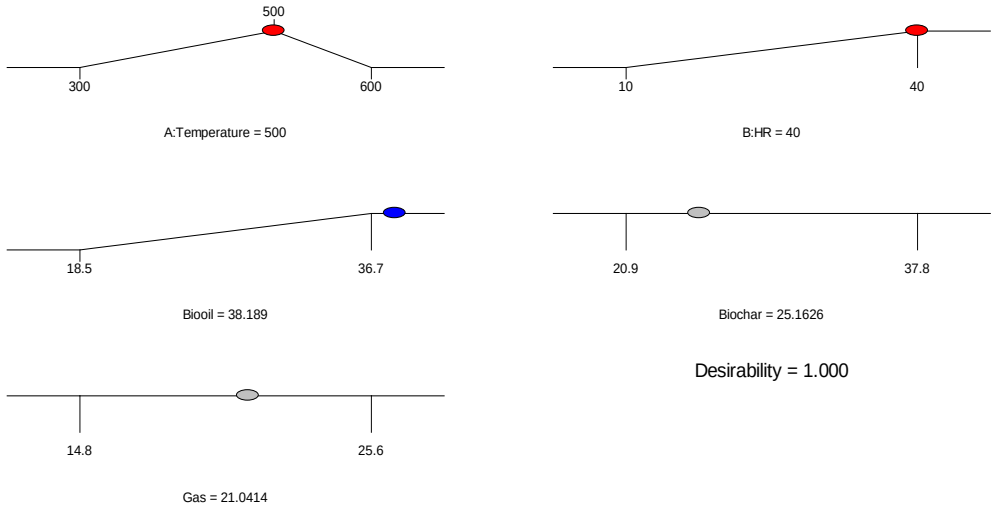

Fig. 4.37: Optimum conditions for highest yield of liquid product from pyrolysis of *S. dimorphus*

4-2.5. Pyrolysis of *S. dimorphus*

4-2.5.1. Sample pyrolysis runs

RSM analysis revealed that maximum yield of biooil was obtained at higher temperature with high heating rate. Therefore, pyrolysis experiments were carried out in fixed bed reactor for 0.22 mm of particle size at temperature range of 300–600 ºC

with a constant heating rate of 40 ºC/min. Nitrogen gas was passed through the reactor at 100 ml/min of flow rate. Pyrolysis temperature is the most important parameter that affects the product yields. The basic role of temperature is to provide necessary heat of decomposition to breakdown the biomass linkages [19]. The effect of pyrolysis temperature on product yields derived from pyrolysis of *S. dimorphus* in a fixed-bed reactor unit is illustrated in Fig. 4.38 and values are shown in Table 4.29.

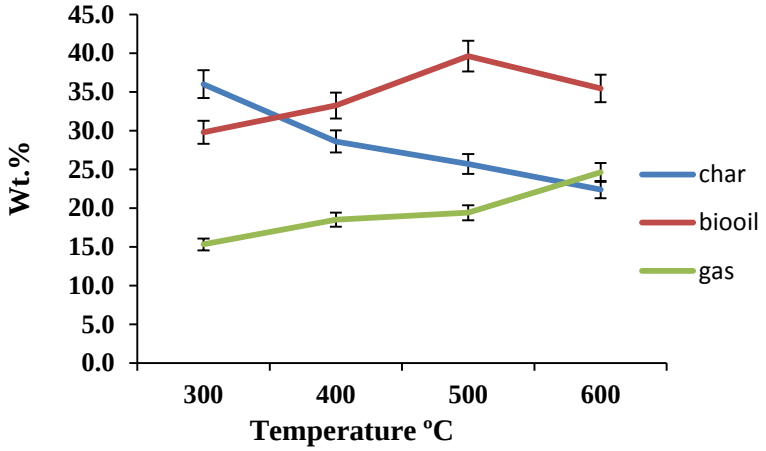

Fig. 4.38: Pyrolysis product yield of *S. dimorphus* at different temperatures

Table 4.29: Pyrolysis product distribution of *S. dimorphus* at different temperatures

Temperature (ºC)	Biooil (wt.%)	Biochar (wt.%)	Gas (wt.%)
300	29.8±0.09	36.0±0.45	15.3±0.44
400	33.2±0.07	28.6±0.45	18.5±0.35
500	39.6±0.56	25.7±0.51	19.4±0.66
600	35.4±0.59	22.4±0.62	24.6±0.26

Fig. 4.38 shows the plot between the yield percentage of pyrolysis products viz. biooil, biochar and gas at different temperatures. *S. dimorphus* was pyrolyzed with an increment of temperature 40 ºC/min to attain the desired final temperatures ranging from 300–600 ºC. It can be observed from both the Table 4.29 and Fig. 4.38 that biooil yield increases as temperature increases from 300–500 ºC and then starts to decrease with further increase of temperature to 600 ºC. Maximum biooil yield (39.6 wt.%) was obtained at 500 ºC. At higher temperatures, secondary reactions of volatiles led to a significant lower biooil yield. The yield of biochar reduced from 36.0 wt.% to 22.4 wt.% with increase in the pyrolysis temperature from 300 to 600 ºC. The decrease in the char yield with increasing temperature could be either due to

primary decomposition of the biomass at higher temperatures or through secondary decomposition of the char residue in the form of dehydrogenation and dehydration of reaction of hydroxyl groups. The higher char yield was observed in case of microalgae biomass as compared to terrestrial biomass which may be due to the presence of higher alkali content in the biomass. It is known that alkali and alkali earth metals serve as catalysts for char formation. With increase in temperature from 300 to 600 ºC the gaseous product yield also increased. The gas yield obtained was found to be maximum (24.6 wt.%) at 600 ºC and minimum (15.3 wt.%) at 300 ºC. The increase in gaseous products was thought to be predominantly due to secondary cracking of the pyrolysis vapors at higher temperatures. However, the secondary decomposition of the char at higher temperatures might give non-condensable gaseous products, which could contribute to the increase in gas yield [20]. As reported by many researchers that pyrolysis of biomass produces a gas rich in carbon oxides due to the high oxygen content present in the starting material [21, 22]. In case of algal biomass the origin ofthe CO_2 is mainly dependent on decomposition of carboxy groups in protein and carbohydrates [23].

4-2.5.2. Yield of chromatographic fractions

Maximum yield of biooil obtained at temperature 500 ºC is further separated by using liquid column chromatography with solvents of various polarities. Solvents were added into the column in an increasing order of polarity. First, the n-hexane, a common nonpolar solvent was passed through the biooil to eluated non polar substances. Ionic compounds present in the biooil were not dissolved in hexane hence unable to extract. Next an aromatic solvent toluene was used to eluated the dissolved compounds. Then the polar compounds are extracted from biooil using a polar solvent ethyl acetate and finally the use of methanol removed all the residues present in the biooil. All the sub-fractions obtained from microalgae biooil were shown in Fig. 4.39 on basis of weight percentage. It could be observed from the Fig. 4.39 that the microalgae biooil contained 18 wt.% of n-hexane fractions which might be useful for the production of hydrocarbons. Yields of toluene and ethyl acetate fractions were found to be 30 wt.% and 28 wt.% respectively. Methanol extraction of

the biooil yielded polar compounds which of about 24 wt.%. Yield of toluene ethyl acetate fractions were found to be more than that of other two fractions.

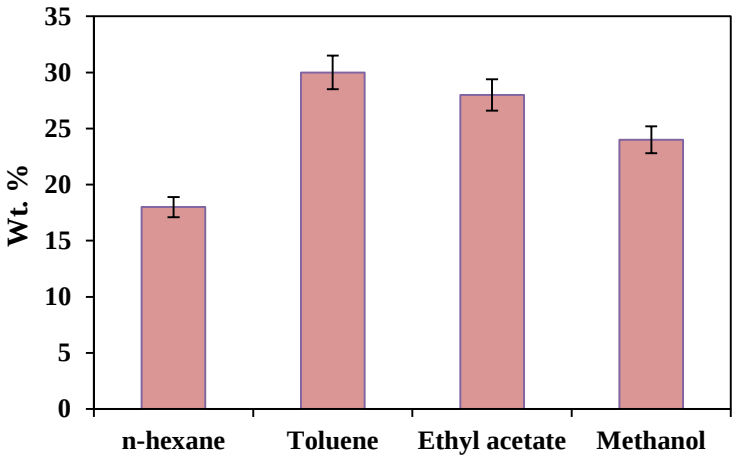

Fig. 4.39: Yield percentage of sub-fractions from *S. dimorphus* biooil

4-2.6. Characterization of the liquid product

4-2.6.1. Physical properties of liquid product

Various physicochemical properties of biooil obtained from the pyrolysis of *S. dimorphus* were carried out and are shown in Table 4.30 below with a comparison with other transportation fuels.

Table 4.30: Physicochemical properties of biooil obtained from *S. dimorphus* at 500 ºC with 40 ºC/min heating rate and their comparison with petro fuels

Properties	Method	Biooil	Gasoline	Diesel
Appearance		Dark Brownish		
Density, 15 ºC (g/cm^3)	ASTM D1298-99	0.8418	0.7197	0.8400
Specific gravity at 15ºC/15ºC	ASTM D1298-99	0.8425	0.72–0.78	0.82–0.85
p ^{H}		5	~7	3.6-5.6
Pour point (ºC)	ASTM D5853-09	+3	–40	–40 to –1
Cloud point (ºC)	ASTM D1310-01(2007)	10		
Flash point (ºC)	ASTM D6450-05(2010)	40	–43	53–80
Fire point (ºC)	ASTM D1310-01(2007)	57	-	-
C (wt.%)	-	74.73	-	-
H (wt.%)	-	10.60	-	-
N (wt.%)	-	5.79	-	-
S (wt.%)	-	0.61	-	-
O (wt.%)	-	8.27	-	-
H/C	-	1.49	-	-
O/C	-	0.08	-	-
Calorific value (MJ/kg)	-	28.52	42–46	42–45

It can be observed from the Table 4.30 that the biooil obtained from the *S. dimorphus* was dark brown in color. Density and gravity of biooil was found to be equivalent with diesel oil but seemed to be higher than gasoline fuel which may affect pumping and injection of fuel in the engine at lower temperatures. It can be further modified by blending with commercial transportation fuels. The flash point of the biooil showed nearby value with other fuels but pour point of plus 3 ºC may not cause freezing problems in colder regions with sub-zero climates.

Elemental analysis of the biooil obtained from the pyrolysis of *S. dimorphus* showed that carbon and hydrogen fractions increased while oxygen fractions decreased as compared to the raw biomass. The reduction of oxygen content in biooil might be ascribed to the de-oxygenation reactions taking place during the pyrolysis of biomass which was then being released in the form of CO and CO_2 [24]. However, the nitrogen content in microalgae biooil was still found to be higher than that of biooil derived from lignocellulosic biomass. N-containing compounds in biooil were assumed to be derived from protein degradation present in *S. dimorphus* [25]. Nitrogen present in fuel directly forms NO_x compounds which are not recommended from environmental and legislative point of view. Therefore, along with the oxygen,

removal of nitrogen from biooil is also necessary for their application in transportation sector. Recently, decarboxylation for removal of oxygen atoms in the form of carbon dioxide and catalytic hydrodenitrogenation (HDN) for removal of nitrogen are introduced to upgrade the pyrolysis oil from microalgae [19]. The H/C and O/C molar ratio of the biooil were found to be 1.49 and 0.08 respectively. The calorific value of the biooil was found to be 28.52 MJ/kg while the original biomass had calorific value of 19.0 MJ/kg. The heating value of biooil depends mainly on oxygen content and the operating conditions of the pyrolysis process such as type of reactor, heating rate and reaction temperature [26].

4-2.6.2. Chemical composition of biooil using FTIR spectra

FTIR spectra of sub-fractions obtained from the microalgae biooil are shown in Fig. 4.40.

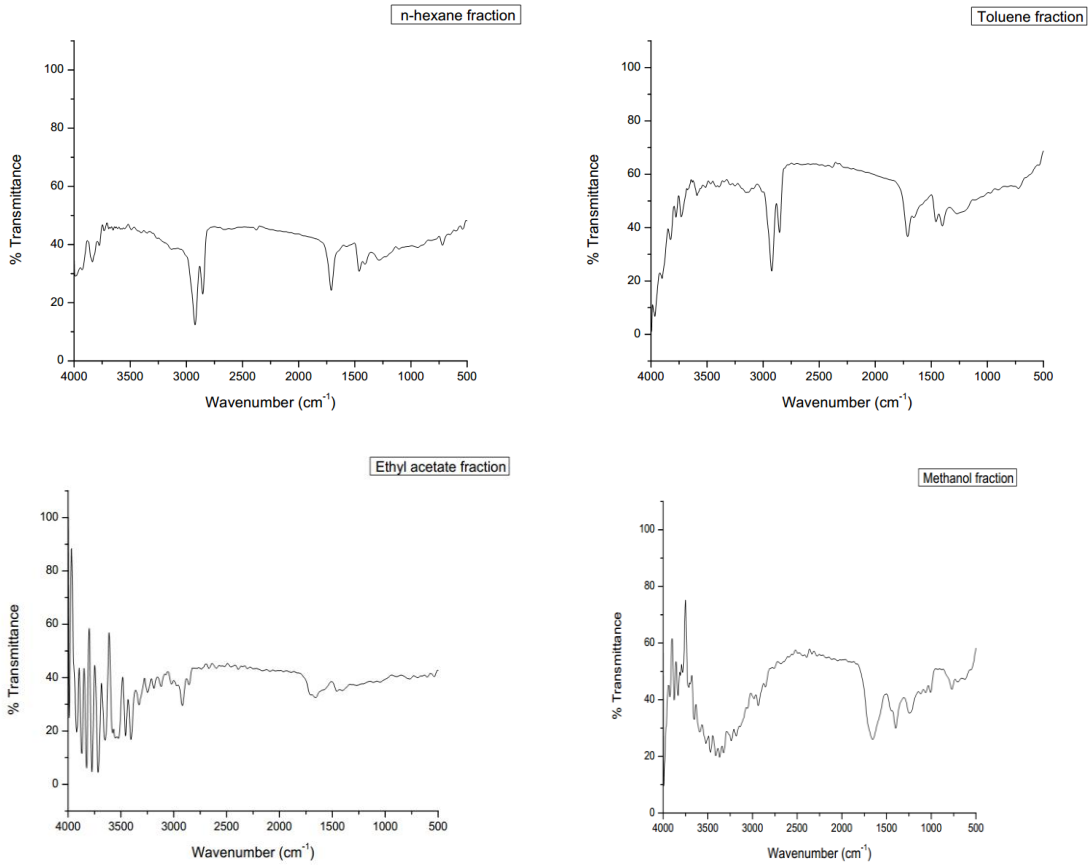

Fig. 4.40: FTIR images of sub-fractions obtained from *S. dimorphus* biooil after eluation of using solvents (a) n-hexane, (b) toluene, (c) ethyl-acetate, and (d) methanol

FTIR spectra can give insights into functional groups present in the biooil in a qualitative measure. The presence of absorption peak around 3200–3550 cm^{-1} indicated the presence of oxygenated compounds along with moisture. This peak was observed in methanol fraction extracted from microalgae biooil. But a sharp peak at 3580–3650 cm^{-1} indicated the presence of free O–H group which was observed in the ethyl acetate fraction of biooil. On the other hand, this band was absent in the toluene and hexane fractions of biooil meant both the fractions were free from O–H group. Absence of O–H group in hexane and toluene fractions supports the fact that fractionation separates the oxygenated compounds from biooils and thus increases the aliphatic nature of the biooil [39]. Peak at 2850 and 2925 cm^{-1} indicated the C–H stretching vibrations of CH_3 and CH_2 groups respectively. Further, the C–H deformation vibrations appeared between 1410 and 1515cm^{-1} indicated the presence of alkanes. The presence of amines was detected by C–N stretching vibrations between 1080 and 1335 cm^{-1}, which was observed in the methanol fraction of biooil. Vibrations between 1650 and 1750 cm^{-1} represented the C=O stretching which was compatible with the presence of ketone, quinine and aldehyde groups etc. The absorbance of peaks between 1575 and 1675 cm^{-1} representing C=C stretching vibrations was an indicative of alkenes and aromatics. The region between 1210 and 1320 cm^{-1} in methanol sub-fractions of biooil showed medium C–O stretching vibrations for carboxylic acids and their derivatives. The region between 700 to 900 cm^{-1} contained various bands related to aromatic out of plane C–H bending frequency. The high intensity of the above mentioned bands in toluene sub-fraction indicated that the aromatic hydrogen was located in aromatic rings with high degree of substitution.

4-2.6.3. ^{1}H NMR analysis of Biooil

The proton NMR spectra were applied to four different sub-fractions of biooil and the integral values of selected regions of the spectra on a percentage basis are presented in Table 4.31. Corresponding spectra are provided in appendix section.

Table 4.31: Percentage of hydrogen based on ^{1}H NMR analysis of microalgae biooil sub-fractions.

Proton assignment	Chemical Shift (ppm)	n-Hexane	Toluene	Ethyl acetate	Methanol
Aromatics	6.5–9.0	3.25	15.43	12.54	12.98
Phenolic OH or olefinic proton	5.0–6.5	3.90	5.43	6.88	3.89
Ring-join methylene (Ar–CH_2–Ar)	3.3–4.5	0.45	1.17	3.83	8.90
CH_3, CH_2, CH α to an aromatic ring	2.0–3.3	11.89	11.79	16.50	29.27
CH_2, CH_β to an aromatic ring (naphthenic)	1.6–2.0	6.75	6.90	7.00	6.94
β-CH_3, CH_2, and CH_γ or further from an aromatic ring	1.0–1.6	60.82	46.69	39.55	20.95
$CH_{3\gamma}$or further from an aromatic ring	0.5–1.0	10.67	8.86	9.71	6.05

It is evident from the Table 4.31 that, the most up-field region of the spectra from 0.5 to 1.6 ppm, represented the aliphatic protons that were attached to carbon atoms, at least two bonds, removed from a C=C double bond or heteroatom (O or N). This region was shown to be more populated for n-hexane fraction of microalgae biooil (~72%) than other fractions. This indicated the presence of higher aliphatic content in n-hexane fractions of the biooil. The aliphatic proton percentages in toluene, ethyl acetate and methanol were lower than hexane fractions (~55%, ~49% and ~27% for toluene, ethyl-acetate and methanol fractions respectively).

The next integrated region was from 1.6 to 3.3 ppm. This region represents the protons on aliphatic carbon atoms which may be bonded to a C=C double bond (aromatic or olefinic) or are two bonds away from a heteroatom. Lower amount of proton percentage were observed in this region for hexane and toluene fractions than that of other fractions. Methanol fraction showed highest percentage of proton for this integral region (~36%).

The next portion of ^{1}H NMR spectrum is from 3.3 to 4.5 ppm. This region represents the protons on carbon atoms next to an aliphatic alcohol or ether, or a methylene group (–CH_2) that joined two aromatic rings. Highest percentage of protons was observed in methanol fraction (8.9%) and that of lowest percentage was in hexane fraction (0.45%) of biooil.

The region between 5.0 and 6.5 ppm represents the presence of phenolic OH or olefinic protons. In this region low proton percentage was observed for n-hexane and methanol fractions while it was the highest for ethyl-acetate fraction of biooil. This may be due to the fact that fractionation with non-polar solvent separated the oxygenated compounds from the biooil. Low percentage of phenolic proton in the n-hexane fraction suggests its aliphatic nature. Phenolic derivatives present in ethyl-acetate fraction can be further used for flavorings agents in the food industry.

The region between 6.5 to 9.0 ppm was assigned to represent the aromatic protons. This represented not only those hydrogen atoms in benzenoids, but also those in hetero-aromatics containing O and N. For n-hexane fraction, the proton percentage (~3%) in this region was quite lower than other fractions whereas the toluene contained the highest percentage of protons (~15%). The ethyl acetate and methanol fractions showed almost equivalent amounts of proton percentage in this region. This confirmed that ethyl-acetate and methanol eluated mostly aromatic compounds including monocyclic and polycyclic aromatic hydrocarbons, phenolic and neutral oxygenated compounds respectively from the biooil.

Lastly, methanol was applied to the column which extracted the polar residues from the biooil. The region from 7.0 to 8.0 ppm was assigned for the amide molecules. Amines, esters, aldehyde, cyanide and nitro groups substituted molecules were observed in the region of 0.5–4.5 ppm. It was obvious from ^{1}H NMR spectra that aliphatic compounds present in the n-hexane fractions of biooil were relatively higher than other fractions. The absence of oxygen content in this fraction was also observed in the FTIR spectra. This was also supported by the higher calorific value (33.42 MJ/kg) of n-hexane fraction which was higher than that of the raw biooil (28.52 MJ/kg) obtained from *S. dimorphus*. Thus, fractionation reduced the disadvantages associated with the biooil that were highly oxygenated and further separates the phenolic and aromatic compounds which could be helpful for various industrial applications.

4-2.6.4. GC-MS analysis of Biooil

GC-MS analysis was carried out to identify the organic compounds present in the un-fractionated biooil and their corresponding fractions. Total ion chromatogram (TIC) of the raw biooil and n-hexane fraction obtained from microalgae is shown in Figs. 4.41 and 4.42 respectively. TIC of other sub-fraction will be provided in Appedix section.

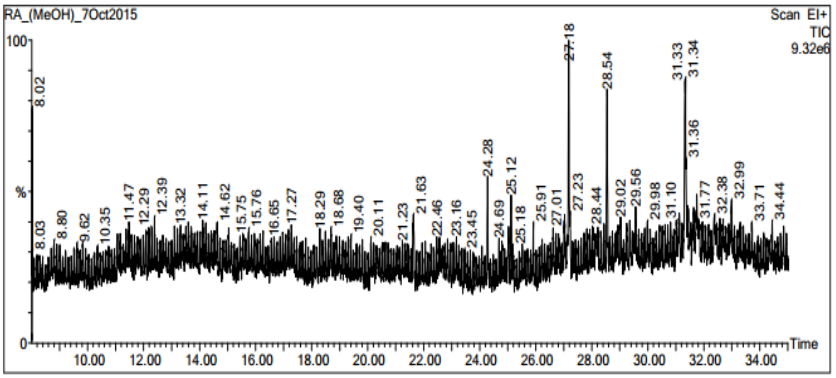

Fig. 4.41: TIC of microalgae biooil

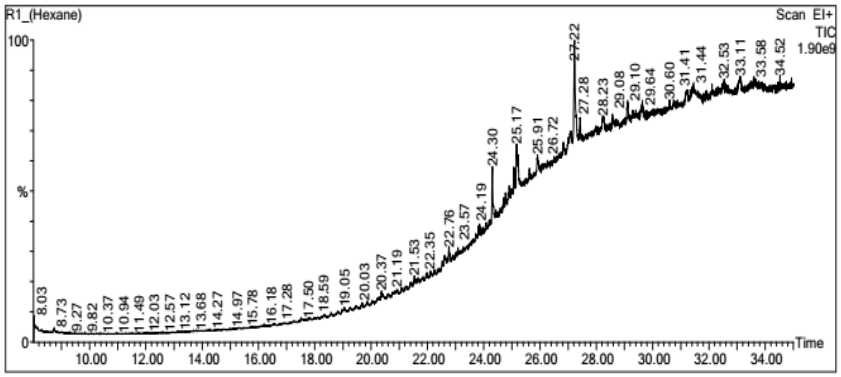

Fig. 4.42: TIC of n-hexane fraction of microalgae biooil

The compounds present in the biooils can be identified by comparing the chromatograms with standard chromatographic data available from NIST 98 spectrum library. Library search indicates that the biooil was a mixture of complex compounds for which a perfect separation of all the compounds was not possible. Fractionation of biooil using solvents of different polarity was able to separate some of the compounds which are listed Table 4.32 along with the retention time.

Table 4.32: Retention time (in min) and compound name present in microalgae biooil and its corresponding fractions obtained from GC-MS analysis

Raw algae biooil				n-hexane	
RT (min)	**C. Name**	**Area%**	**RT (min)**	**C. Name**	**Area%**
8.12	2-Methyl-1H-pyrrole	0.8	22.59		1.0
12.21	2,3-Dimethyl-1H-pyrrole	0.5	24.30	Bicyclo[3.1.1]Heptane, 2,6,6-TrimethyL	2.6
13.45	Phenol	0.6	25.06	n-Dotriacontane	1.6
17.72	N-Methylaniline	0.5	25.17	n-Tritriacontane	2.0
19.68	4-Methylphenol	0.5	25.21	n-Pentatriacontane	1.8
20.77	Benzyl nitrile	0.5	25.90	n-Tetracontane	1.0
24.73	Trans,Trans-1,6-Dimethylspiro[4.5]Decane	0.5	27.09	Octadecane	2.0
27.18	6-Nitroundec-5-Ene	0.4	27.22	n-henicosane	8.0
29.93	Hexadecanamide	0.4	27.43	Cyclohexane, 1,1'-(2-Ethyl-1,3-Propanediyl)Bis	1.5
30.43	Heptanamide, 4-Ethyl-5-Methyl	0.5	29.10		1.4
32.31	Hexamethylene Diacrylate	0.4	31.44		3.4

It can be observed from the Table 4.32 that, most of the compounds present in biooil were aromatic and phenolic in nature. Aromatic hydrocarbons, heterocyclic, amide, indole, alkane and nitrile compounds were present in the biooil. Presence of acids in biooil shows adverse effect due to its corrosive nature. Similarly, oxygenated compounds such as carbonyl groups affect the stability and heating value of biooil. Therefore, these compounds must be isolated from biooil structure through efficient separation techniques so as to utilize the biooil effectively. Alkane groups were found to be dominant in n-hexane fraction of biooil. Among the identified compounds n-alkanes, alkenes and branched hydrocarbons (isoprenoids) were most abundant. The majority of straight chain alkanes were distributed in the range from C_9 to C_{22}. However, some part of the light hydrocarbons may have escaped through evaporation along with the solvent after fractionation. Though alkenes were present in n-hexane fractions, n-alkanes were found to be dominant. GC-MS results for biooils are also supported by FTIR and ^{1}H NMR analyses. These results show consistency with the findings of Horne and Williams [20].

The properties of biooil produced from microalgae depend on its biochemical composition viz. lipids, proteins and carbohydrates. The major constituents of biooil

comprise of phenol and its alkylated derivatives, heterocyclic N-containing compounds, long chain fatty acids, alkanes and alkenes. Among these compounds, hydrocarbons are major components of biooil in order to replace the transportation fossil fuel. Fractionation helped to separate the hydrocarbons from other compounds (oxygenated, N-containing compounds etc) which in turn increase the stability of the biooil. Furthermore, aromatic hydrocarbons serve as important industrial chemicals and transportation fuel additives to increase octane number. Proteins produce large amounts of N-containing heterocycles, pyrroles and indoles, carbohydrates produce cyclic ketones as well as phenols while lipids in microalgae being cracked into hydrocarbons during pyrolysis as well as fatty acids [40]. Presence of amides and nitriles groups in biooil was possibly due to reaction between ammonia (protein decomposition product) and fatty acids (lipid degradation products) during thermal degradation of *S. dimorphus* [27]. Similarly, the phenolic components detected in the biooil may arise from thermal degradation of carbohydrates [28] and pyrolysis of some amino acids [29]. Pyrroles may be products of the pyrolysis of melanoidin like-polymers that are formed by reaction between sugars and amino acids present in microalgae [30]. The generation of PAHs, such as naphthalenes, may have been due to some complex reactions, e.g. cyclization or condensation reactions [31].

4-2.7. Characterization of biochar

4-2.7.1. Physico-chemical properties of biochar

The proximate and ultimate analysis of microalgae biochar obtained at different temperatures with heating rate 40 ºC/min are shown in Table 4.33.

Table 4.33: Properties of biochars obtained at different temperatures from pyrolysis *S. dimorphus*

Properties	Biochar			
	300 ºC	400 ºC	500 ºC	600 ºC
pH	7.18±0.07	7.93±0.17	7.96±0.22	8.32±0.02
EC (m mho cm^{-1})	0.14±0.03	0.15±0.03	0.24±0.03	0.46±0.04
Moisture Content (wt.%)	0.08±0.003	0.07±0.007	0.06±0.004	0.05±0.005
Ash Content (wt.%)	39.60±0.26	41.43±0.95	43.30±0.36	44.17±0.42
Volatile Content (wt.%)	17±0.26	6.63±0.29	4.33±0.60	3.33±0.25
Fixed C (wt.%)	43.40±0.82	51.87±0.64	52.37±0.70	52.17±0.68
C (wt.%)	46.82	47.37	50.20	53.58
H (wt.%)	7.85	7.93	8.01	8.50
N (wt.%)	5.85	5.63	6.01	6.50
O (wt.%)	39.48	39.07	35.78	31.42
H/C	2.01	2.01	1.91	1.90
O/C	0.63	0.62	0.53	0.44

It can be observed from the Table 4.33 that pH and electrical conductivity (EC) values of biochar gradually increased with increase in temperature from 300-600 ºC which might be due to the separation of alkali salts from organic materials. The biochars produced at higher temperatures, had higher pH values is in agreement with other studies [32-33]. The increased alkalinity of biochars might be due to the loss of organic functional groups (such as –COOH and –OH) present on the biochar surface at high temperatures [34]. On addition of biochar to soil shows a significant difference in pH compared to the pure soil. Biochar may be used as a liming agent as it is capable to resolve the acidity problem of soil. The accumulation of cations (K, Na, Ca and Mg) and the formation of carbonates, such as $CaCO_3$ and $MgCO_3$ are responsible for the liming capacity of biochar. The organic anions of the biochar will rapidly react with H^+ in the soil, while the carbonates will react slower with the H^+, thus, the reduction of soil acidity will last longer [32]. EC can be used as an index for ionic strength and is an estimate for the amount of dissolved salts in the solution [35]. Biochars produced at higher temperatures had higher EC which might be due to

presence of higher soluble salts in biochars caused by the loss of volatile materials [36–37]. Biochar with higher EC when applied to soil may harm plant growth by reducing water uptake and cause nutrient imbalance due to increased salinity [38]. Therefore, EC of biochar is an important parameter which must be taken into consideration prior to biochar application in soil as a soil amendment. Though biochar with high pH may be desirable for recovery of highly acidic soils, but, may also harm the soil due to its high EC. Therefore, the final pyrolysis temperature is important for favorable values of pH and EC of biochar for its use as a soil amendment.

Moisture content of biochars found to be decrease with increase in temperatures. The ash content of biochar increases form 39 wt.% to 44 wt.% with rise in pyrolysis temperature from 300–600 ºC. This increase in ash content was caused by the increase in relative concentration of Ca, Mg, K, P, S and Zn at higher temperature [39]. The major difference among the biochar obtained at different pyrolysis temperatures in this study were in their ash content, which is comparatively higher in amount than the biochar produced from lignocellulosic biomasses. This might be due to the presence of exogenous material (sand) that could not be removed from the raw algal biomass [40]. As the final treatment temperature of biochar increased from 300–600 ºC volatile matter decreased and fixed carbon content increased which signified the biochar as high-quality solid fuel [41]. Unlike lignocellulosic biochar, algal biochar may contain lesser oxygen and carbon than the raw biomass. With the increase in temperature, H/C and O/C ratios of biochar decreased which was probably due to dehydration, decarboxylation and decarbonylation reactions. The oxygen containing functionalities were decomposed by decarbonylation and decarboxylation reactions followed by increase in proportion of aryl C and carbonization of biochar [39]. The decrease in H/C and O/C ratios of biochars with increase in pyrolysis temperature from 300 to 600 ºC for *S. dimorphus,* can be also portrayed by using the Van-kravelen diagram shown in Fig. 4.43 below.

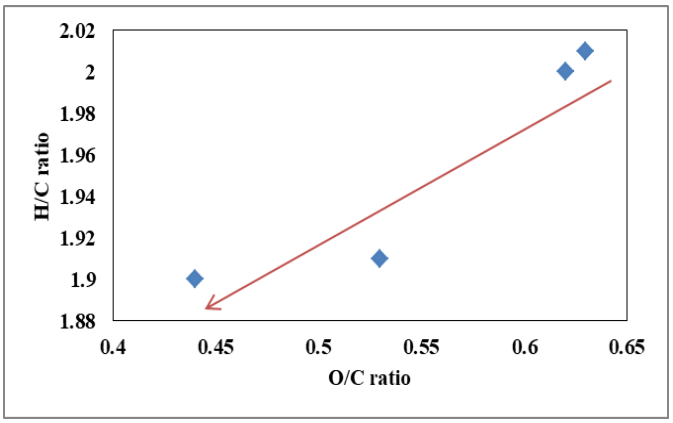

Fig. 4.43: Van-kravelen diagram of biochars obtained from *S. dimorphus*

4-2.7.2. SEM analysis of biochar

Scanning Electron Microscopy (SEM) images of biochar produced at 300, 400 and 500 ºC with heating rate of 40 ºC/min are shown in Fig. 4.44. Surface morphology of the biochar was studied at high magnification imaging by using SEM analysis. It is a very widely used technique which confirmed the heterogeneous distribution of pores and presence of rough texture on sample surface.

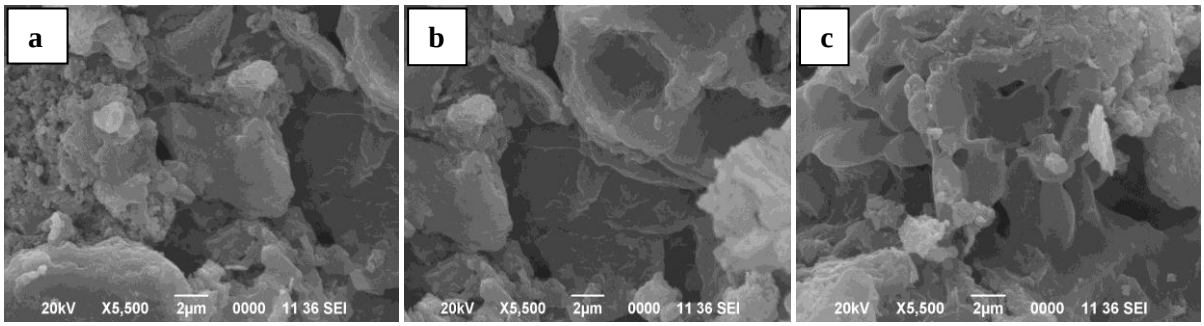

Fig. 4.44: SEM images of biochars produced at (a) 300 ºC, (b) 400 ºC, and (c) 500 ºC

It can be observed from the Fig. 4.44 that biochar produced at temperature 300 ºC had rough and irregular surface texture. Biochar produced at 400 ºC, showed some caves like image of the surface. As the temperature rises to 500 ºC, biochar surfaces developed some pores like structure due to release of volatiles from the biomass during thermal treatment. Some bright spots were also observed on the

surface of biochar produced at higher temperature which occurs might be due to the presence of silica particles in the biochar [40].

4-2.7.3. EDX analysis of biochar

EDX analysis of the biochar produced at 500 ºC was carried out and the chromatograph is shown in Fig. 4.45. The elements present on the surface of the biochar at that temperature are listed in a table. It can be observed from the Table 4.34 that carbon is the major element present in the biochar. After that silica is highly available on the biochar surface followed by Fe, Ca, Mg, K, Na, P, and S. Occurrence of silica on the biochar surface is due to the presence of some exogenous material (sand) in *S. dimorphus* biomass. This might be the reason of high ash content in algal biochars produced at different temperatures. Detection of high percentage of carbon in EDX analysis supports the formation of carbonized material from the biomass at higher pyrolysis temperature.

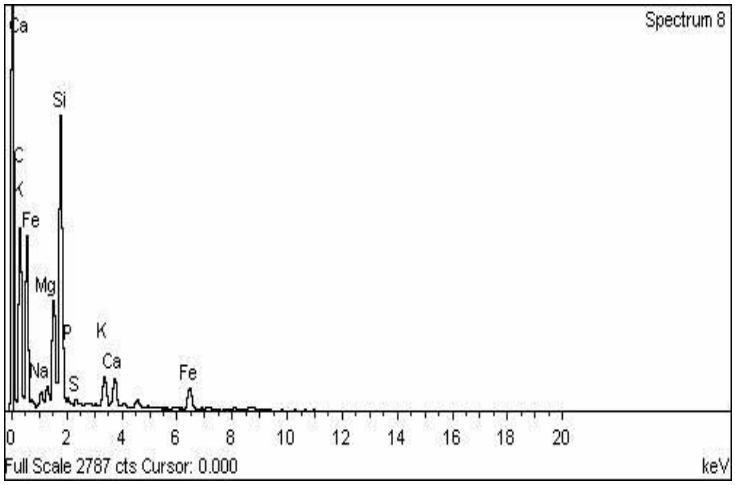

Table 4.34: Elemental composition of *S. dimorphus* biochar from EDX analysis

Element	Weight%	Atomic%
C	70.40	86.10
Na	0.92	0.59
Mg	1.47	0.89
Si	17.35	9.08
P	0.63	0.30
S	0.42	0.19
K	2.30	0.86
Ca	2.67	0.98
Fe	3.83	1.01
Total	100.00	

Fig. 4.45: EDX spectrum of biochar produced at 500 º C from *S. dimorphus*

4-2.7.4. FTIR analysis of biochar

FTIR spectra of biochar samples produced at different temperature (300, 400, 500 and 600 ºC) are shown in Fig. 4.46.

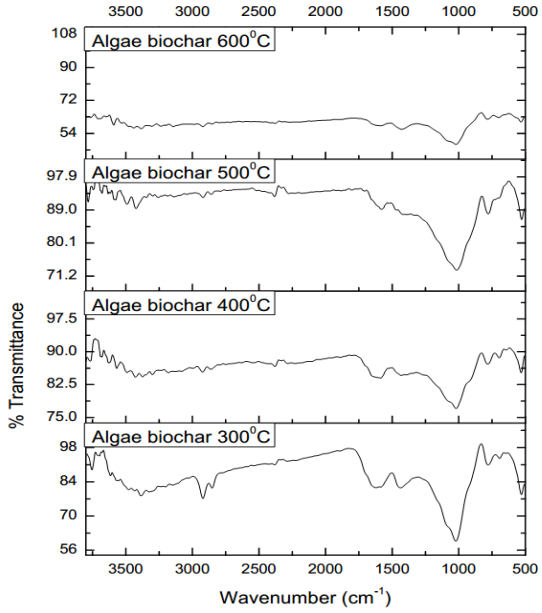

Fig. 4.46: FTIR spectra of *S. dimorphus* biochar produced at different temperatures

The Fig. 4.46 showed the changes occurred in case of functional groups present in the biochar. As the pyrolysis temperature increased to 600 ºC, the characteristic peaks tend to disappear. The bands corresponding to O–H stretches (at wave numbers of 3358–3403 cm^{-1}, broad), aromatic rings at 1657 cm^{-1}, aromatic out of plane C–H bending (various bands between 900 and 700 cm^{-1}) and C=O (1550–1653 cm^{-1}) were identified. Weak absorption bands at 2950 and 2850 cm^{-1}were observed that were assigned to aliphatic C–H stretching decreased with increase in temperature. The spectrum of the biochar obtained at 600 ºC showed the disappearance of most of the bands and suggested that the biochar was mainly an aromatic carbon polymer. The absorption peaks at 780 and 1400 cm^{-1} in the spectra of biochar produced at 300 ºC were assigned to the carboxylate (–COO) group [42]. Increase of terminal pyrolysis temperature signified the loss of carboxylate (–COO) group from biochar. Thus a gradual decrease in intensity of the peaks was seen for the spectrum of biochars produced at 300 to 600 ºC. A very strong band at 1075 cm^{-1}

corresponds to Si–O stretching vibrations was observed due to silica frustules, a siliceous shells that surround the cells [40]. With increase in temperature towards 600 ºC, slight shifting of the band was observed to lower wave numbers (1057–1046 cm^{-1}). This could be assigned to the stretching vibrations of the Si–O–Si bridges in SiOx [43]. This interpretation shows consistency with the results of EDX analysis and point to a relatively high content of silica-based compounds present in *S. dimorphus* [43].

4-2.7.5. Carbon sequestration potential of biochar

One of the most crucial parameter of biochar is carbon sequestration potential (CSP). Higher CSP means higher resistance ability of biochar against both biotic and abiotic degradation. Based on R_{50} recalcitrance index which determines the accessing the stability of carbon in biochar sample CSP can be determined. The R_{50} index and CSP values for biochars produced at different temperatures are shown in Table 4.35.

Table 4.35: R_{50} index and CSP of *S. dimorphus* biochars at different temperatures

Temperature (ºC)	**R_{50} index**	**CSP%**
300	0.62	25.26
400	0.67	32.98
500	0.70	34.49
600	0.76	36.27

It was observed from the Table 4.35 that the recalcitrance of biochar increased from 0.62 to 0.76 with increase in pyrolysis temperature from 300–600 ºC. This might be attributed to increase in aromatic C and decrease in N in biochar with increment of temperature [44]. Thus, biochar produced at lower temperature had lower recalcitrance meant lower CSP, which indicated that it could be easily mineralized by microorganism compared to biochar produced at higher temperature with higher CSP.

4-2.7.6. XRD analysis of biochar

The XRD spectra of *S. dimorphus* biochars produced at 300, 500 and 600 ºC are shown in Fig. 4.47.

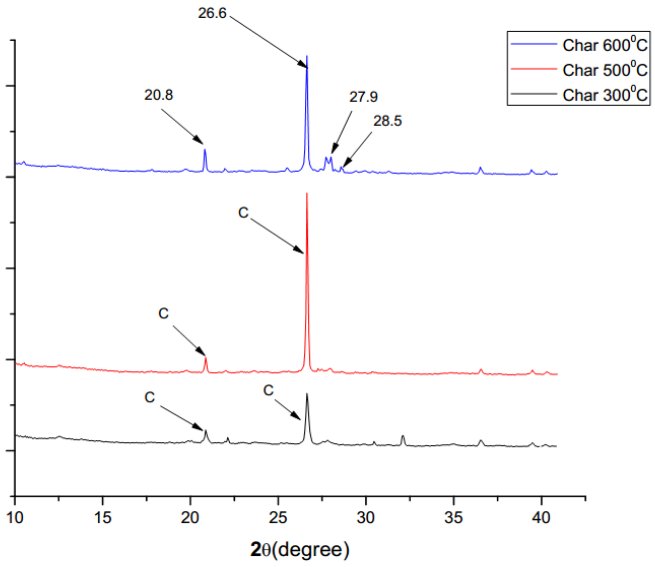

Fig. 4.47: XRD analysis of *S. dimorphus* biochar obtained at different temperatures

The XRD patterns of biochars revealed sharp peaks, which showed a high degree of crystallinity with characteristic peaks at 20.8º, 26.6º, 27.9º and 28.5º. The diffraction peaks at value of 2θ equal to 20.8º and 26.6º were considered as an evidence for the presence of carbon in the biochar sample. As the severity of the biochar production temperature increased the intensity of the corresponding peaks were also increased. At 500 ºC, highest intensity of carbon peak was observed as compared to other two temperatures indicates the formation carbonized material. At 300 and 600 ºC some other peaks were observed which indicated the presence of miscellaneous inorganic components. At temperature 600 ºC, peaks at 27.9º and 28.5º indicated the presence of silicate material in the biochar [45]. Biochar produced at higher temperature lead to the deposition of Si compound present in microalgae biomass in the form of sand like materials. This result showed consistency with the findings of FTIR and EDX analysis of biochar.

4-2.8. Summary

In the present investigation, microalgae species, *S. dimorphus* was being studied as a potential feedstock for thermo-chemical conversion. Physicochemical characterization of *S. dimorphus* was carried out which provided the information that biomass has high percentage of ash content (17.33 wt.%). Presence of high ash content in aquatic flora from natural ecosystems, including micro and macro algae was might be due to the presence of the inorganic component in the biomass. The biomass has the volatile matter (VM) of 51.45 wt.% and fixed carbon content (FC) of 31.13 wt.%. The carbon, hydrogen and nitrogen contents in the algal biomass were found to be 52.60 wt.%, 6.21 wt.% and 8.75 wt.% respectively obtained on dry basis. Further, with the help of a thermogravimetric analyzer degradation of the biomass was monitored.

Three main phases were observed during the thermochemical conversion of the aquatic species, based on which detailed kinetic studies have been carried out to estimate the various parameters using TG–DTG curves. Three model-free methods, Friedman, FWO and KAS analysis were applied to study the kinetic analysis when experimental data was represented as the set of measurements at three different heating rates. The model-free methods provide information on kinetic parameters, such as the activation energy (E_a) and frequency factor without determining a concrete kinetic model.

Further, a simulation technique Response Surface Methodology (RSM) was employed to microalgae species *S. dimorphus* in order to establish a model interrelated with two independent variables such as temperature and heating rate by using Central composite design (CCD) matrix against three dependent variables such as yield of biooil, biochar and gas yield. As suggested by RSM analysis, maximum yield of biooil was obtained at higher temperature with high heating rate. Therefore, pyrolysis *of S. dimorphus* was performed in fixed bed reactor for 0.22 mm of particle size at temperature range of 300–600 ºC with a constant heating rate of 40 ºC/min. Maximum yield of biooil (39.6 wt.%) was obtained at 500 ºC with calorific value of 28.52 MJ/kg. Further, the maximum yield of biooil obtained at temperature 500 ºC was separated by using liquid column chromatography with solvents of various

polarities so that different group of compounds can be separated from the biooil. Microalgae biooil and its sub-fractions were characterized by using different spectroscopic and chromatographic technique. ^{1}H NMR analysis showed that n-hexane fraction contained highest percentage of aliphatic protons. Similarly, toluene fraction had high percentage of aromatic protons and ethylacetate fraction contained highest percentage of phenolic protons. This result also showed consistency with the FTIR analysis of the sub-fractions. The compounds present in the biooils were further identified by comparing the chromatograms with NIST 98 spectrum library. Thus, fractionation of biooil may be useful in biooil upgradation and recovery of value added chemicals.

Biochar produced as co-product of pyrolysis at different temperature was also analyzed by using different techniques. Physicochemical characterization of biochar revealed that pH and electrical conductivity (EC) values of biochar gradually increased with increase in temperature from 300-600 ºC which might be due to the separation of alkali salts from organic materials. Though biochar with high pH may be desirable for recovery of highly acidic soils, but, may also harm the soil due to its high EC. Therefore, the final pyrolysis temperature is important for favorable values of pH and EC of biochar for its use as a soil amendment. It was also observed that biochar obtained at higher temperature was highly recalcitrant and could be used for C-sequestration and GHG mitigation.

References:

1. Schenk, P. M., Thomas-Hall, S. R., Stephens, E., Marx, U. C., Mussgnug, J. H., Posten, C., Kruse, O. and Hankamer, B. Second generation biofuels: high-efficiency microalgae for biodiesel production. *Bioenergy Research*, 1(1): 20-43, 2008.

2. Satyanarayana, K. G., Mariano, A. B. and Vargas, J. V. C. A review on microalgae, a versatile source for sustainable energy and materials. *International Journal of Energy Research*, 35(4): 291-311, 2011.

3. Ehimen, E. A., Sun, Z. F. and Carrington, C. G. Variables affecting the in situ transesterification of microalgae lipids. *Fuel*, 89(3): 677-684, 2010.

4. Du, Z., Hu, B., Ma, X., Cheng, Y., Liu, Y., Lin, X., Wan, Y., Lei, H., Chen, P. and Ruan, R. Catalytic pyrolysis of microalgae and their three major components: carbohydrates, proteins, and lipids. *Bioresource Technology*, 130: 777-782, 2013.

5. Mohan, D., Pittman, C. U. and Steele, P. H. Pyrolysis of wood/biomass for bio-oil: a critical review. *Energy and Fuels*, 20(3): 848-889, 2006.

6. Harman-Ware, A. E., Morgan, T., Wilson, M., Crocker, M., Zhang, J., Liu, K., Stork, J. and Debolt, S. Microalgae as a renewable fuel source: fast pyrolysis of Scenedesmus sp. *Renewable Energy*, 60: 625-632, 2013.

7. H. Okkou, M. Naddaf, A. Alinizam, M.F. Azmeh, Growth promotion of indigenous *Scenedesmus dimorphus* strain under different conditions using stirred tank photobioreactor. *International Journal of ChemTech Research*, 8 (11): 221-228, 2015.

8. Ross, A. B., Jones, J. M., Kubacki, M. L. and Bridgeman, T. Classification of macroalgae as fuel and its thermochemical behaviour. *Bioresource Technology*, 99(14): 6494-6504, 2008.

9. Shuping, Z., Yulong, W., Mingde, Y., Chun, L., and Junmao, T. Pyrolysis characteristics and kinetics of the marine microalgae Dunaliella tertiolecta using thermogravimetric analyzer. *Bioresource Technology*, 101(1): 359-365, 2010.

10. Hamidi, N., Yanuhar, U., and Wardana, I. N. G. Potential and properties of marine microalgae Nannochloropsis oculata as biomass fuel feedstock. *International Journal of Energy and Environmental Engineering*, 5(4): 279-290, 2014.

11. Sanchez-Silva, L., López-González, D., Villaseñor, J., Sánchez, P. and Valverde, J. L. Thermogravimetric–mass spectrometric analysis of lignocellulosic and marine biomass pyrolysis. *Bioresource Technology*, 109: 163-172, 2012.

12. Biller, P. and Ross, A. B. Potential yields and properties of oil from the hydrothermal liquefaction of microalgae with different biochemical content. *Bioresource Technology*, 102(1): 215-225, 2011.

13. Chaiwong, K., Kiatsiriroat, T., Vorayos, N. and Thararax, C. Study of bio-oil and bio-char production from algae by slow pyrolysis. *Biomass Bioenergy*, 56: 600-606, 2013.

14. Campanella, A., Muncrief, R., Harold, M. P., Griffith, D. C., Whitton, N. M. and Weber, R. S. Thermolysis of microalgae and duckweed in a CO_2-swept fixed-bed reactor: bio-oil yield and compositional effects. *Bioresource Technology*, 109: 154-162, 2012.

15. Muktham, R., Ball, A. S., Bhargava, S. K., & Bankupalli, S. Study of thermal behavior of deoiled karanja seed cake biomass: thermogravimetric analysis and pyrolysis kinetics. *Energy Science & Engineering*, 4(1); 86-95, 2016.

16. Peng, W., Wu, Q., Tu, P., and Zhao, N. Pyrolytic characteristics of microalgae as renewable energy source determined by thermogravimetric analysis. *Bioresource Technology*, 80(1): 1-7, 2001.

17. Agrawal, A. and Chakraborty, S. A kinetic study of pyrolysis and combustion of microalgae Chlorella vulgaris using thermo-gravimetric analysis. *Bioresource Technology*, 128: 72-80, 2013.

18. Li, D., Chen, L., Zhang, X., Ye, N., and Xing, F. Pyrolytic characteristics and kinetic studies of three kinds of red algae. *Biomass Bioenergy*, 35(5): 1765-1772, 2011.

19. Hu, Z., Zheng, Y., Yan, F., Xiao, B., and Liu, S. Bio-oil production through pyrolysis of blue-green algae blooms (BGAB): product distribution and bio-oil characterization. *Energy*, 52, 119-125, 2013.

20. Horne, P. A. and Williams, P. T. Influence of temperature on the products from the flash pyrolysis of biomass. *Fuel*, 75(9): 1051-1059, 1996.

21. Pan, P., Hu, C., Yang, W., Li, Y., Dong, L., Zhu, L., Tong, D., Qing, R. and Fan, Y. The direct pyrolysis and catalytic pyrolysis of Nannochloropsis sp. residue for renewable bio-oils. *Bioresource Technology*, 101(12): 4593-4599, 2010.

22. Grierson, S., Strezov, V., Ellem, G., Mcgregor, R. and Herbertson, J. Thermal characterisation of microalgae under slow pyrolysis conditions. *Journal of Analytical and Applied Pyrolysis*, 85(1): 118-123, 2009.

23. Yanik, J., Stahl, R., Troeger, N. and Sinag, A. Pyrolysis of algal biomass. *Journal of Analytical and Applied Pyrolysis*, 103: 134-141, 2013.

24. Yuan, X., Wang, J., Zeng, G., Huang, H., Pei, X., Li, H., Liu, Z. and Cong, M. Comparative studies of thermochemical liquefaction characteristics of microalgae using different organic solvents. *Energy*, 36(11): 6406-6412, 2011.

25. Maddi, B., Viamajala, S. and Varanasi, S. Comparative study of pyrolysis of algal biomass from natural lake blooms with lignocellulosic biomass. *Bioresource Technology*, 102(23): 11018-11026, 2011.

26. Duman, G., Okutucu, C., Ucar, S., Stahl, R. and Yanik, J. The slow and fast pyrolysis of cherry seed. *Bioresource Technology*, 102(2): 1869-1878, 2011.

27. Simoneit, B. R., Rushdi, A. I., Bin Abas, M. R., & Didyk, B. M. Alkyl amides and nitriles as novel tracers for biomass burning. *Environmental Science and Technology*, 37(1): 16-21, 2003.

28. Brown, T. M., Duan, P., and Savage, P. E. Hydrothermal liquefaction and gasification of *Nannochloropsis sp*. *Energy and Fuels*, 24(6): 3639-3646, 2010.

29. Torri, C., Garcia Alba, L., Samori, C., Fabbri, D. and Brilman, D. W. Hydrothermal treatment (HTT) of microalgae: detailed molecular characterization of HTT oil in view of HTT mechanism elucidation. *Energy and Fuels*, 26(1): 658-671, 2012.

30. Tressl, R., Wondrak, G. T., Krüger, R. P. and Rewicki, D. New melanoidin-like Maillard polymers from 2-deoxypentoses. *Journal of Agricultural and Food Chemistry*, 46(1): 104-110, 1998.

31. Subagyono, R. D. J., Qi, Y., Jackson, W. R., and Chaffee, A. L. Pyrolysis-GC/MS analysis of biomass and the bio-oils produced from CO/H 2 O reactions. *Journal of Analytical and Applied Pyrolysis*, 120: 154-164, 2016.

32. Yuan, J. H., Xu, R. K. and Zhang, H. The forms of alkalis in the biochar produced from crop residues at different temperatures. *Bioresource Technology*, 102: 3488-3497, 2011.

33. Wu, W., Yang, M., Feng, Q., Mcgrouther, K., Wang, H., Lu, H. and Chen, Y. Chemical characterization of rice straw-derived biochar for soil amendment. *Biomass and Bioenergy*, 47: 268-276, 2012.

34. Zhang, J., Liu, J. and Liu, R. Effects of pyrolysis temperature and heating time on biochar obtained from the pyrolysis of straw and lignosulfonate. *Bioresource Technology*, 176: 288- 291, 2015.

35. Hossain, M. K., Strezov, V., Chan, K. Y., Ziolkowski, A. and Nelson, P. F. Influence of pyrolysis temperature on production and nutrient properties of wastewater sludge biochar. *Journal of Environmental Management*, 92: 223-228, 2011.

36. Chintala, R., Mollinedo, J., Schumacher, T. E., Malo, D. D. and Julson, J. L. Effect of biochar on chemical properties of acidic soil. *Archives of Agronomy and Soil Science*, 60: 393- 404, 2014.

37. Gai, X., Wang, H., Liu, J., Zhai, L., Liu, S., Ren, T., and Liu, H. Effects of feedstock and pyrolysis temperature on biochar adsorption of ammonium and nitrate. *PloS One*, 9(12): e113888, 2014.

38. Chutia, R. S., Kataki, R. and Bhaskar, T. Characterization of liquid and solid product from pyrolysis of *Pongamia glabra* deoiled cake. *Bioresource Technology*, 165: 336-342, 2014.

39. Mullen, C. A., Boateng, A. A., Goldberg, N. M., Lima, I. M., Laird, D. A. and Hicks, K. B. Bio-oil and bio-char production from corn cobs and stover by fast pyrolysis. *Biomass and Bioenergy*, 34(1): 67-74, 2010.

40. Bird, M. I., Wurster, C. M., de Paula Silva, P. H., Bass, A. M. and De Nys, R. Algal biochar–production and properties. *Bioresource Technology*, 102(2): 1886-1891, 2011.

41. Kiatsiriroat, T. Biochar production from freshwater algae by slow pyrolysis. *Maejo International Journal of Science and Technology*, 6(2): 186-195, 2012.

42. Pütün, A. E., Özbay, N., Önal, E. P. and Pütün, E. Fixed-bed pyrolysis of cotton stalk for liquid and solid products. *Fuel Processing Technology*, 86(11): 1207-1219, 2005.

43. Muradov, N., Fidalgo, B., Gujar, A. C., Garceau, N., and Ali, T. Production and characterization of Lemna minor bio-char and its catalytic application for biogas reforming. *Biomass and Bioenergy*, 42: 123-131, 2012.

44. Spokas, K. A., Koskinen, W. C., Baker, J. M. and Reicosky, D. C. Impacts of woodchip biochar additions on greenhouse gas production and sorption/degradation of two herbicides in a Minnesota soil. *Chemosphere*, 77(4): 574-581, 2009.

45. He, B. C., Fu, W. E., Wu, C. L., Chien, Y. S. Liou, H. C. Calibrating the Z-magnification of atomic force microscope below 10nm by single-atom steps. *Thin Solid Films*, 584: 372-377, 2015.

Chapter -4 (c)

4-3.1. Introduction

Biochar, a by-product from thermal treatment of biomass in a closed system with limited supply of oxygen is a stable carbon rich solid material [1]. In recent years, biochar has gained increasing attention for its potential beneficial application in the field of agricultural and environmental implication. Amongst its various applications, viz. carbon sequestration, soil conditioning [2], pollution remediation [3], and waste recycling [4], biochar also exhibited great potential for managing the waste stream originating from industrial effluents [5]. Most of the studies reported that biochar showed excellent ability to remove organic [6–8] and inorganic pollutants [9–11] from aqueous solution. The efficacy of biochar in contaminant management depends on its porous nature, abundant surface functional groups, surface area and ion-exchange capacity [3]. Compared with traditional activated carbon, biochar appears to be a potential low cost, environment friendly and effective adsorbent. The production of activated carbon requires higher temperature and additional activation process as compared to the biochar production, which is a cheap process with low energy requirements [12]. The cost of biochar production is mainly associated with the machinery and heating value, which is only about $4 per giga joule and is dependent on a supply of cheap biomass (various waste biomass) [13].

In the present context, biochars derived from the pyrolysis of seed covers of *P. glabra* and *M. ferrea* and microalgae species *S. dimorphus* are subjected to a study as a low cost adsorbent. Inorganic effluent removal efficiency by using biochar derived from the selected feedstocks is comprehensively discussed in part C and organic pollutant removal efficiency by using PGSC derived biochar is discussed in the part D of chapter 4.

4-3.2. Cobalt as heavy metal

Inorganic pollutants, mainly heavy metals create a risk to public health because of their high toxicity, non-biodegradability, and widespread occurrence in natural and human-altered environments [14]. Among the heavy metals, cobalt (Co) has been identified as one of the significant toxic element found in various industrial wastewater including petrochemical wastewater, cobalt bearing mineral mining and

smelting wastewater and nuclear wastewater. Co in trace level may cause harmful effects due to chronic exposure [15]. The permitted limits of Co in the livestock wastewater and irrigation water are 0.01 and 0.05 mg/L respectively, whereas the acceptable limit of Co in drinking water is 0.002 mg/L [16]. Acute exposure to Co can induce nausea, vomiting and neuro toxicological symptoms such as headaches and changes in reflexes, while chronic exposure to cobalt may cause partial or complete loss of smell, gastrointestinal troubles and dilation of the heart [17]. Therefore, removal of Co ions from water is of great concern for conservation of environment as well as human health.

4-3.3. Effect of contact time

The effect of contact time on removal of Co (II) by using biochars derived from PGSC, MFSC and *S. dimorphus* are shown in Fig. 4.48.

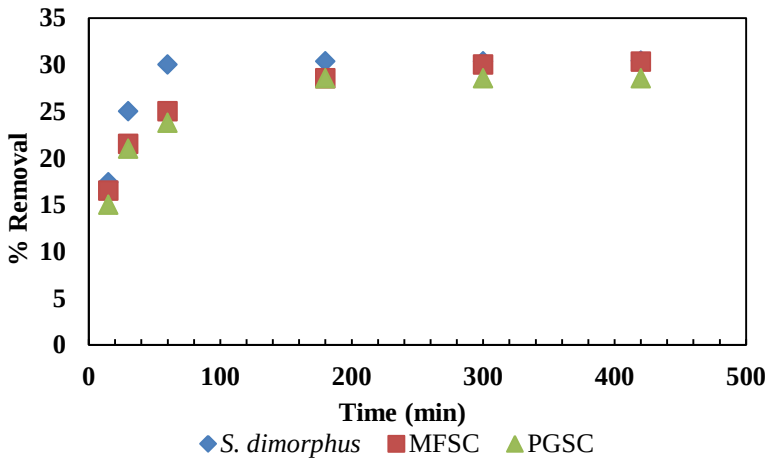

Fig. 4.48: Effect of contact time on removal of Co (II) by using biochars derived from PGSC, MFSC and *S. dimorphus*

Fig. 4.48 showed the effect of contact time by the biochars derived from PGSC, MFSC and *S. dimorphus* within time interval of 15, 30, 60, 90 and 180 min. Rate of sorption of Co by using PGSC and MFSC biochar showed similar trend - it first increased up to 30 min followed by a slight drop at about 60 min and then the two curves attained an equilibrium point at about 90 min. Rate of sorption of Co by *S. dimorphus* biochar was faster in the initial stage and it remains constant after reaching

the equilibrium at 60 min (30% removal within 60 min). These curves indicated that the adsorption sites available on the biochar surface were either saturated beyond the equilibrium point or the remaining vacant binding sites present on the biochar were difficult to occupy due to some repulsive force between the solute molecules of the solid and the bulk phase. The sorption of metal ions on the adsorbent surface depended on the availability of binding sites and electrostatic interaction between them [18]. It can be observed from the Fig. 4.48 that adsorption process in case of *S. dimorphus* biochar was characterized by a strong increase during the first minutes of contact as compared to both MFSC and PGSC derived biochars.

4-3.4. Equilibrium study

Adsorption isotherms are mathematical models that describe the distribution of the adsorbate species among liquid and adsorbent. Isotherms are based on a set of assumptions that are mainly related to the heterogeneity/homogeneity of adsorbents, the type of coverage and possibility of interaction between the adsorbate species. The equilibrium data obtained from the atomic adsorption spectrometer (AAS) were fitted by,twoparameter isotherms, including Freundlich, Langmuir, Harkins-Jura and Dubinin-Radushkevich (D-R) isotherms.

4-3.4.1. Langmuir Adsorption Isotherm

The Langmuir adsorption isotherm model is based on the assumption that there are a finite number of active sites which are homogeneously distributed over the surface of the adsorbent. These active sites have the same affinity for adsorption of a mono molecular layer and there is no interaction between adsorbed molecules [19]. Linear form of Langmuir equation can be written as

$$\frac{1}{q_e} = \frac{1}{q_m} + \frac{1}{q_m K_L C_e}$$

Langmuir adsorption isotherm was obtained by plotting $\frac{1}{q_e}$ vs. $\frac{1}{C_e}$. Values of Langmuir parameters, q_m = maximum monolayer coverage capacity (mg/g) and K_L = Langmuir isotherm constant (L/mg) were determined respectively from the slope and intercept of the plot. The essential features of the Langmuir isotherm might be expressed in terms of equilibrium parameter R_L, which is a dimensionless constant

also referred to as separation factor [5]. The value of R_L indicated the adsorption nature of Co on the PGSC, MFSC and *S. dimorphus* derived biochar surfaces. Adsorption is unfavorable if $R_L > 1$, linear if $R_L = 1$, favorable if $0 < R_L < 1$ and irreversible if $R_L = 0$. Langmuir plot for PGSC, MFSC and *S. dimorphus* are shown in Figs. 4.49 (a), (b) and (c) respectively and corresponding parameters are listed in Table 4.36.

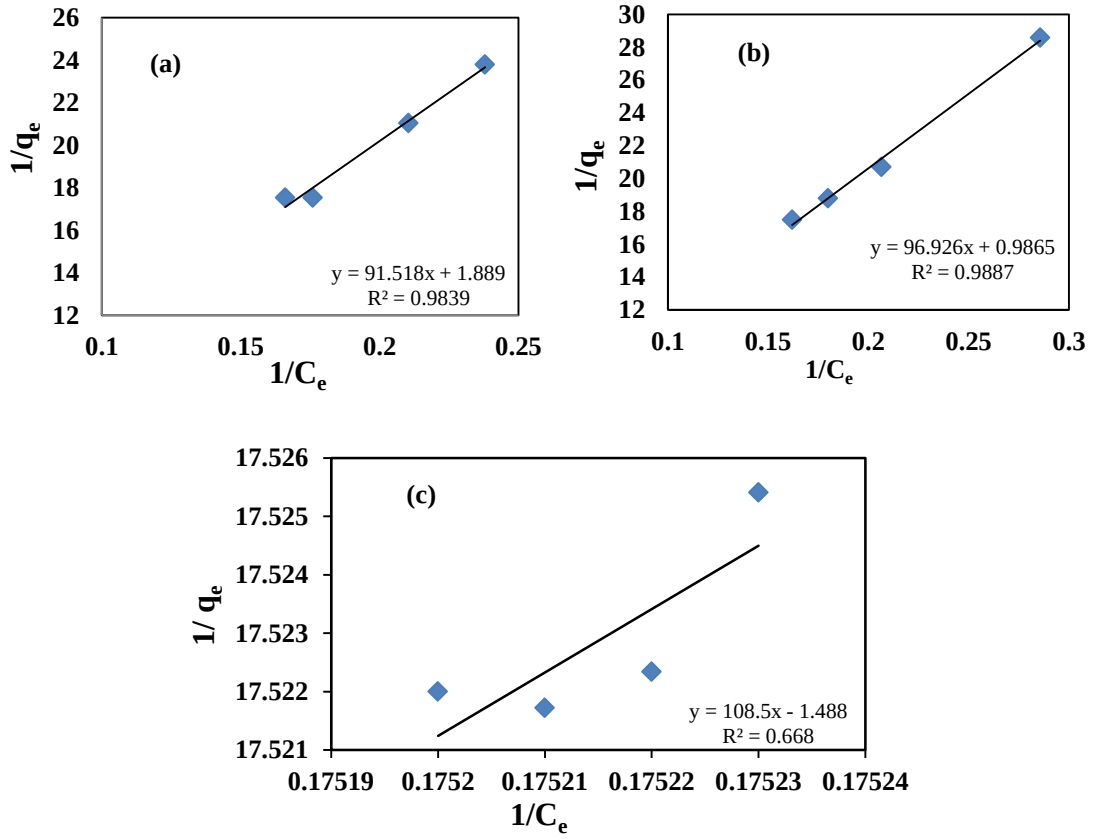

Fig. 4.49: Langmuir adsorption isotherms for (a) PGSC, (b) MFSC and (c) *S. dimorphus*

Table 4.36: Langmuir adsorption isotherm parameters

Isotherms	Plot	Parameters	PGSC	MFSC	*S. dimorphus*
Langmuir	$\frac{1}{q_e}$ vs $\frac{1}{C_e}$	q_m = (intercept)$^{-1}$	0.529 mg g^{-1}	1.01 mg g^{-1}	0.672 mg g^{-1}
		K_L = intercept/slope	0.02 mg^{-1}	0.01 mg^{-1}	0.014 L mg^{-1}
		R_L	0.146	0.256	0.197
		R^2	0.9839	0.9887	0.6680

Table 4.36 showed the Langmuir isotherm constants and correlation coefficients obtained from their corresponding Langmuir plot of PGSC, MFSC and *S. dimorphus* derived biochars. R_L, the separation factor values for PGSC, MFSC and *S. dimorphus* were found to be 0.146, 0.256 and 0.197 respectively. As the R_L values lies between $0 < R_L < 1$, it indicated that the adsorption was favorable for all the biochars. Based on the correlation coefficients, Langmuir model was found to be best-fitted for both PGSC (R^2 = 0.9839) and MFSC (R^2 = 0.9887) biochars. For *S. dimorphus*, significantly lower R^2 value (0.6680) was observed which meant that model was poorly fitted to the Langmuir isotherm model. The maximum monolayer coverage capacity q_m from Langmuir isotherm model was found to be the highest for MFSC biomass (1.01 mg g^{-1}). K_L is the Langmuir isotherm constant and values were found to be 0.02, 0.01 and 0.014 L $mg^{-1}$for biochars from PGSC, MFSC and *S. dimorphus* respectively.

4-3.4.2. Freundlich Adsorption Isotherm

Freundlich adsorption isotherm is commonly used to describe the multilayer adsorption on a heterogeneous surface which assumes that different sites have several adsorption energies [5]. The adsorption isotherm is expressed by the following linear equation

$$log q_e = l_n K_F + \frac{1}{n} \log C_e$$

The Freundlich expression is an exponential equation and is used to estimate the adsorption intensity of the adsorbent towards the adsorbate. The values of K_F and n were calculated from the intercepts and slopes of the Freundlich plots respectively. The affinity of the adsorbent towards the uptake of heavy metal ion is indicated by the value of n [5]. Freundlich adsorption isotherm was plotted between $\log q_e$ vs. $\log C_e$ which allowed for determining the Freundlich constants. The Freundlich parameter $\frac{1}{n}$ was related to the surface heterogeneity. When $0 < \frac{1}{n} < 1$, the adsorption was favorable; $\frac{1}{n} = 1$, the adsorption was homogeneous and there was no interaction among the adsorbed species; $\frac{1}{n} > 1$, the adsorption was unfavorable [18]. When n = 1, partition between the two phases was independent of the concentration [20]. The

results of adsorption isotherm models for PGSC, MFSC and *S. dimorphus* are shown in Figs. 4.50(a), (b) and (c) respectively. The isotherm parameters for adsorption of Co (II) on the three biochar surfaces are given in Table 4.37.

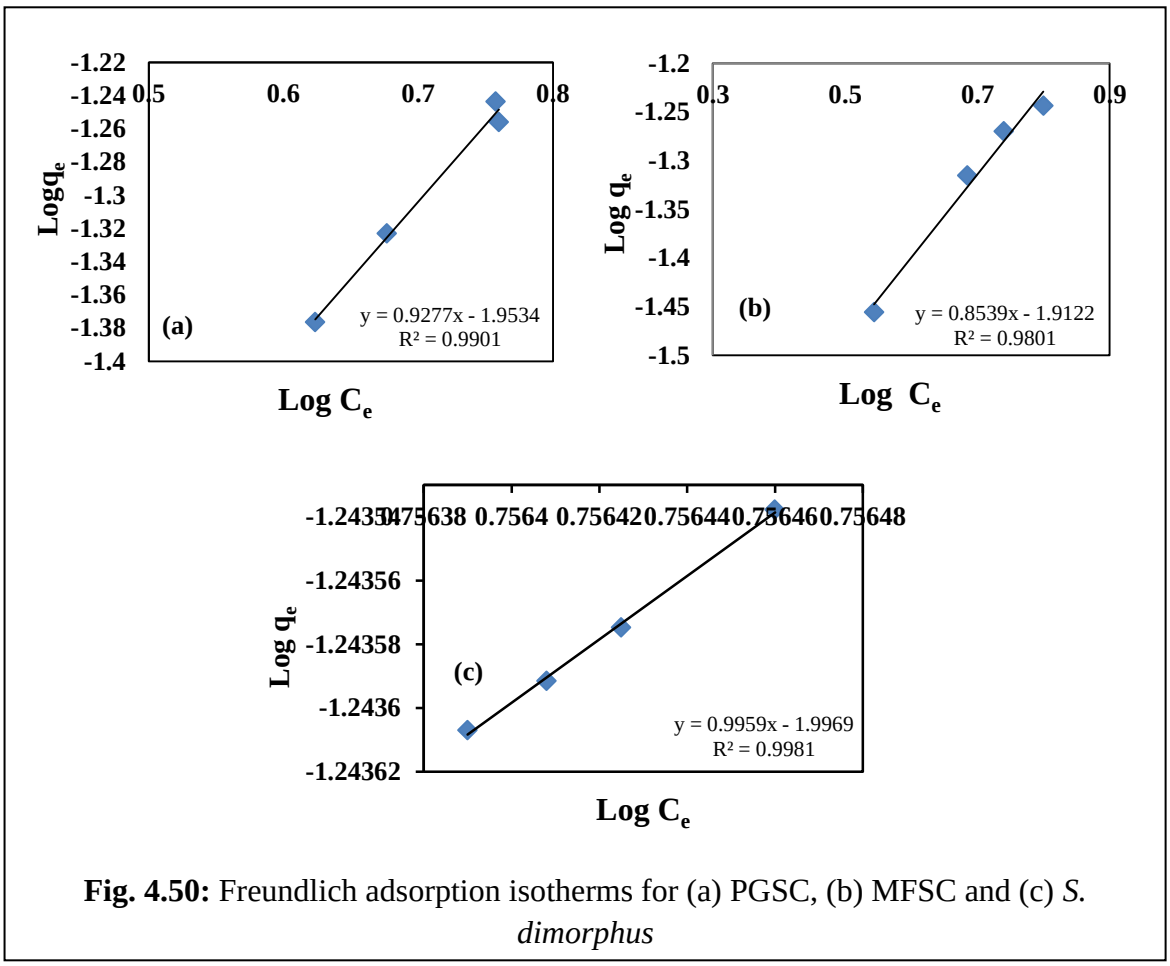

Fig. 4.50: Freundlich adsorption isotherms for (a) PGSC, (b) MFSC and (c) *S. dimorphus*

Table 4.37: Freundlich adsorption isotherm parameters

Isotherm	Plot	Parameters	PGSC	MFSC	*S. dimorphus*
Freundlich	$\log q_e$ vs $\log C_e$	K_F = exp (intercept)	0.141	0.147	0.136
		n = (slope)$^{-1}$	1.077	1.171	1.004
		1/n	0.928	0.854	0.996
		R^2	0.9901	0.9801	0.9981

The magnitude of K_F and n showed the separation and adsorption capacity of heavy metal ion from aqueous solution. The value of n, which was related to the distribution of bonded ions on the adsorbent surface. It was evident from Table 4.37, the value of $\frac{1}{n}$ lied between $0 < \frac{1}{n} < 1$ for biochars derived from PGSC, MFSC and *S. dimorphus* derived biochars, which indicated the favorable multilayer adsorption of

Co (II) on the surface of the biochar. Further, the values of correlation coefficients (0.98–0.99) suggested that Freundlich isotherm model was best fitted for all the biochars. This recommended the heterogeneous nature of biochar surfaces which possibly attributed to the heterogeneous surface of the initial feedstocks. The Freundlich isotherm model assumes that multilayer adsorption occurs on heterogeneous surfaces and that the adsorption amount increases infinitely with increasing concentration [21].

4-3.4.3. Dubinin–Radushkevich adsorption isotherm

Dubinin-Radushkevich (D-R) isotherm is an empirical model generally applied to express the adsorption mechanism onto a heterogeneous surface [5, 22]. The linear form of isotherm is expressed as follows:

$$l_n\, q_e = l_n(q_m) - (B\varepsilon^2)$$

where, $\varepsilon = RT\; l_n\,(1 + \frac{1}{C_e})$

The approach was usually applied to distinguish the physical and chemical adsorption of metal ions with its mean free energy, E per molecule of adsorbate (for removing a molecule from its location in the sorption space to the infinity) could be computed by the relationship [5]

$$E = \frac{1}{\sqrt{2B}}$$

Linear plot of Dubinin-Radushkevich isotherm was obtained by plotting $l_n\, q_e$ vs. ε^2 for PGSC, MFSC and *S. dimorphs* and are shown in Figs. 4.51(a), (b) and (c) respectively. The constants q_m and B were calculated from the intercept and slope of the plots respectively. The D-R isotherm parameters are given in Table 4.38.

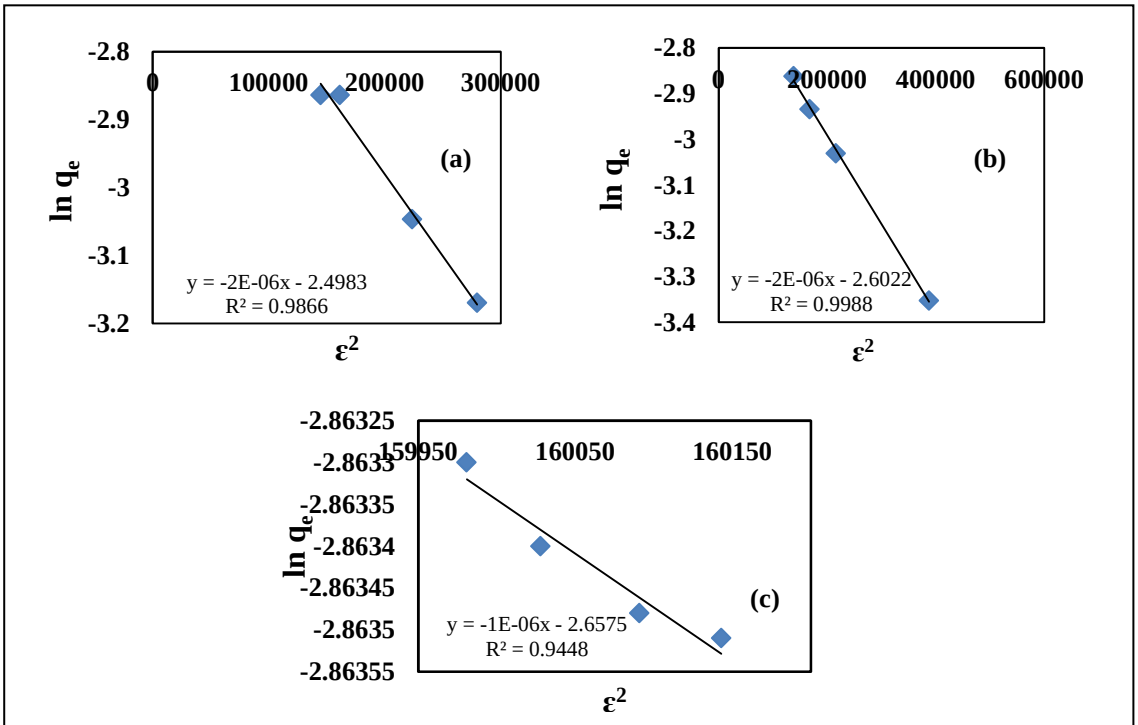

Figs. 4.51: D-R adsorption isotherms for (a) PGSC, (b) MFSC and (c) *S. dimorphus*

Table 4.38: D-R adsorption isotherm parameters

Isotherms	Plot	Parameters	PGSC	MFSC	*S. dimorphus*
Dubinin–Radushkevich	$l_n q_e$ vs ε^2	q_m = exp(intercept)	8.222×10^{-2}	7.411×10^{-2}	7.012×10^{-2}
		B	2×10^{-6}	2×10^{-6}	1×10^{-6}
		E	5.0×10^{-2}	5.0×10^{-2}	7.0×10^{-2}
		R^2	0.9866	0.9988	0.9448

Based on the value of regression parameter as shown in Table 4.38, the adsorption of Co (II) on MFSC biochar (R^2 = 0.9988) and PGSC (R^2 = 0.9866) showed the best fit to the experimental data *S. dimorphus* biochar also showed a good fit to the experimental data with regression parameter R^2 value of 0.9448.

4-3.4.4. Harkins-Jura Isotherm (Hurkins-Jura adsorption isotherm)

The Hurkins-Jura adsorption isotherm can be expressed in linear form as [23]

$$\frac{1}{q_e^2} = \frac{B_H}{A_H} - \frac{1}{A_H} \log C_e$$

where, A_H(mg/g) and B_H are two parameters characterizing the sorption equilibrium.

A plot of $\frac{1}{q_e^2}$ vs. log C_e enabled the determination of model parameters A_H and B_H from the slope and intercept. The isotherm equation accounted for multilayer adsorption. Harkins-Jura plot for adsorption of Co(II) on the biochars surfaces derived from PGSC, MFSC and *S. dimorphus* are shown in Figs. 4.52(a), (b) and (c) and kinetic parameters derived from the corresponding isotherms are listed in Table 4.39.

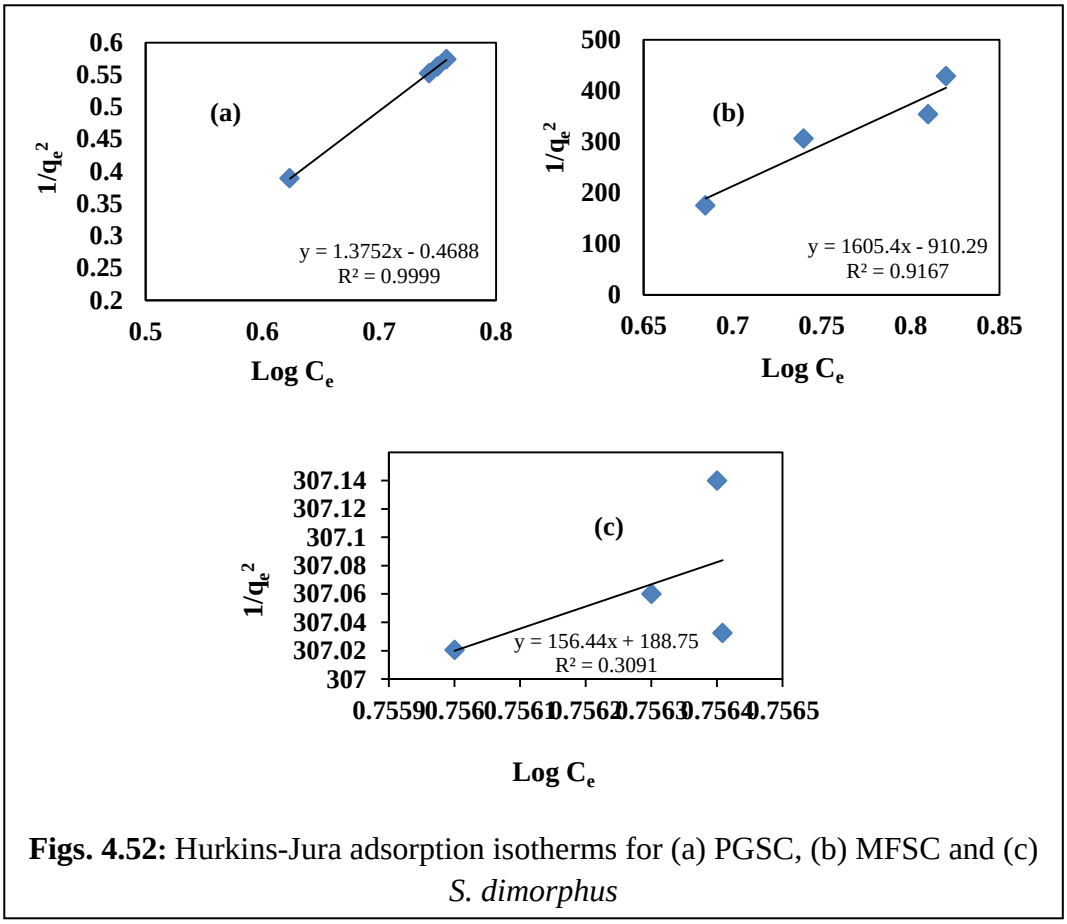

Figs. 4.52: Hurkins-Jura adsorption isotherms for (a) PGSC, (b) MFSC and (c) *S. dimorphus*

Table 4.39: Hurkins-Jura adsorption isotherm parameters

Isotherms	Plot	Parameters	PGSC	MFSC	*S. dimorphus*
Hurkins-Jura	$\frac{1}{q_e^2}$vs.log C_e	A = (slope)$^{-1}$	0.7271	0.0006	0.0064 mg g^{-1}
		B = (intercept/slope)	0.3408	0.5670	1.20
		R^2	0.9999	0.9167	0.3091

It was evident from Table 4.39 that the Harkins-Jura equations seemed to be well fitted for adsorption of Co (II) onto biochars derived from both PGSC and MFSC with higher correlation coefficients. But for *S. dimorphus* biochar, it seemed to be

very poorly fitted to the experimental data with lower value of correlation coefficient R^2= 0.3091.

4-3.5. Kinetic Study

The evaluation of the kinetics parameters is important, since theseparameters can give an insight into the rate and type of adsorption process. In order to investigate the controlling mechanism of adsorption processes, the pseudo-first-order and pseudo-second order equations were applied. Pseudo first-order and pseudo second-order reactionmodels wereused to simulate the adsorption kinetics of Co with respect to the biochars derived from PGSC, MFSC and *S. dimorphus* biomass. The uniformity between experimental data and model predicted values was expressed by correlationcoefficients (R^2 values close or equal to 1).

The kinetic plots between log (q_e-q_t) vs. t and t/q_t vs. t were plotted for pseudo first-order and pseudo second-order reactions respectively. Both the plot gave a set of straight lines for different concentration values and isdepicted in Figs. 4.53, 4.54 and 4.55 correspondingly for biochars derived from PGSC, MFSC and *S. dimorphus*. Slope and intercept values were measured to determine the valueof rate constants (shown in Table 4.40).

Table 4.40: Kinetic parameters derived from both Pseudo first-order and pseudo second-order reactionmodels for adsorption of Co (II) on biochar surfaces

Pseudo-first-order reaction				**Pseudo- second-order reaction**		
Conc. (mM)	K_{ad} **(min^{-1})**	q_e **(mg/g)**	R^2	q_e **(mg/g)**	k**(g mg^{-1} min^{-1})**	R^2
PGSC						
1	0.009	0.230	0.8698	0.585	0.013	0.9931
2	0.010	0.249	0.8576	0.063	1.123	0.9983
3	0.010	0.262	0.8027	0.70	0.857	0.9994
MFSC						
1	0.009	0.218	0.8473	0.057	1.717	0.9962
2	0.008	0.226	0.8101	0.063	1.319	0.9989
3	0.008	0.237	0.9224	0.064	1.350	0.9985
S. dimorphus						
1	0.080	0.882	0.8952	0.072	0.878	0.9991
2	0.081	1.003	0.9203	0.075	0.916	0.9992
3	0.080	1.117	0.8938	0.087	0.618	0.9925

Table 4.40 showed a highly significant regression and the data were well fitted to the pseudo second-order rate equation. The plots of t/qt vs. t give a straight line and isdepicted in Figs. 4.53, 4.54 and 4.55 for PGSC, MFSC and *S. dimorphus* derived biochar. The calculated rate constants and equilibrium concentration are presented in Table 4.40. The higher regression coefficients obtained with the second order kinetics indicates that the goodness of fit is better in the pseudo second-order kinetics model as compared to the pseudo first-order kinetics model for the entire range of kinetics run.

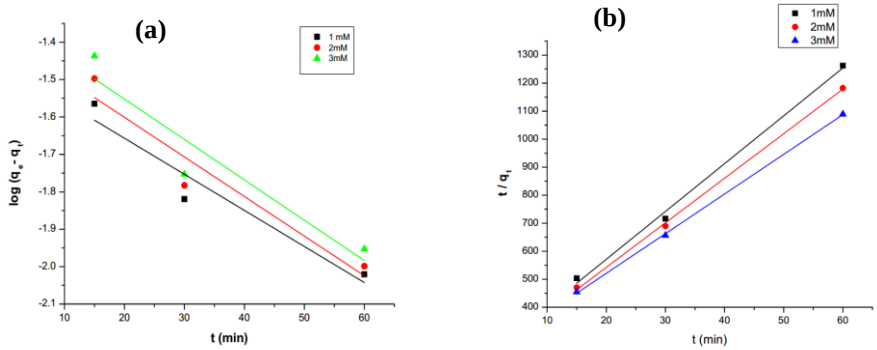

Figs. 4.53: Pseudo first-order (a) and pseudo second-order (b) reaction models for PGSC biochar

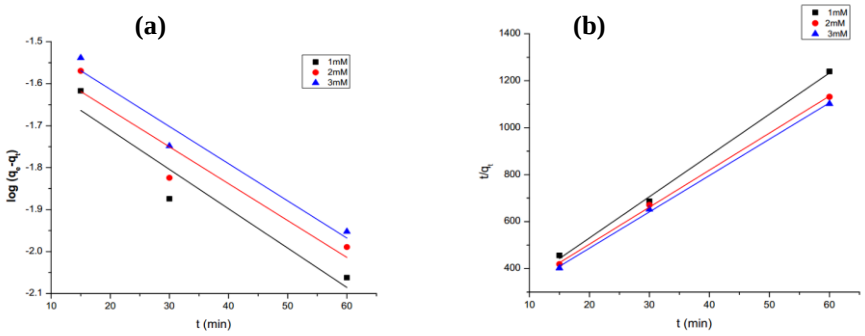

Figs. 4.54: Pseudo first-order (a) and pseudo second-order (b) reaction models for MFSC biochar

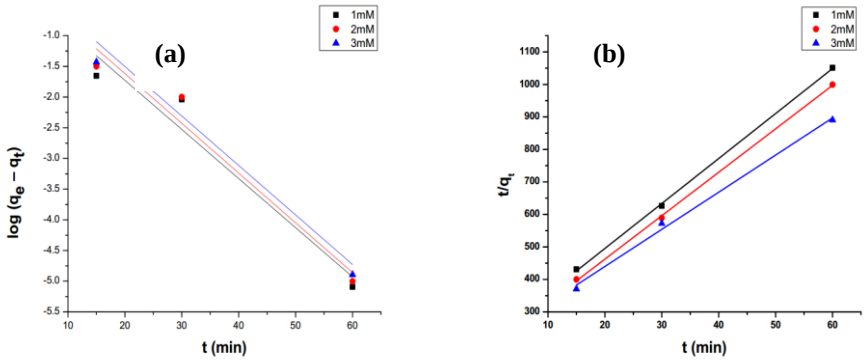

Figs. 4.55: Pseudo first-order (a) and pseudo second-order (b) reaction models for *S. dimorphus* biochar

4-3.6. Post sorption characteristics of biochar

4-3.6.1. SEM analysis

SEM images of the biochars obtained from PGSC, MFSC and *S. dimorphus* after the adsorption of Co (II) metal are shown in Figs. 4.56(a), (b) and (c) respectively. The SEM images of biochars demonstrated the physical changes occurred during adsorption. SEM images of biochars after adsorption showed uneven and rough texture. Some bright spots were also observed on the surface of the biochars covering the caves, pores and surfaces which might be due to the presence of cobalt on surface of the post-sorption biochar.

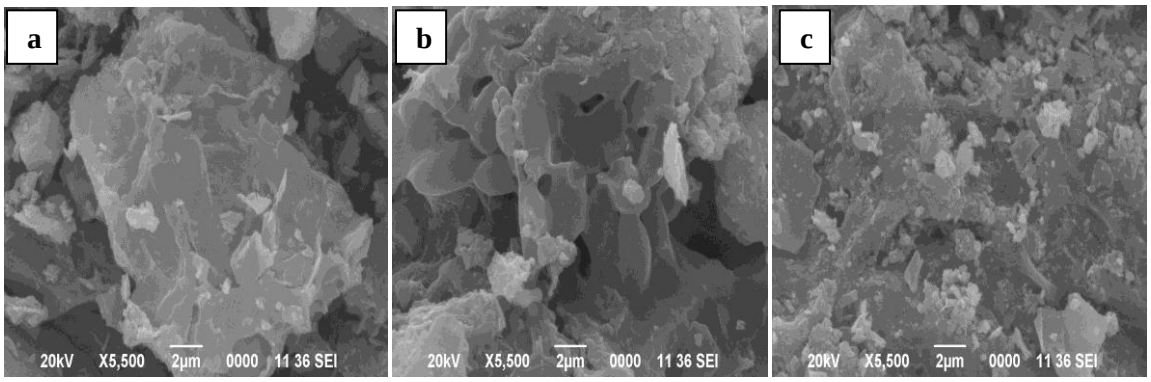

Figs. 4.56: SEM images of biochars derived from (a) PGSC, (b) MFSC and (c) *S. dimorphus* after adsorption Co (II)

4-3.6.2. EDX analysis

The EDX spectrum after adsorption of Co (II) on the biochar surface derived from PGSC, MFSC and *S. Dimorphus* are shown in Figs. 4.57(a), (b) and (c) respectively. The corresponding EDX spectra of the SEM image demonstrated the peaks occurred due to presence of Co on surfaces of the post-sorption biochars. This strongly suggested the precipitation of Co(II) metal from aqueous solution onto the biochar surfaces, because both the elemental analysis and the SEM–EDX analysis of pre-sorption biochars (Chapter 4(a) and 4(b)) showed that no cobalt metal was present on the surface of original biochars.

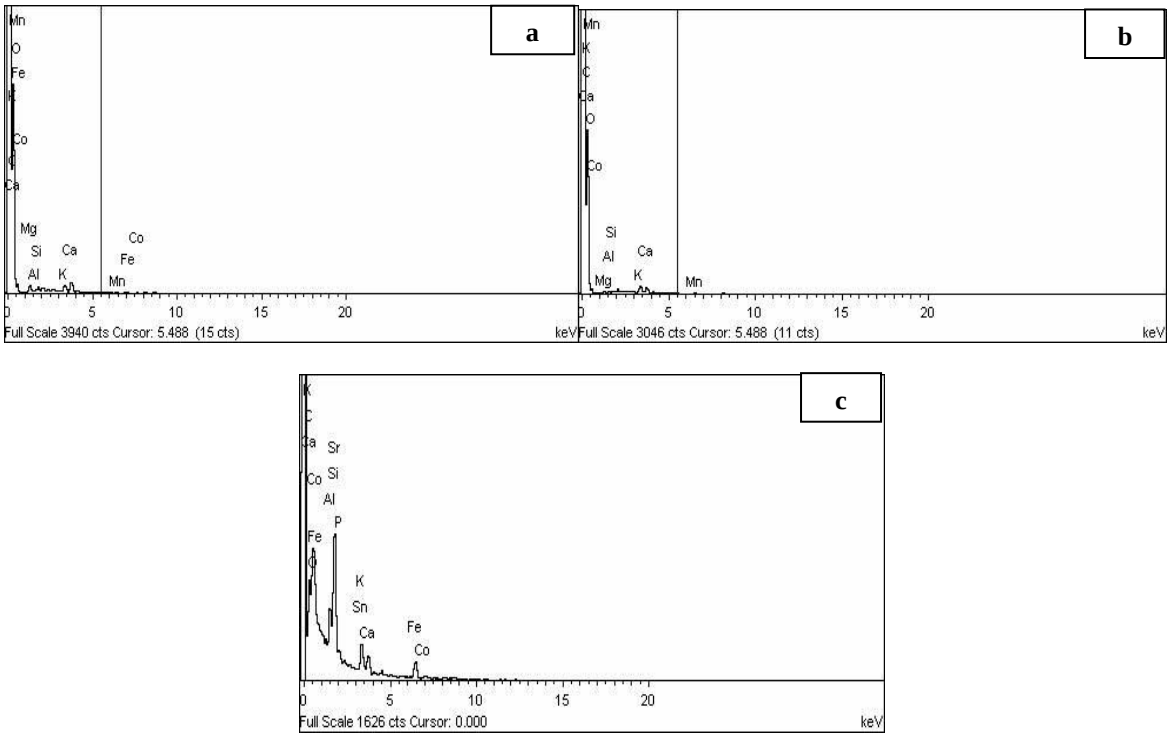

Figs. 4.57: EDX spectrum of biochars after adsorption of Co (II) derived from (a) PGSC (b) MFSC and (c) *S. dimorphus*

4-3.7. Summary

The present investigation showed that biochars derived from PGSC, MFSC and microalgae *S. dimorphus* were found to be a potential sorbent for the removal of Co (II) from aqueous solution. Biochar produced from the pyrolysis of *S. dimorphus* species showed the highest removal efficiency (30% removal efficiency within 60

min) of cobalt as compared to the other two biochars obtained from PGSC and MFSC (25% removal efficiency within 60 min). Experimental data were tested against two parameter isotherms, including Freundlich, Langmuir, Harkins-Jura and Dubinin-Radushkevich (D-R) isotherms. Highest correlation coefficient values (R^2) for Co (II) adsorption were obtained from Hurkins-Jura, Dubinin-Radushkevich (D-R) and Freundlich isotherm model for biochars derived from the PGSC (0.9901), MFSC (0.9988) and *S. dimorphus* (0.9981) respectively. Thus, adsorption on PGSC biochar accounted for multilayer adsorption, adsorption on MFSC biochar accounted on a heterogeneous surface, adsorption on *S. dimorphus* derived biochar showed both heterogeneous and multilayer adsorption phenomenon. Adsorption kinetics was best described by the pseudo-second-order model for all the biochars derived from PGSC, MFSC and *S. dimorphus* biomass as compared to pseudo-first-order kinetic model.

References:

1. Lehmann, J., Gaunt, J., and Rondon, M. Bio-char sequestration in terrestrial ecosystems – a review. *Mitigation and Adaptation Strategies for Global Change*. 11: 403–427, 2006.
2. Laird D.A., Fleming P., Davis D.D., Horton R. Wangn B., and Karlen D.L. Impact of biochar amendments on the quality of a typical Midwestern agricultural soil. *Geoderma*, 158: 443-449, 2010.
3. Mohan, D., Sarswat, A., Ok, Y., and Pittman, C. U. Jr. Organic and inorganic contaminants removal from water with biochar, a renewable, low cost and sustainable adsorbent: A critical review. *Bioresource Technology*, 160: 191–202, 2014.
4. Field, J. L., Keske, C. M. H., Birch, G. L., Defoort, M. W., and Cotrufo, M. F. Distributed biochar and bioenergy coproduction: a regionally specific case study of environmental benefits and economic impacts. *Global Change Biology Bioenergy* 5: 177–191, 2013.
5. Dada, A. O., Olalekan, A. P., Olatunya, A. M., and Dada, O. Langmuir, Freundlich, Temkin and Dubinin–Radushkevich isotherms studies of equilibrium sorption of Zn2+ unto phosphoric acid modified rice husk. *IOSR Journal of Applied Chemistry*, 3(1): 38-45, 2012.
6. Inyang, M. D., Gao, B., Zimmerman, A., Zhou, Y., and Cao, X. Sorption and co-sorption of lead and sulfapyridine on carbon nanotube-modified biochars. *Environmental Science and Pollution Research*, 22: 1868–1876, 2014.
7. Lattao, C., Cao, X., Mao, J., Schmidt-Rohr, K., and Pignatello, J. J. Influence of molecular structure and adsorbent properties on sorption of organic compounds to a temperature series of wood chars. *Environmental Science & Technology*, 48: 4790–4798, 2014.
8. Rajapaksha, A. U., Vithanage, M., Zhang, M., Ahmad, M., Mohan, D., Chang, S. X., and Ok, Y. S. Pyrolysis condition affected sulfamethazine sorption by tea waste biochars. *Bioresource Technology*, 166: 303–308, 2014.
9. Meng, J., Feng, X., Dai, Z., Liu, X., Wu, J., and Xu, J. (2014). Adsorption characteristics of Cu(II) from aqueous solution onto biochar derived from

swine manure. *Environmental Science and Pollution Research,* 21: 7035–7046.

10. Mohan, D., Kumar, H., Sarswat, A., Alexandre-Franco, M., and Pittman, C. U. Jr. Cadmium and lead remediation using magnetic oak wood and oak bark fast pyrolysis bio-chars. *Chemical Engineering Journal,* 236: 513–528, 2014.
11. Yao, Y., Gao, B., Inyang, M., Zimmerman, A. R., Cao, X. D., Pullammanappallil, P., and Yang, L. Y. Removal of phosphate from aqueous solution by biochar derived from anaerobically digested sugar beet tailings. *Journal of Hazardous Materials,* 190: 501–507, 2011.
12. Patra, J. M., Panda, S. S., and Dhal, N. K. Biochar as a low-cost adsorbent for heavy metal removal: A review. *International Journal of Research in BioSciences*, 6: 1-7, 2017.
13. Inyang, M., Gao, B., Yao, Y., Xue, Y., Zimmerman, A. R., Pullammanappallil, P., and Cao, X. Removal of heavy metals from aqueous solution by biochars derived from anaerobically digested biomass. *Bioresource Technology*, 110: 50-56, 2012.
14. Goswami, R., Shim, J., Deka, S., Kumari, D., Kataki, R. and Kumar, M. Characterization of cadmium removal from aqueous solution by biochar produced from Ipomoea fistulosa at different pyrolytic temperatures. *Ecological Engineering*, 97: 444-451, 2016.
15. Parab, H., Joshi, S., Sudersanan, M., Shenoy, N., Lali, A., and Sarma, U. Removal and recovery of cobalt from aqueous solutions by adsorption using low cost lignocellulosic biomass—coir pith. *Journal of Environmental Science and Health Part A*, 45(5): 603-611, 2010.
16. World Health Organization. The world health report 2007: a safer future: global public health security in the 21st century.
17. Pan, X., Wang, J., and Zhang, D. Sorption of cobalt to bone char: kinetics, competitive sorption and mechanism. *Desalination*, 249(2): 609-614, 2009.
18. Pellera, F., Giannis, A., Anastasiadou, K., Kalderis, D., Pentari, D., and Gidarakos, E. Adsorption of Cu (II) ions from aqueous solutions using biocharprepared from agricultural by-products. In 2nd International Conference on Hazardous and Industrial Waste Management–CRETE, 2010.

19. Vijayakumar, G., Senthilnathan, P., Pandurangan, K., and Ramakrishna, G. Impact and energy absorption characteristics of lathe scrap reinforced concrete. *International Journal of Structural and Civil Engineering Research*, 1(1): 1-6, 2012.
20. Komkiene, J., and Baltrenaite, E. Biochar as adsorbent for removal of heavy metal ions [Cadmium (II), Copper (II), Lead (II), Zinc (II)] from aqueous phase. *International Journal of Environmental Science and Technology*, 13(2): 471-482, 2016.
21. Agrafioti, E., Kalderis, D., and Diamadopoulos, E. Arsenic and chromium removal from water using biochars derived from rice husk, organic solid wastes and sewage sludge. *Journal of environmental management*, 133: 309-314, 2014.
22. Sampranpiboon, P., Charnkeitkong, P., and Feng, X. S. Determination of Thermodynamic Parameters of Zinc (II) Adsorpton on Pulp Waste as Biosorbent. In Advanced Materials Research, Vol. 931, pages 215-219, Trans Tech Publications, 2014.
23. Jusoh, A., Hartini, W. J. H., and Endut, A. Study on the removal of pesticide in agricultural run off by granular activated carbon. *Bioresource Technology*, 102(9): 5312-5318, 2011.

4-4.1. Introduction

Among the various organic pollutants, large amounts of dye effluents are annually discharged by textile, cosmetics, paper, leather, pharmaceutical, food and other industries [1]. Dumping of dye containing effluents into water pools and surrounding industrial areas adversely affects surface water [2], ground water [3] and even soils through irrigation [4-5]. Presence of low concentration (>1ppm) of dyes is highly visible and can adversely affect the aquatic environment by preventing light penetration. Some dyes and their degradation products are found to be toxic, mutagenic and carcinogenic in nature [6] because of presence of carcinogens, such as benzidine, naphthalene and other aromatic compounds in some dyes [7]. Thus, the removal of dyes from effluents has been given utmost importance.

In the present study, biochar produced from the *Pongamia glabra* seed cover (PGSC) was used as an adsorbent for removal of dye effluents and investigate the adsorption efficacy of the biochar for the removal of synthetic dyes from aqueous solution.

4-4.2. Selection of dyes

Dyes are colorful organic compounds. The complex aromatic structures of dyes make them more stable and difficult to remove from the effluents discharged into water bodies [8]. Untreated releases of effluents into the environment are found to be toxic, mutagenic and carcinogenic in nature [9]. Synthetic dyes are resistant to natural degradation and pose numerous environmentally-oriented drawbacks when released into natural water bodies. Methylene blue (MB) and Rhodamine B (RB) are two synthetic basic dyes used extensively in dyeing of various products including cotton, silk, paper, bamboo, weed, straw and leather [10]. Being cationic in nature basic dyes are considered as more toxic than the anionic dyes, since they can easily interact with the negatively charged surface of cell membranes, and can enter into the cells [11]. MB can cause eye burns in humans and animals, methemoglobinemia, cyanosis, convulsions, tachycardia, dyspnea, irritation to the skin, and if ingested, irritation to the gastrointestinal tract, nausea, vomiting, and diarrhea [12]. Similarly, RB can cause skin and eye irritation with redness and pain, irritation to the respiratory

tract and gastro-intestinal tract [10]. Among a number of different techniques of dye removal from the aqueous medium, adsorption is one of the most efficient and attractive methods for removing pollutants from wastewater because of its easy process control, low cost and minimal energy requirements [13]. Nowadays, biochar, a byproduct of pyrolysis process has received increased attention as adsorbent, since the production of biochar is considered as cheaper method with lower energy requirements as compared to traditional activated carbon [14]. Till now, a few studies have been reported on removal of dyes on using biochar as adsorbent. Therefore, this chapter makes an attempt to discuss the removal of two important and abundantly used dyes by using biochar derived from PGSC biomass.

4-4.3. Optimization of adsorption parameters

Optimization of biomass, pH and temperature for the efficient uptake of MB and RB by the biochar are shown in Figs. 4.58 (a), (b) and (c). It was evident that adsorption of MB was superior to RB by the PGSC biochar. It was observed from the Fig. 4.58 (a) that for adsorption of MB and RB at a concentration of 50 ppm, the optimum biochar requirement was 30g/L (90% of dye adsorption) and 50g/L (60% of dye adsorption) respectively. Increasing biomass beyond optimum amounts did not alter the adsorption of the dyes. Effect of pH on adsorption of MB by biochar was found to be minimal at a wide range of pH from 3.0 to 10.0. However, a sharp decline in adsorption was found when pH was raised to 11.0 (Fig. 4.58 (b)). In contrast, adsorption of RB was fairly uniform in the range of 3.0 to 11.0 with a minor drop in adsorption percentage at pH 8.0. In general, with decrease in pH of the system, the number of negatively charged adsorbent sites decreased and positively charged surface sites increased, which might not favor the adsorption of positively charged dye cations. Since, the adsorption percentage of the dyes by biochar remained almost constant in a wide range of pH, there might exist another mode of adsorption, i.e., ion exchange [15]. Adsorption of dyes in a wide range of pH by PGSC biochar is advantageous for its potential use in management of diverse industrial effluents released at varying pH. The optimum temperature for both MB and RB adsorption was found to be 28 ºC (Fig. 4.58(c)). The dependence on temperature was minimal for

adsorption of RB, while adsorption percentage varied significantly with temperature in case of MB.

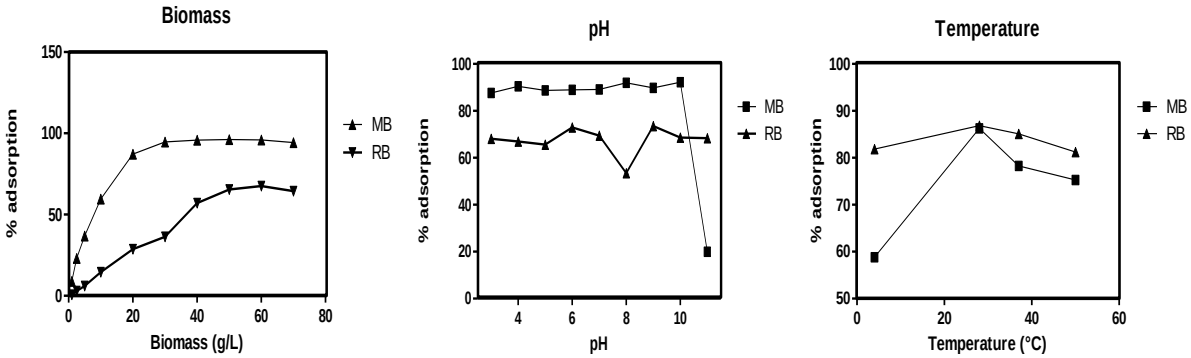

(a) (b) (c)

Figs. 4.58: Plots showing optimization of (a) biomass, (b) pH and (c) temperature for the adsorption of Methylene blue (MB) and Rhodamine B (RB) by PGSC biochar

4-4.4. Effect of initial concentration

To achieve efficient adsorption of synthetic dyes by various adsorbents, the initial concentration of the dyes is one of the major parameter of consideration. In order to study the effect of the initial concentrations of MB and RB on the rate of dye adsorption onto PGSC biochar, experiments were carried out at different initial dye concentrations of MB and RB (10, 20, 30, 40 and 50 mg/L) for different time intervals (10–480 min) at 28 ºC as shown in Figs. 4.59 (a) and (b) respectively. The initial concentration of the dye was varied keeping the amount of biosorbent constant. It was observed that the initial adsorption of dye increased with rise in concentration of synthetic dyes initially and reached a point of equilibrium, beyond which there was no further increase in the adsorption. It was also noted that adsorption of lower concentration of dyes reached equilibrium earlier than those with higher concentration.

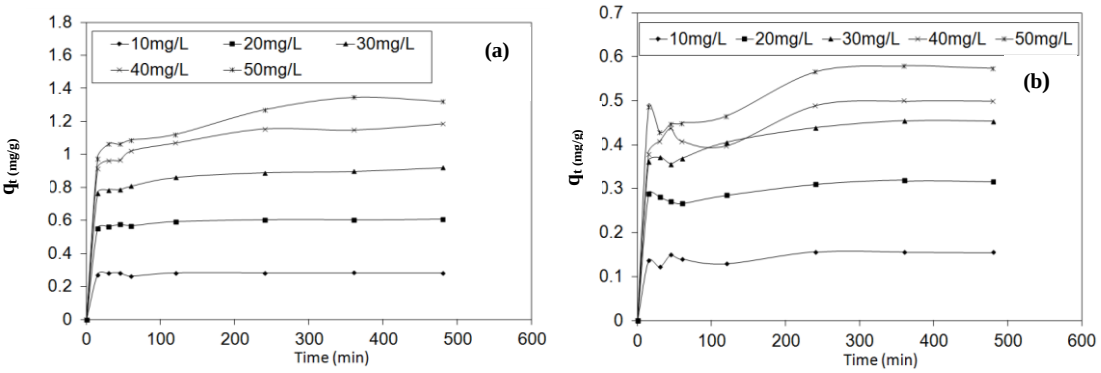

Fig. 4.59: Effect of initial concentration on uptake of (a) Methylene blue (MB) and (b) Rhodamine B (RB) by PGSC biochar

4-4.5. Adsorption isotherm

In order to establish a relation between adsorbate concentration in the solution and the amount adsorbed at the adsorbent interface, adsorption isotherm studies were carried out. The results were analyzed by using four different isotherms, namely, Langmuir, Freundlich, Temkin and Dubinin-Radushkevich isotherms, which are shown below in Fig. 4.60. The isotherm constants are given in Table 4.41.

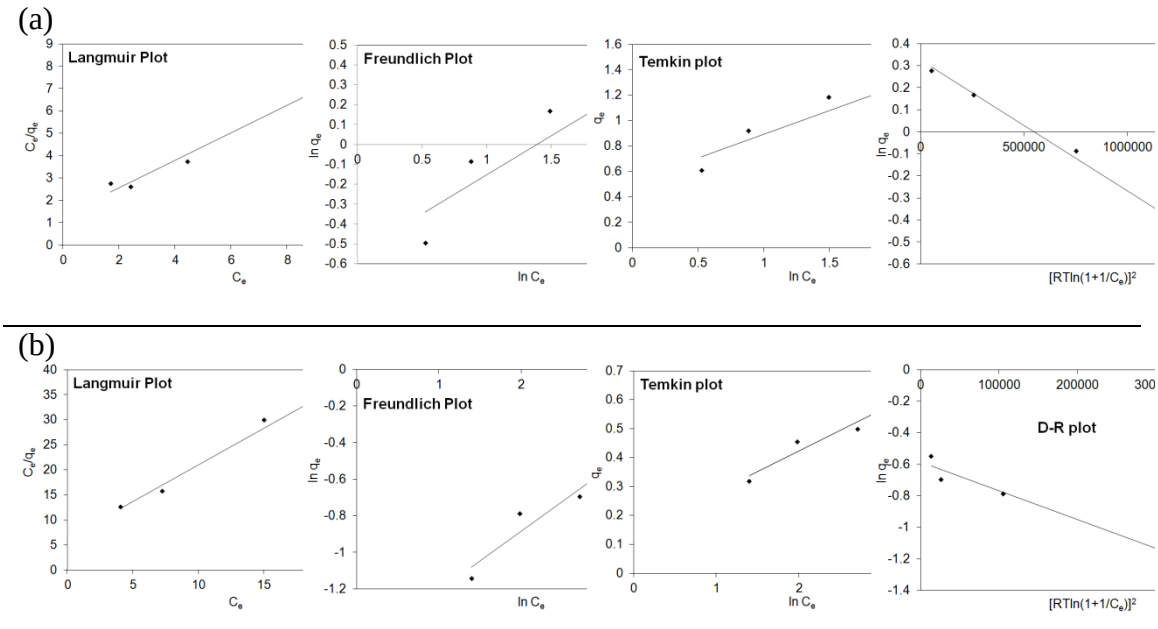

Figs. 4.60: Isotherm plots for adsorption of (a) Methylene blue (MB) and (b) Rhodamine B (RB) by PGSC biochar

Table 4.41: Isotherm constants for the adsorption of MB and RB with PGSC biochar

Isotherm Parameters	Methylene blue	Rhodamine B
Langmuir		
Qo (mg/g)	1.623	0.683
b (L/mg)	0.462	0.952
R^2	0.98	0.98
Freundlich		
K_F	1.727	4.653
n	2.545	3.059
R^2	0.82	0.91
Temkin		
A	4.018	2.661
B	0.374	0.142
R^2	0.88	0.93
Dubinin-Radushkevich		
q_D	1.385	1.795
B_D	6×10^{-7}	2×10^{-6}
R^2	0.99	0.95

It could be observed from the Table 4.41 that, in case of Langmuir adsorption isotherm, both dyes with PGSC biochar showed high regression coefficient (R^2) value of 0.98. The R_L value for MB was of 0.04 while the value for RB adsorption was 0.02 which suggested that both the adsorption could follow Langmuir adsorption. For Frendlich adsorption isotherm, parameters suggested relatively low regression coefficient (R^2) values of 0.82 and 0.91 for adsorption of the MB and RB, respectively. Similarly, the regression coefficient (R^2) values for Temkin isotherm model were lower than that of Langmuir isotherm model. Study of D-R isotherm model for the adsorption of MB by PGSC biochar revealed a very high regression coefficient (R^2) value of 0.99 suggesting that the D-R adsorption isotherm model is the best fit for this adsorption. D-R isotherm model implies a physical mode of adsorption characterized by porous adsorbent biomass. Using the same model, the adsorption of RB by PGSC, however, showed a lower R^2 value of 0.95. The value was lesser than that of Langmuir isotherm model. From four isotherm analyses, it may be concluded that adsorption of MB and RB with PGSC biochar could be best explained by D-R and Langmuir isotherm models, respectively.

4-4.6. Adsorption kinetics

Adsorptions of dyes are known to follow a pseudo-second-order kinetics which can be expressed in linear form as:

$$\frac{t}{q_t} = \frac{1}{k_2 q_e^2} + \frac{t}{q_e}$$

where, the dye adsorbed at equilibrium (q_e) and the second order constants k_2 (g/mg h) could be determined from the slope and intercept of plot t/q_t vs t. Figs. 4.61 (a) and (b) represented the pseudo-second-order sorption kinetics of MB and RB on biochar. The values for k_2 and q_e (both experimental and calculated) were represented in Table 4.42. The data analysis suggested that the correlation coefficients (R^2) for fitting the data to the pseudo-second-order kinetic model were close to unity. Values of q_e calculated using pseudo-second-order kinetic model were in agreement with the experimentally determined values of q_e. Thus, the pseudo-second-order model described the mechanism of the MB and RB adsorption by the biochars satisfactorily. This observation suggested that the adsorption could predominantly be due to chemisorptions which were described in cases of adsorptions that follow pseudo-second-order kinetics [16].

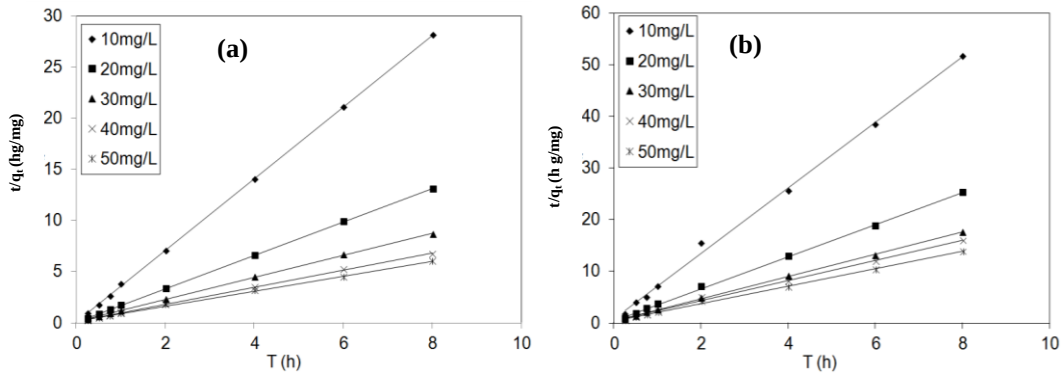

Figs. 4.61: Pseudo-second-order sorption plots for adsorption of (a) Methylene blue (MB) and (b) Rhodamine B (RB) on PGSC biochar.

Table 4.42: Pseudo-second-order kinetics parameters for adsorption of MB and RB on PGSC biochar

Dye	Initial concentration (ppm)	q_e experimental (mg/g)	Parameters for pseudo second order kinetics		
			K_2 (g/mg h)	q_e calculated (mg/g)	R^2
Methylene blue (MB)	10	0.28	165.99	0.28	0.99
	20	0.61	31.15	0.61	0.99
	30	0.91	9.07	0.92	0.99
	40	1.18	5.32	1.19	0.99
	50	1.32	3.36	1.36	0.99
Rhodamine B (RB)	10	0.15	46.54	0.15	0.99
	20	0.31	22.82	0.32	0.99
	30	0.45	11.35	0.46	0.99
	40	0.49	9.21	0.51	0.99
	50	0.57	6.75	0.59	0.99

4-4.7. Post sorption characteristics of biochar

SEM analysis

Images from scanning electron microscopy (SEM) studies showing the surface topologies of the biochars before and after the adsorption of MB and RB dyes are shown in Fig. 4.62. The SEM images of biochars demonstrated physical changes in surface structures during adsorption. The image of biochar showed a smooth surface with distinct pores before adsorption, while biochars after adsorption showed rough texture. After adsorption of MB dyes, the pores on the biochar surface were occupied by the dye molecules which may have caused the surface to be uneven. After adsorption of RB dyes, some bright spots were observed on the surface of biochar covering the pores. Rough surface was observed for the adsorption of RB dyes as compared with adsorption of MB dyes on biochar. The heterogeneous compactness of biomass surfaces indicates a non-uniform adsorption process.

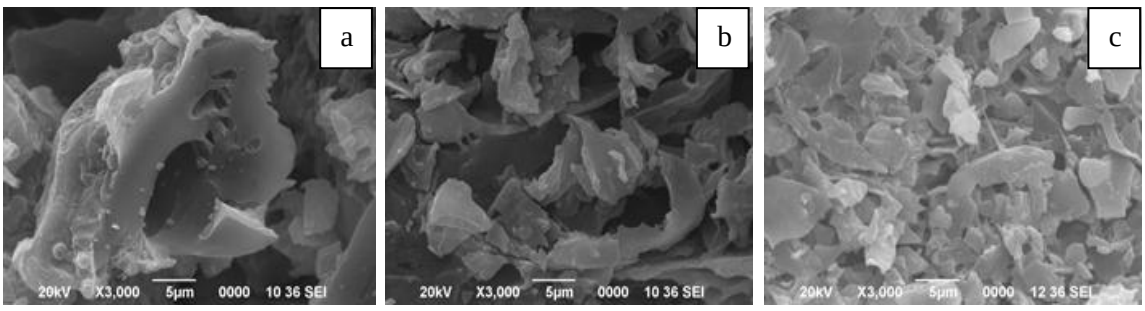

Fig. 4.62: SEM image of PGSC biochar (a) before dye adsorption (b) after adsorption of Methylene blue (MB) and (c) after adsorption of Rhodamine B (RB)

FTIR analysis

The FTIR spectra of biochar before and after adsorption of MB and RB dyes are shown in Fig. 4.63. The absorption peak at 3200–3550 cm^{-1} indicates the presence of O–H group (or N–H) along with moisture [17]. The C–H stretching vibrations between 2830 and 2928 cm^{-1} and C–H deformation vibrations between 1410 and 1515 cm^{-1} indicated the presence of alkanes. Moreover, the location of bending vibration of C–H groups at 1378 cm^{-1} provides another evidence of the fact that this band is very important for the detection of methyl groups in a given compound [18]. The region between 700 and 900 cm^{-1} contains various bands related to the aromatic, out of plane C–H bending. The high intensity of the above mentioned bands indicated that the aromatic hydrogen was located in aromatic rings with high degree of substitution after adsorption of MB and RB dyes [19].

After adsorption of MB on the biochar surface, N–H bending vibration was observed from 1650–1590 cm^{-1}, and C–N stretching was observed from 1090–1020 cm^{-1} for primary amine. Intensity of the peak at 3433 cm^{-1} increased after adsorption of MB, indicated the presence of O–H and N–H groups of amine. After adsorption of RB on the biochar surface, the stretching frequency appearing at 3441 cm^{-1} was attributed to the presence of O–H group. This O–H stretching might be occurred from carboxylic group (–COOH) present in RB. The weak band at 1629 cm^{-1} can be related to stretch from carboxylic group and peaks at 1403 cm^{-1} and 1049 cm^{-1} might be due to O–H bending vibration of carboxylic acid. N–H bend was observed at 1650–1550 cm^{-1} and C–N stretch was observed at 1123 cm^{-1} for secondary amine [20]. All these changes in functional groups of the PGSC biochar post dye adsorption suggested the ole of these groups in adsorption of the dyes.

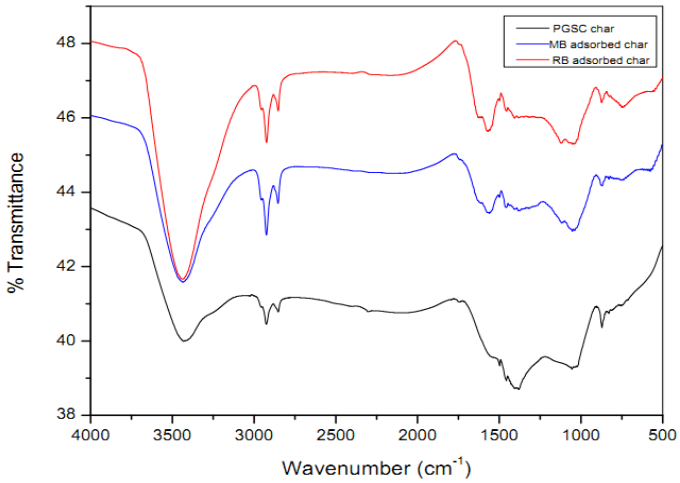

Fig. 4.63: FTIR spectrum of PGSC biochar before (black) and after adsorption with MB (blue) and RB (red).

4-4.8. Summary

The present study investigated the efficacy of biochar derived from PGSC produced at 550 ºC as an adsorbent for the removal of cationic dyes, MB and RB from aqueous solutions. It was observed that, at 50 ppm concentration, for adsorption of both MB and RB the optimum biochar requirement was 30g/L (90% of dye adsorption) and 50g/L (60% of dye adsorption) respectively. Adsorption was found to be independent of solution pH and optimum temperature for both MB and RB adsorption was found to be 28 ºC. The adsorption of MB by PGSC biochar followed D-R adsorption isotherm model with a regression coefficient (R^2) of 0.99. Adsorption of RB by biochar however, followed Langmuir adsorption isotherm model with a regression coefficient (R^2) of 0.98 and an R_L value of 0.02. This observation suggested that the adsorption of MB by biochar is a heterogeneous kind of adsorption occurs at multilayer surface of the adsorbent whereas the adsorption of RB is homogenous kind of adsorption and occurs in a monolayer fashion. Study showed that PGSC biochar had high removal efficiency for MB and also an effective adsorbent for removal of RB from wastewater. Thus, the PGSC biochar can be considered as an effective adsorbent for removal of the dye from waters without any pre-treatment.

References:

1. Safarikova, M., Ptackova, L., Kibrikova, I., and Safarik, I. Biosorption of water-soluble dyes on magnetically modified Saccharomyces cerevisiae subsp uvarum cells. *Chemosphere*, 59 (6): 831–835, 2005.
2. Carneiro, P.A., Umbuzeiro, G.A., Oliveira, D.P., and Zanoni, M.V.B. Assessment of water contamination caused by a mutagenic textile effluent/dye house effluent bearing disperse dyes. *Journal of Hazardous Materials*, 174 (1-3): 694–699, 2010.
3. Dubey, S.K., Yadav, R., Chaturedi, R.K., Yadav, R.K., Sharma, V.K., and Minhas, P.S. Contamination of ground water as a consequence of land disposal of dye waste mixed sewage effluents: a case study of Panipat District of Haryana. India. *Bulletin of Environmental Contamination and Toxicology*, 85 (3): 295–300, 2010.
4. Topaç, F.O., Dindar, E., Uçaroglu, S., and Baskaya, H.S. Effect of a sulfonated azo dye and sulfanilic acid on nitrogen transformation processes in soil. *Journal of Hazardous Materials*, 170 (2-3): 1006–1013, 2009.
5. Zhou, Q.X., and Wang, M.E. Adsorption-desorption characteristics and pollution behavior of reactive X-3B red dye in four Chinese typical soils. *Journal of Soils and Sediments*, 10 (7): 1324–1334, 2010.
6. Keharia, H., and Datta, M. Bioremediation concepts for treatment of dye containing wastewater: A review. *Indian Journal of Experimental Biology*, 41 (9): 1068-1075, 2003.
7. Carmen, Z., and Daniela, S. Textile organic dyes–characteristics, polluting effects and separation/elimination procedures from industrial effluents–a critical overview. In Organic Pollutants Ten Years after the Stockholm Convention-Environmental and Analytical Update. InTech, 2012.
8. Crini, G. Non-conventional low-cost adsorbents for dye removal: a review. *Bioresource Technology*, 97(9): 1061-1085, 2006.
9. Keharia, H. and Datta, M. Bioremediation concepts for treatment of dye containing wastewater: a review. *Indian Journal of Experimental Biology*, 41 (9): 1068–1075, 2003.

10. Shakir, K., Elkafrawy, A.F., Ghoneimy, H.F., Beheir, S.G.E. and Refaat, M. Removal of rhodamine B (a basic dye) and thoron (an acidic dye) from dilute aqueous solutions and wastewater simulants by ion flotation. *Water Research*, 44 (5): 1449-1461, 2010.
11. Orfanos A., Manariotis I.O. and Karapanagioti H.K. 2016 Sorption of Methylene Blue onto Food Industry Byproducts. http://www.biochar-international.org/node/7046/accessed 22/05/2017.
12. Senthilkumaar, S., Varadarajan, P.R., Porkodi, K, and Subbhuraam, C.V. Adsorption of methylene blue onto jute fiber carbon: kinetics and equilibrium studies. *Journal of Colloid and Interface Science*, 284 (1): 78-82, 2005.
13. Yang, Y., Lin, X., Wei, B., Zhao, Y. & Wang, J. Evaluation of adsorption potential of bamboo biochar for metal-complex dye: equilibrium, kinetics and artificial neural network modeling. *International Journal of Environmental Science and Technology*, 11 (4): 1093–1100, 2014.
14. Tan, X., Liu, Y., Zeng, G., Wang, X., Hu, X., Gu, Y. & Yang, Z. Application of biochar for the removal of pollutants from aqueous solutions. *Chemosphere*, 125: 70–85, 2015.
15. Garg, V.K., Gupta, R., Yadav, A.B., and Kumar, R. Dye removal from aqueous solution by adsorption on treated sawdust. *Bioresource Technology*, 89 (2): 121–124, 2003.
16. Malash, G.F., and Mi, E.K. Methylene blue adsorption by the waste of Abu-Tartour phosphate rock. *Journal of Colloid and Interface Science*, 348 (2): 537–545, 2010.
17. Pütün, A.E., Özcan A., and Pütün, E. Pyrolysis of hazelnut shells in a fixed-bed tubular reactor: yields and structural analysis of bio-oil. *Journal of Analytical and Applied Pyrolysis*, 52 (1): 33–49, 1999.
18. Apaydin-Varol, E., Uzun, B.B., Önal, E., and Pütün, A.E. Synthetic fuel production from cottonseed: fast pyrolysis and a TGA/FT-IR/MS study. *Journal of Analytical and Applied Pyrolysis*, 105, 83–90: 2014.
19. Ozbay, N., Pütün, A.E., and Pütün, E. Bio-oil production from rapid pyrolysis of cottonseed cake: product yields and compositions. *International Journal of Energy Research*, 30 (7): 501–510, 2006.

20. Rani, M.J., Murugan, M., Subramaniam, P. and Subramaniam, E. Study of water soluble dyes adorption from aqueous solution by Prosopis spicigera L. wood (PSLW) carbon. *Indian Journal of Chemical Technology*, 23 (1): 22-30, 2016.